Physical modeling of cavitation using an enthalpy based model

Gert-Jan Meijn

Master of Science Thesis

TU Delft Delft University of Technology

Process and Energy

Physical modeling of cavitation using an enthalpy based model

Master of Science Thesis

For the degree of Master of Science in Mechanical Engineering at Delft University of Technology

Gert-Jan Meijn

September 22, 2015

Faculty of Mechanical, Maritime and Materials Engineering (3mE) · Delft University of Technology

Flowserve Etten-Leur - 2015

Delft University of Technology
Department of
Process and Energy (p&E)

The undersigned hereby certify that they have read and recommend to the Faculty of Mechanical, Maritime and Materials Engineering (3mE) for acceptance a thesis entitled

Physical modeling of cavitation using an enthalpy based model

by

Gert-Jan Meijn

in partial fulfillment of the requirements for the degree of

Master of Science Mechanical Engineering

Dated: September 22, 2015

Supervisor(s):

dr.ir. R. Pecnik

dr.ir. F.C. Visser

Reader(s):

prof.dr.ir. B.J. Boersma

dr.ir. M. Pourquie

Abstract

The International Energy Agency (IEA) reported that 10% of the world energy consumption is due to pumps and pump related equipment.[1] From this it is gathered that, by improving the efficiency of pumps and lowering their energy consumption in general, a real difference can be made in the global energy consumption. But on the other side of the coin, there are practical limitations that are imposed on the pump design by the process conditions or the surroundings in which the pump most operate. Real-life situations may require a pump to operate far from its Best Efficiency Point (BEP), which in most cases will lead to the development of cavitation.

Cavitation is defined as the process of formation and disappearance of a vapor phase in a liquid when this liquid is subjected to reduced pressures, followed by an increase of pressure. One of the main challenges in the design and application of centrifugal pumps is the ability to control and limit the development of cavitation. It is generally unlikely that a pump will operate across its entire operating range without any cavitation. But a distinction must be made between the general presence of cavitation and the point at which the levels of cavitation become too high and will start to influence the peformance of the pump and damage the pump.

Computational Fluid Dynamics (CFD) is used extensively to model cavitation in pump impellers. These models are almost always governed by empirical relations, which is no problem for cold water that has ample test data to be validated with, but makes the prediction of cavitation for hydrocarbons or amine solutions impossible. In the present work the cavitation development of water, butane and propane is described using a barotropic model assuming an isenthalpic expansion in the two-phase region. This barotropic relation should only be governed by the fluid properties, no empiricism should be involved.

First a literature study is performed to gain insight into the mechanics and thermodynamics of cavitation. The inception, growth and collapse phases of cavitation are individually discussed and the related physics are analyzed. This is followed by a discussion of the different possibilities to model cavitation in a CFD environment, explaining the pros and cons of incompressible versus compressible modeling.

[1] IEA Report 2009, IEA Statistics, CO2 Emissions from fuel combustion

The development of the model is divided in a physical section and a numerical section. The physical section shows the development and validation of the barotropic model. Starting with the mixed isentropic-isenthalpic model from Brennen, it is reduced to an barotropic isenthalpic model assuming full thermal contact and the evaluation of fluid properties at free stream temperature. Validating the model with data from a thermodynamic library, to confirm isenthalpic expansion behavior, closes the section. Although butane and propane are considered much more sensitive to the local thermal effects of cavitation than water, the validation of the barotropic model showed satisfactory results for every fluid used in this work. In the numerical section the finite volume method (FVM) is presented including the MUSCL face extrapolation method to estimate quantities at the cell faces based on cell centered values. The AUSM-HLLC hybrid scheme is reviewed, that will calculate the flux of the quantities through each of the cell interfaces. The numerical section is closed by a full overview of the model, showing the final implementation that combines the physical part with the numerical part.

In order to validate the model, it is implemented in both 1-dimensional and 2-dimensional situations. In the 1-dimensional situation the Euler equations are solved for a single dimension in combination with source terms that model the varying area distribution of a Venturi-like nozzle. By forcing all three liquids through the nozzle at different velocities and pressures, insight is gained into the general qualitative performance of the model, both physical and numerical. Also the first observations are made concerning the unique cavitation development for each fluid. In order to validate the model quantitatively with test data, the model is implemented into a 2-dimensional situation. A circular rod with a hemispherical head is pointed into the flow to obtain the pressure distribution over the head and part of the rod. This pressure distribution is then compared with data from Rouse & McNown, in order to perform a simple quantitative validation of the model.

Based on the work done in this thesis it is concluded that an isenthalpic barotropic model is a suitable approach to describe cavitation. Due to the independence from empirical relations, the development of cavitation for three different fluids can be modeled, based solely on fluid properties taken from a thermodynamic library. The results from the 1D implementation, followed by a qualitative validation, show that the physical behavior and differences in cavitation development are captured. However, the numerics are influenced by the fluid properties, meaning that it is challenging to tune the numerics in such a way that it treats all possible fluids in an equal manner. The 2D implementation for water shows that the shape of the cavitation region is comparable with images from Rouse & McNown and that the resulting pressure distribution over the head shape is relatively accurate. The 2D implementation of butane and propane shows results that are plausible from a physical standpoint, but remain unvalidated predictions based on the current model. The general results from the 2D implementation are encouraging, but require more work to remedy the numerical instabilities and extremely slow convergence of the solution. The general recommendation for future work is to further develop and improve the numerics to make the solver more efficient and stable, thus viable for bigger simulations.

List of Symbols

Roman Symbols

a	coefficient used in Brennen isenthalpic liquid index	$[-]$
B	parameter used in Tait equation of state	$[-]$
b	coefficient used in Brennen isenthalpic liquid index	$[-]$
C	parameter used in Tait equation of state	$[-]$
c	coefficient used in Brennen isenthalpic liquid index	$[-]$
C_i	domain of cell with index i	$[-]$
c_p	specific heat	$[kJ/kg \cdot K]$
D	thermal diffusivity	$[m^2/s]$
E	bulk modulus	$[Pa]$
E_k	kinetic energy	$[J]$
F	flux vector	*various*
f	autonomous flux function	*various*
F_c	condensation constant in the source terms by Zwart	$[-]$
f_c	constant used in AUSM-scheme	$[-]$
F_e	evaporation constant in the source terms by Zwart	$[-]$
f_L	Brennen isentropic liquid index	$[s^2/m^2]$
f_V	Brennen isentropic vapor index	$[s^2/m^2]$
g_L	Brennen isenthalpic liquid index	$[s^2/m^2]$
g_V	Brennen isenthalpic vapor index	$[s^2/m^2]$
H	head	$[m]$
h	enthalpy	$[kJ/kg]$
I	turbulence intensity	$[-]$
K	coefficient used in Venkatakrishnan's limiter	*various*
k	thermal conductivity	$[W/m \cdot K]$

K_0	constant used in Tait equations of state	$[Pa]$
K_u	constant used in AUSM-scheme	$[-]$
m	mass	$[kg]$
M_0	constant used in AUSM-scheme	$[-]$
N	coefficient used in Tait equations of state	$[-]$
p	pressure	$[Pa]$
p_{G0}	reference partial pressure of gas	$[Pa]$
p_{stat}	static pressure	$[Pa]$
p_{tot}	total pressure	$[Pa]$
Q	vector of conserved variables	$various$
q	quantity of conserved variable	$various$
R	radius	$[m]$
r	ratio	$[-]$
R_0	initial radius	$[m]$
R_b	constant radius of the bubble in the source terms by Zwart	$[m]$
R_g	universal gas constant	$[J/mol \cdot K]$
r_n	nucleation rate of the bubbles in the source terms by Zwart	$[s^{-1}]$
S	surface tension	$[kg/s^2]$
s	entropy	$[kJ/kg \cdot K]$
T	temperature	$[K]$
t	time	$[s]$
U	velocity vector	$[m/s]$
u	velocity component in the x-direction	$[m/s]$
V	volume	$[m^3]$
v	specific volume	$[m^3/kg]$
v	velocity component in the y-direction	$[m/s]$
w	velocity component in the z-direction	$[m/s]$
x	distance	$[m]$
Z	wave speed used in HLLC-scheme	$[m/s]$
$\dot{m}$	massflow	$[kg/s]$
$\hat{F}$	AUSM total flux vector	$various$
$\mathcal{M}$	variable used in AUSM-scheme	$[-]$
$\mathcal{P}$	variable used in AUSM-scheme	$[-]$

Greek Symbols

α	void fraction	$[-]$
β	turbulent viscosity ratio	$[-]$
ϵ	fraction of fluid transferring heat	$[-]$
Γ	mass source term for vapor transport equations	$[kg]$
γ	fluid exponent for CEV equation of state	$[s^2/m^2]$
κ	polytropic exponent	$[unit]$

μ	viscosity	$[Pa \cdot s]$
ϕ	limiter coefficient	$[-]$
ϕ_c	erosion rate	$[mm/h]$
ψ	compressibility	$[Pa^{-1}]$
ρ	density	$[kg/m^3]$
ρ^*	reference density for CEV equation of state	$[kg/m^3]$
τ	viscous stress	$[Pa]$
θ	surface angle	$[rad]$

Superscripts

$\bar{x}$	effective average
x^+	used in AUSM-scheme, analogous to left state
x^-	used in AUSM-scheme, analogous to right state
x^L	left state
x^R	right state

Subscripts

∞	far field or at free stream
b	bubble
c	creation
$crit$	critical
d	destruction
eff	effective value
g	ghost cell
gl	parameter used in Schmidt barotropic model
i	index of a cell
$inlet$	value at inlet
L	left state
l	liquid
lv	liquid to vapor phase change
M	center state
max	maximum
min	minimum
$outlet$	value at outlet
R	rigth state
red	reduced
sat	saturated
t	turbulent
v	vapor
(5)	additional index used for terms in AUSM-scheme

Dimensionless numbers

σ	cavitation number	$\frac{p_{stat}-p_{sat}}{\frac{1}{2}\cdot\rho_\infty U_\infty^2}$
σ_T	Thoma cavitation number	$\frac{NPSH}{H}$
C_p	pressure coefficient	$\frac{p_{stat}-p_\infty}{\frac{1}{2}\cdot\rho_\infty U_\infty^2}$
CFL	Courant-Friedrichs-Lewy number	$\frac{u\cdot\Delta t}{\Delta x}$
M	Mach number	$\frac{u}{c}$
Re	Reynolds number	$\frac{\rho\cdot U\cdot L}{\mu}$

Table of Contents

List of Figures

List of Tables

Preface

In September 2014 I started an internship with Flowserve at their offices in Etten-Leur. The goal of the internship was to obtain a better understanding of the vapor formation in pumps that were utilized as power recovery turbines. After successful completion of the internship project, a possibility was offered to continue working at Flowserve for a thesis project. The goal of the thesis project was to develop the basis for a new cavitation model that can be used for Computational Fluid Dynamics (CFD) calculations. Correct prediction of the shape and intensity of cavitation is an important tool to guarantee that the pump will achieve the performance and the lifetime it was designed for.

About nine months ago I eagerly started to work on this thesis under the impression that it would be very similar to the vapor evolution I researched during my internship. After a month of literature study I was boggled by the complexity of the mechanics and thermodynamics that are associated with cavitation. Cavitation is from both a physical and a numerical perspective a very challenging phenomena to model.

This thesis is submitted in partial fulfillment of the requirements for a Master's Degree in Mechanical Engineering. It contains work done from January to September 2015. The project was performed in-house at Flowserve in Etten-Leur under the daily supervision of dr.ir. F.C. Visser. The project has been done under the supervision of dr.ir. Rene Pecnik of the Process and Energy department at the Technical University of Delft.

This thesis has been solely made by the author. Many of the formulae, scientific data and numerical methods used in the project are based on the research of others. The author has made the best possible effort to provide an actual and correct reference to these sources.

Acknowledgements

This thesis is the final distillate of 9 months of hard work. It was a challenging but extremely interesting project, I worked on it with much pleasure and would like to thank Flowserve for giving me the chance to work on this project. Also, I would like to thank all my colleagues at Flowserve who were always available for a talk or some friendly advice.

I would like to express my gratitude to my supervisor dr.ir. R. Pecnik and to my daily supervisor dr.ir. Frank Visser, first of all for the time they invested in this project, but also for the critical discussions and their guidance when having to make hard decisions. I would also like to thank dr.ir. Mathieu Pourquie and prof.dr.ir. B.J. Boersma for participating in my graduation committee and for the time they committed to reading my thesis.

A special word of thanks is dedicated towards my parents, who have always been there for me and have supported me in many ways. The final word of thanks is dedicated to Lucy, her continuing support and optimism kept me motivated to work hard and keep this project on track.

Delft, University of Technology — Gert-Jan Meijn
September 22, 2015

"When everything seems to be going against you, remember that the airplane takes off against the wind, not with it."

— *Henry Ford*

Chapter 1

Introduction

The purpose of this chapter is to briefly introduce the topic of cavitation and to motivate the goals that are being set to be further explored in this thesis. Also a short background will be given on previous modeling methods that are the main driving force behind this project. The chapter is concluded by an outline of this thesis.

1.1 Introduction

Cavitation is defined as the process of formation and disappearance of a vapor phase in a liquid when this liquid is subjected to reduced pressures, followed by an increase of pressure. The formation of this vapor phase is a process that is almost identical to the boiling of a liquid. The main difference is that boiling is achieved by the addition of heat, thus increasing the temperature of the fluid up till the boiling point. It is normally assumed that cavitation occurs at a more or less constant temperature and that the evaporation of the fluid is caused by lowering the pressure below the saturation pressure at that temperature. Cavitation should not be confused with the flashing of a liquid, since the vapor formed during the flash will remain in the gaseous phase. For this reason cavitation is defined as a thermodynamic change of phase with mass transfer from liquid to vapor phase and the other way around, since the cavitation bubble will again implode when the pressure increases. Figure 1-1 again illustrates the differences between these processes.

The correct prediction of cavitation is not important in the sense that it should be completely avoided. In practice this could be easily achieved by preventing that at any point the pressure falls below the saturation pressure. Even if the pump is correctly designed it is very likely that it will develop some cavitation. But if cavitation is allowed to develop too far it will result in the following negative (possibly damaging) effects:

- performance loss (head loss)
- physical material damage (figure 1-2)

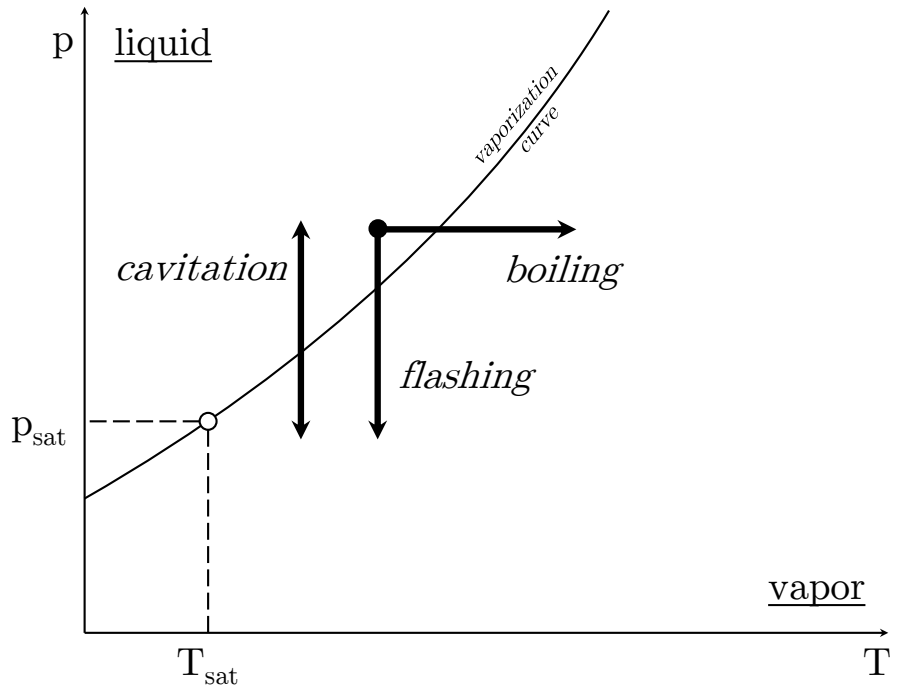

Figure 1-1: Boiling and cavitation illustrated in thermodynamical diagram

- vibrations
- noise

To better illustrate the difference between avoiding cavitation and acceptable levels of (centrifugal pump) cavitation figure 1-3 is used. The figure shows the total head delivered by the pump versus the net positive suction head (NPSH) available to the pump. NPSH is the amount of total suction head above the vapor pressure. Starting on the right hand side of the figure and traveling to the left the amount of NPSH available to the pump is lowered, causing increasing cavitation along the way. Important to note is that the point where cavitation becomes powerful enough to cause damage is not identical to the point of inception, meaning that cavitation can form but will not cause any damage to the surface of the pump. A popular method in industry to describe the allowable levels of cavitation is to look at the actual performance of the pump. The 'NPSH3%' norm determines the minimum amount of NPSH required by the pump before it loses 3% of its head compared to non cavitating operation. This point is indicated as 'Three-Percent Head Drop' in figure 1-3.

Cavitation can occur on many different levels, ranging from a small group of bubbles to a pump that is fully blocked by a big pocket of vapor (better known as 'vapor lock') causing full breakdown of head. Many of the pumps operating in the field are operating with cavitation, but with a level acceptable for their purpose. In some cases it is specified that a pump must always operate above inception (cavitation free) but this will restrict the performance compared to a pump that is allowed to operate with low levels of cavitation. In the end a

Figure 1-2: The resulting damage of continuous cavitation on a pump impeller [1]

certain criterion, based on hours of lifetime or performance, must be defined to determine what level of cavitation is acceptable for the design. Cavitation is an important factor to take into account when designing pumps and cannot be judged by the threshold of vapor pressure alone.

1.2 Tascflow and the CEV-model

Nowadays CFD is the main tool to predict cavitation and many different software packages containing a wide array of models are available to model the behavior of cavitating fluids. Over the years Flowserve has used a small selection of models to predict cavitation and in most cases the fluid of interest was water. The subject of this thesis comes into perspective when the fluid concerned is not water but something like a hydrocarbon or an amine solution. Many of the current cavitation models are based on empirical coefficients which have been experimentally determined in literature but almost solely for water.

May 2000 AEA Technology, a privatized part of the Atomic Energy Authority (AEA), released version 2.10 of their computational fluid dynamics software package CFX-Tascflow. This release contained a new cavitation model, the 'Constant Enthalpy of Vaporization' (CEV) model that utilizes the full solution of mass, momentum and energy to obtain a solution for the amount and location of vapor that is being formed when the local pressure falls below the vapor pressure. The most interesting fact of this model is that it is completely dependent on the actual fluid properties. Meaning that if the user has access to detailed information of the

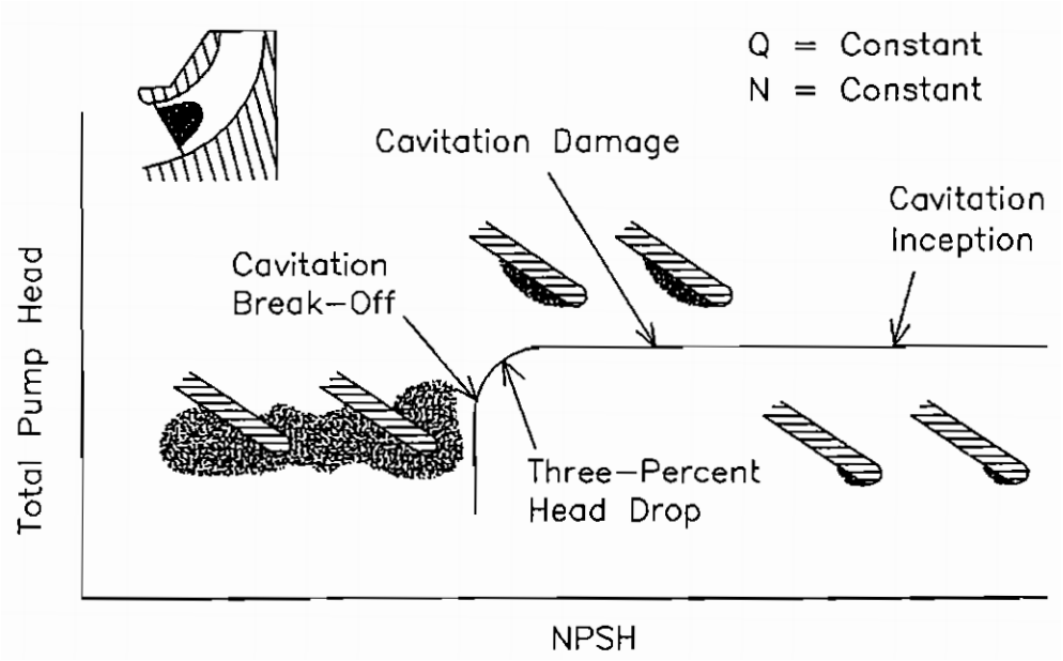

Figure 1-3: Typical stages of pump impeller cavitation [2]

properties of the liquid that is being pumped, it should be possible to fully physical model the cavitation behavior of that fluid. More details about the CEV model and different ways to model cavitation will be discussed in chapter 2 and 3. The cavitation model implemented in Tascflow will be used as an initial reference for the derivation and selection of cavitation models throughout the thesis.

CFX-Tascflow was utilized by Flowserve and led to very satisfactory results, especially when predicting head-drop curves, as can also be seen in the paper by Visser [3]. This is also the main motivation behind the choice for Tascflow as an initial reference. Unfortunately shortly after acquiring CFX-Tascflow it was abandoned by ANSYS and when Flowserve upgraded its computers from Windows XP to Windows 7, it was no longer possible to use CFX-Tascflow. ANSYS never made the step from Windows XP to Windows 7 for CFX-Tascflow and the software package disappeared from the market. Currently Flowserve Etten-Leur uses the ANSYS CFX and Simeric's Pumplinx software packages which only contain a Rayleigh-term model[1]. A cavitation model that is based on physical fluid properties enables to capture the thermodynamic effect on the development of cavitation when pumping hot water or hydrocarbons.

Predicting cavitation on the basis of a Rayleigh-term model has its limitations as from a practical standpoint it is impractical to determine the empirical coefficients needed for each and every fluid. It would involve testing a pump with the same liquid as will be used in the field, which often raises all kind of safety concerns and would be very costly.

[1]Rayleigh-term models or vapor transport models (see chapter 2.2.4) describe cavitation using a transport equation for the vapor that is formed. The mass transfer between phases is governed by a complex source term that is derived from the Rayleigh equation, hence Rayleigh-term model.

1.3 Purpose and motivation

The reintroduction of a model similar to the previously described CEV model, which relies only on physical properties of the fluid itself, would be much more practical. The main driving force behind this thesis project is the desire of Flowserve to again have a cavitation model at its disposal to predict cavitation for fluids other than cold water. Thus this thesis will be focused on the physical modeling of cavitation using an enthalpy based model. The following goals have been set and have been successfully incorporated into this thesis:

- Literature review of available models and their drawbacks, studying the cavitation fluid mechanics and thermodynamics involved
- Develop an accurate barotropic model of the cavitation process utilizing a two-phase isenthalpic expansion
- Guarantee that the model is only dependent on physical fluid properties; no experimental fitting procedure should be required, as is the case with Rayleigh-term models.
- Design of a robust numerical method that can handle the large differences in density, and can overcome other numerical issues like shock waves, discontinuities or spurious oscillations.
- Modification of a density based solver to incorporate the physical models and numerical schemes
- Using the solver to model cavitation for three different liquids: water, butane and propane
- Investigate the influence of a fluid's thermal properties when assuming isothermal flow and referencing fluid properties at this free-stream temperature
- Investigate the role of a fluid's gas-liquid density ratio in a density based solver
- Investigate the practical applicability of the model by focusing on important cavitation details, like cavitation length and the correct modeling of the closure region

The choice to model water, butane and propane is partially based on the practical needs of Flowserve and partially based on the physical properties of the fluids. From a physical point of view the three liquids are quite different. The gas-liquid density ratio ($\frac{\rho_l}{\rho_v}$) for water, butane and propane at $293K$ are respectively 57655, 109 and 28. Also the thermal effect of butane and propane is much larger than that of water. Both these parameter will influence the development of the cavitation as will be shown later on in this thesis. Water is an obvious choice because every shop test is done with water. Butane and propane are candidates to show that the model can predict cavitation behavior based on physical fluid properties. The model will be validated with water based experimental data, butane and propane will remain predictions due to the lack of experimental data.

1.4 Thesis overview

To realize all the goals that have been set in the previous paragraph the thesis is structured to work out each of these goals. To start, an overview of cavitation theory is presented. Cavitation is as much a numerical problem as a physical problem. Each side of the problem is described in its own chapter. The resulting model is then implemented in both a 1D- and a 2D-situation. The results of these models are assessed by comparing them with theory and experimental results.

Chapter 2 provides an extensive overview of the theory related to cavitation phenomena. It will provide further insight into the thermodynamics and fluid mechanics that govern this phenomena. Also the influence of viscosity and surface tension will be discussed, followed by a description of quantities regularly used to describe cavitation. The chapter ends with a description of cavitation modeling methods used in CFD simulations.

Chapter 3 starts with a detailed description of the original CEV model. This is followed by a description and full derivation of the barotropic model by Brennen [4], which will serve as the base for the new and modified CEV model. The modified CEV model is further worked out and verified with Fluidprop [5] to check the isenthalpic nature of the model and the assumptions made. The Tait equation of state [6] is presented that will be used to model the fluid when no cavitation is present. The parameters that are needed to match the CEV model and the Tait equation of state with a certain fluid (water, butane, propane) are presented. It is explained how these parameters are derived from actual fluid data.

Chapter 4 provides the details of the numerical methods involved in the 1D- and 2D-model. The Euler equations in combination with the Finite Volume Method (FVM) are presented. The hybrid AUSM-HLLC [2] scheme used for the convective and pressure fluxes is described in detail. Also special attention is payed to the (non-reflecting) boundary conditions needed for both the 1D- and the 2D-model. The chapter concludes by giving an overview of the entire model, with references to the physical methods describing the full algorithm.

Chapter 5 presents the results that have been obtained using the modified CEV model in an 1D-situation. These results are not compared with experiments since this is not feasible due to the simplified 1D situation. The objective of the 1D-situation is to qualitatively check the physics of the cavitation model and verify that the fluid properties are correctly modeled by the CEV model.

Chapter 6 presents the results that have been obtained using the modified CEV model in an 2D-situation. These results are compared with the experiments by Rouse and McNown [9] to further validate the model and quantify the accuracy of the CEV model. Some parameters of special interest when modeling cavitation (e.g. cavitation length, void fraction, velocity in the closure region) are analyzed with additional care.

Chapter 7 gives a summary of the conclusions of chapters 6 and 7. This is followed by a list of recommendations for future progress on this work.

[2] A combination of the Harten-Lax-van Leer-Contact (HLLC) scheme introduced by Toro [7] and the Advection Upstream Splitting Method (AUSM) scheme introduced by Liou [8]

Chapter 2

Cavitation theory

The purpose of this chapter is to provide an overview of the theory involved with cavitation and to give some practical examples of modeling strategies applied in CFD software packages. The chapter is concluded by discussing the pros and cons of applying a certain modeling strategy.

2.1 Cavitation theory

The process of cavitation can be divided into three distinct steps. The first step is the initial formation of a bubble, another name for this part is the inception of cavitation. After the initial formation (or inception) the bubble enters the next step, namely the growth step, where the bubble will grow to a certain size, controlled by the forces (pressures) acting on the bubble. Note that the collapse of the bubble is the main difference between actual cavitation and the flashing of a liquid to a vapor. Flashing a liquid involves the same phase change (liquid to vapor) but the formed vapor will not turn back into a liquid.

Different authors have focused on different parts of the cavitation cycle, since each phase has its own unique characteristics, driving forces and timescales. The practical interest is also different for each step. For instance, the modeling of the collapse of the bubble is largely focused on accurately predicting the forces involved to update models that are used to predict the damage caused by cavitation bubbles. Another example is inception behavior, which is studied intensively by the medical industry. Their goal is to accurately predict the location, amount and size of the bubbles formed by their cavitation inducing devices used to destroy kidney stones [10].

2.1.1 Types of cavitation

As described in the introduction, the definition of cavitation is the process of formation and disappearance of a vapor phase in a liquid when this liquid is subjected to reduced pressures, followed by an increase of pressure. But depending on the fluid flow regime and the shape

the fluid is flowing over, many different types of cavitation can be formed. The following five cavitation types are reviewed: bubble, sheet, cloud, vortex and super cavitation. Do note that these are typical and relatively clear examples of a certain cavitation type, it is very well possible to create cavitation regimes that are a combination of or transition between these five types.

Much of the theory from the previous and coming paragraphs is concerned with a single cavitation event, meaning a single (perfectly spherical) bubble. When these bubbles start to form larger groups, and start to influence and alter the flow surrounding them, different types of cavitation can be formed.

Bubble cavitation (figure 2-1) can be recognized by the individual bubbles that travel through the flow field. These bubbles can be attached to a surface but can also detach and travel with the flow. This cavitation generally occurs in low mass flow rate machines with a relatively uniform pressure distribution across the surface. This type of cavitation is very harmful and erosive since very large amounts of energy are transmitted to the surface when these large bubbles collapse.

Sheet cavitation (figure 2-2) or blade attached cavitation is the next phase in the cavitation process when the cavitation number is lowered further or the angle between the flow and the hydrofoil is increased. The larger bubbles coalesce to form a single sheet that starts closely downstream of the stagnation point of the geometry, for instance a little after the leading edge of a hydrofoil. This form of cavitation is sometimes described as 'fully developed' cavitation because the sheet can keep a steady shape with a very clear and sharp interface between the phases. In general the velocities for sheet cavitation are higher than for bubble cavitation, but the individual bubbles are much smaller which means that this form of cavitation is generally perceived as less noisy.

Cloud cavitation (figure 2-3) looks very similar to sheet cavitation except for the fact that this cavitation is much less attached to the surface. In general the convecting velocities are higher for cloud cavitation than for sheet cavitation, causing the top layer of the sheet to become unstable. The shedding of these clouds from the main sheet is not completely random but knows a certain temporal periodicity that for instance can be described by the Strouhal-number. In rotodynamic machinery this periodicity can be caused by perturbations induced by the machinery itself. The interaction between the impeller blades and the volute cutwater inside a centrifugal pump is an example of such a perturbation.

These clouds of cavitation can be very damaging depending on the location where they collapse. For hydrofoils these clouds are convected away from surface and implode somewhere with the main flow, which is harmless for the hydrofoil. But inside a pump this cloud can be convected to a high pressure zone somewhere near a wall, causing the entire cloud to implode instantaneous resulting in a loud bang and high local erosion rates.

Vortex cavitation (figure 2-4) occurs in zones of very high vorticity. The tip of a ship propeller is an example of a high vorticity region. In the center of the vortex the pressure is lower causing the fluid to cavitate. The shape of vortex cavitation is thus determined by following the local vorticity contours, resulting in long 'ropes' of cavitation. Centrifugal forces play a very important role in vortex cavitation. Firstly these forces cause the pressure to be lower in the center of the vortex, correlating high vorticity with the pressure drop in the center. Secondly in the work of Higuchi et al. [11] it has been hypothesized that the centrifugal forces

are also responsible for the smooth shape of these cavitation 'ropes'. Higher centrifugal forces would cause the bubbles to be pushed towards the center of the vortex, creating smoother looking cavitation.

Super cavitation (figure 2-5) looks very similar to sheet cavitation but the difference is in the location of the closure region. When sheet cavitation forms on a hydrofoil, it is possible to stretch the cavity from the leading further back to the trailing edge of the hydrofoil by increasing the angle between the hydrofoil and the flow. If the velocities are sufficiently high it is possible to stretch the cavity to the point where it closes behind the trailing edge of the hydrofoil. This situation is an example of super cavitation. The principle is used by torpedoes to form a sheet enclosing the entire torpedo, drastically reducing the drag forces under water [12].

A final note is directed to the simulation of these different cavitation types. Some of the previously described cavitation types posses a steady state, for example sheet cavitation or super cavitation, which on the scale of individual bubbles are very chaotic but form large stable structures on a large scale. From a computational perspective it costs much less resources to compute a stable flow structure than predict the convection of a cloud of vapor traveling through the domain.

Figure 2-1: Example of bubble cavitation [13]

2.1.2 Quantities and dimensionless numbers

To correctly compare and scale cavitation across different fluids and geometries, a group of dimensionless numbers and relevant quantities is introduced. The following dimensionless numbers and quantities are maintained for this report:

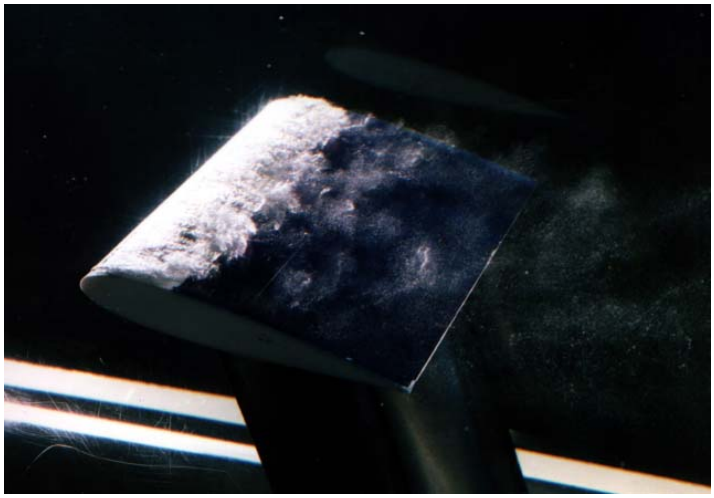

Figure 2-2: Example of sheet cavitation [13]

Figure 2-3: Example of cloud cavitation [13]

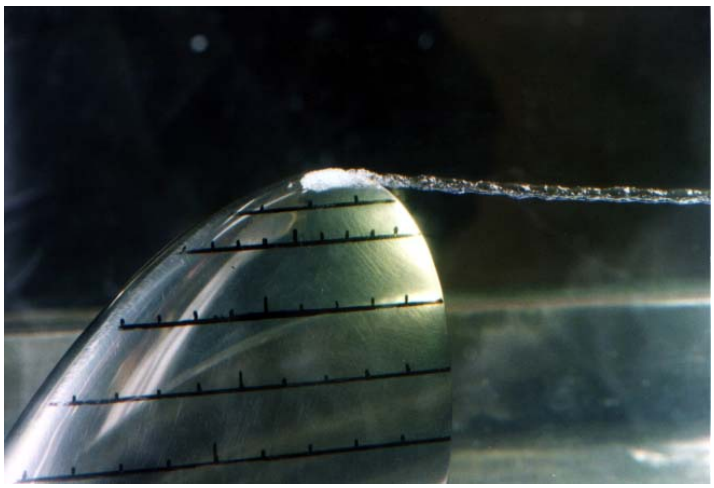

Figure 2-4: Example of vortex cavitation [13]

Figure 2-5: Example of super cavitation [13]

$$\alpha = \frac{V_v}{V_l + V_v} \tag{2-1}$$

$$x = \frac{m_v}{m_l + m_v} \tag{2-2}$$

$$p_{tot} = p_{stat} + \frac{1}{2}\rho v^2 \tag{2-3}$$

$$H = \frac{p_{tot}}{\rho \cdot g} \tag{2-4}$$

$$NPSH = \frac{p_{tot} - p_{vap}}{\rho \cdot g} \tag{2-5}$$

$$C_p = \frac{p_{stat} - p_\infty}{\frac{1}{2}\rho v^2} \tag{2-6}$$

$$\sigma = \frac{p_{stat} - p_{vap}}{\frac{1}{2}\rho_\infty v_\infty^2} \tag{2-7}$$

$$\sigma_T = \frac{NPSH}{H} \tag{2-8}$$

- void (volume) fraction α: fraction of the total volume that is occupied by the vapor phase
- mass fraction x: fraction of the total mass that is occupied by the vapor phase
- total pressure p_{tot}: the sum of the static and the dynamic component of the pressure
- head H: the height of a incompressible column of fluid which is equivalent to the energy of that fluid
- net positive suction head $NPSH$: The amount of total head above vapor pressure
- pressure coefficient C_p: the ratio of static and dynamic pressure forces

- cavitation number σ: the ratio of the static pressure difference between free-stream and vapor pressure and the dynamic pressure at free-stream
- Thoma cavitation number σ_T: ratio between the net positive suction head and the local head. Considered to be archaic standard for defining cavitation, may be found in older references.

2.1.3 Inception

The first step of cavitation is the 'birth' of the bubbles, better known as the inception of cavitation. The bubbles emerge in the liquid due to nucleation. Nucleation can be divided in two categories, homogeneous and heterogeneous nucleation. Homogeneous nucleation involves the creation of a new phase in the midst of the liquid, away from any surfaces. Heterogeneous nucleation involves the creation of a new phase by using nucleation sites, which are zones on the surface on which the new phase is formed.

In most practical situations it is impossible to create cavitation through homogeneous cavitation. Homogeneous nucleation would imply that the fluid is pulled and eventually torn apart to make space and create an interface between the two phases. The governing equation behind this statement is [4]:

$$p_b - p = \frac{2S}{R} \tag{2-9}$$

Assuming surface tension to be equal to $S = 0.05N/m$ and that the radius r of the bubble is equal to a single intermolecular distance unit in the order of $10^{-10}m$, the pressure difference would be in the order of 10,000 bar of pressure. The calculation shows that it is near impossible to create homogeneous nucleation under practical circumstances.

An interesting observation is that in early papers concerning cavitation researchers (Berthelot [14], Dixon [15]) reported seeing bubbles appear in the center of the fluid, suggesting homogeneous cavitation, having only applied a tensile pressure in the order of 100 bar. What in fact was happening is that these researchers observed heterogeneous nucleation of cavitation, that used nucleation sites on impurities that were drifting through the flow. Figure 2-6 provides a few examples on possible shapes for nucleation sites. Note that the bubbles are no longer spherical but have a certain contact angle θ at the vapor-liquid interface. The governing equation as was described by equation 2-9, is now rewritten to include the effect of this angle θ:

$$p_b - p = \frac{2S \cdot sin\theta}{R} \tag{2-10}$$

For example A and B in fig 2-6 this would mean that the tensile pressure goes towards zero if $\theta \to \pi$. Example B, showing the hydrophilic surface, this means making a spherical bubble that would be identical to homogeneous nucleation. Example A, showing the hydrophobic surface gives a possible explanation to why heterogeneous nucleation lowers the tensile pressure needed, the tensile pressure goes towards zero if $\theta \to 180°$, which would be possible for very flat bubbles on very hydrophobic surfaces. Both A and B fail to illustrate why nucleation is possible close to vapor pressure.

A realistic surface is not perfectly flat, the cast steel impeller of a pump is covered with surface imperfections, much like example C in fig 2-6. If half-angle α at the bottom of the

cavity is taken in to account for equation 2-10, the angle for zero tensile strength θ becomes $\theta = \alpha + 90°$. The value of alpha is well within in a range that could be encountered on the surface of actual materials. If the situation would occur that $\theta > \alpha + 90°$ it is even possible to have nucleation sites that operate well below the vapor pressure. From all the above it can be concluded that homogeneous nucleation is highly unlikely and that the inception of cavitation most likely will occur inside small imperfections that are found across the surface of the geometry involved.

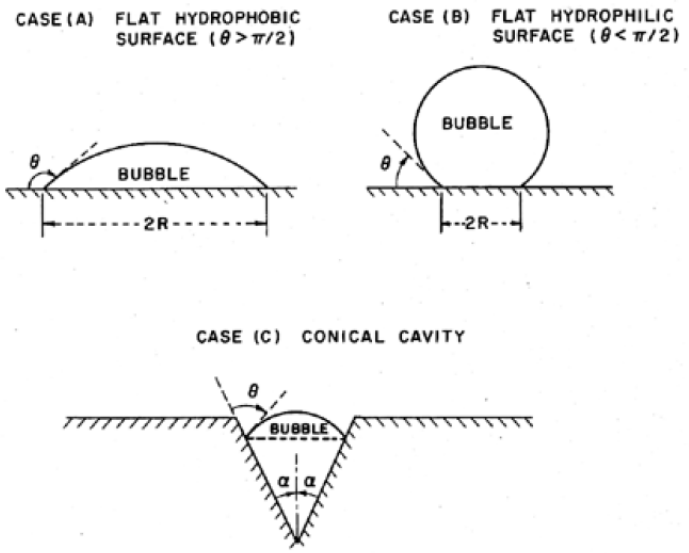

Figure 2-6: Different sites for heterogeneous nucleation [4]

2.1.4 Growth

The step that follows after the inception of the cavitation bubble is the growth step. The growth step is governed by the Rayleigh-Plesset equation, which describes the radius of the bubble as a function of time, thus also including all the transient effects of bubble growth [16]:

$$\begin{aligned} \frac{p_b(t) - p_\infty(t)}{\rho_l} + \frac{p_{sat}(T_b) - p_{sat}(T_\infty)}{\rho_l} + \frac{p_{G0}}{\rho_l}\left(\frac{T_b}{T_\infty}\right)\left(\frac{R_0}{R}\right)^{3\kappa} \\ = R\frac{d^2R}{dt^2} + \frac{3}{2}\left(\frac{dR}{dt}\right)^2 + \frac{4\nu_l}{R}\frac{dR}{dt} + \frac{2S}{\rho_l R} \end{aligned} \tag{2-11}$$

This equation is built up from a set of terms that denote the individual contributions of the forces that work on or from the inside of the bubble:

- 1: $R\frac{d^2R}{dt^2} + \frac{3}{2}\left(\frac{dR}{dt}\right)^2$ - inertial forces
- 2: $\frac{4\nu_l}{R}\frac{dR}{dt}$ - viscous forces

- 3: $\frac{2S}{\rho_l R}$ - surface tension
- 4: $\frac{p_b(t)-p_\infty(t)}{\rho_l}$ - driving pressure
- 5: $\frac{p_{sat}(T_b)-p_{sat}(T_\infty)}{\rho_l}$ - thermal effect
- 6: $\frac{p_{G0}}{\rho_l}\left(\frac{T_b}{T_\infty}\right)\left(\frac{R_0}{R}\right)^{3\kappa}$ - bubble content state term

The equation is derived from the Navier-Stokes equation, assuming perfectly spherical bubbles. Terms 1,2 and 3 are governing the mechanics of the bubble. Term 4 is the main driving force, forcing a time-dependent external pressure $p_\infty(t)$ on the bubble. Term 5 is the so called 'thermal effect' that arises due to the temperature difference that can be formed when part of the fluid is evaporated. Term 5 will be discussed in more detail in 2.1.7. Term 6 is often omitted from the Rayleigh-Plesset equations, it describes the influence of the gas on the inside of the bubble (at partial pressure p_{G0}) using a state-like equation (with polytropic coefficient κ). Note that if all transient terms are stricken from the equation, the bubble contents are ignored and the thermal effects are assumed negligible, the static solution is equal to equation 2-9.

The Rayleigh-Plesset equation is a second-order differential equation, meaning that the are stable and unstable solutions. Stable solutions will result in stable growth or shrinkage to a new bubble radius according to the imposed pressure. The bubbles do have a minimum size, meaning that they will eventually become so small that mass diffusion from the surrounding liquid will dissolve the remaining gas, making the bubble disappear [17].

2.1.5 Collapse

The unstable solutions, caused by a sudden decrease in pressure followed by an increase of pressure, will respectively lead to an explosive growth followed by the collapse of a bubble. The difference between controlled shrinkage and full collapse of a bubble lies with the so called 'Blake threshold pressure' [18]. Blake defined this critical threshold to be equal to:

$$p_{b,crit} = p_{vap} - \frac{4S}{3}\left(\frac{8\pi S}{9km_vT_bR_g}\right)^{\frac{1}{2}} \tag{2-12}$$

In which κ is equal to the polytropic coefficient, m_v is equal to the mass of the vapor in the bubble and R_g is equal to the universal gas constant ($8.314\ J/mol \cdot K$). If the pressure is lowered from p_0 to a pressure that is still above $p_{b,crit}$, the bubble will grow in a controlled manner until the pressure gradient is reversed, causing the bubble to shrink back to its original size. If the pressure is lowered from p_0 to a pressure that is below $p_{b,crit}$, the bubble will grow explosively (uncontrolled) until the pressure gradient is reversed, but for this scenario the bubble will collapse. The increased growth rate during the explosive expansion causes an overshoot when the bubble is shrunk back to its original size and due to the increasingly important role of surface tension, the rate of collapse will increase further. Eventually the two bubble walls will hit each other, the energy converted by this collapse will cause very high local pressure and very high local temperature also releasing shock waves from the bubble walls that are traveling faster than the speed of sound.

Figure 2-7: Close-up picture of the collapse of a single cavitation bubble [19]

If this collapse occurs somewhere in the main stream, far away from any surface, the bubble will be split in two or more bubbles. Although relatively high amounts of energy are converted, only the shock waves are felt by the surrounding boundaries generally not causing any damage to the surface material of the boundary. Damage by cavitation occurs when the collapse of the bubble is close to a boundary (distance to the boundary in the order of the bubble diameter). The flow and pressure surrounding the bubble will be influenced by the (rigid) wall resulting in the formation of a so called 'micro jet' as can be seen in fig 2-7. The piercing damage caused by this 'micro jet' results in small pits (cavities) in the surface. If the cavitation is allowed to persist over longer periods of time, the surface will become heavily damaged, as shown in figure 1-2.

2.1.6 Thermodynamics

In order to model the phase change between the liquid and the fluid it is important to realize that not only mass is transfered between phases but that heat is also transfered between phases in order to make the jump from liquid to vapor. The inception, growth and collapse as described previously are mainly described from the viewpoint of mechanics, ignoring the heat transfer.

One way of approaching the heat transfer is to assume that the two phases are always in thermodynamic equilibrium. The mixture is assumed to be perfectly homogeneous, the liquid and the vapor are dispersed so finely that they are in contact with each other in the entire mixture. This would imply that heat transfer occurs instantaneous, because the two phases are in perfect thermal contact. This model is called the 'homogeneous equilibrium model' and has applied been applied to cavitation in the work of Xie et al [20] and Khoo [21].

The opposite is to completely ignore heat transfer in the model, thus assume that the phase change occurs without any heat transfer or that the heat transfer is infinitely slow. This model is called the 'frozen flow model'. The actual physical truth lies somewhere in between these models; the real mixture will have finitely dispersed phases. Part of the mixture will be in contact to transfer heat, but the other part is separated and will not transfer heat. The

'frozen flow model' has been applied to cavitation in the work of Bouziad [16] and d'Agostino & Raposelli [22].

2.1.7 Thermal influences and effects

In the introduction it was made clear that cavitation is not identical to boiling, since boiling is largely temperature controlled at almost constant pressure and cavitation is largely pressure controlled at almost constant temperature. This however does not mean that the cavitation process is completely independent of temperature. The properties of the fluid dictate how much temperature will play a role. To illustrate this principle the three fluids of interest for this thesis are compared; water, butane and propane. The relevant physical properties are listed in table 2-1.

Table 2-1: Physical properties of water, butane and propane

fluid name	water	butane	propane	unit
library	IF97	RefProp	RefProp	-
temperature	293.15	293.15	293.15	K
density - liquid - ρ_l	998.1608	578.5912	500.0569	kg/m^3
density - vapor - ρ_v	0.0173	5.3126	18.0823	kg/m^3
ratio	57655	109	28	-
latent heat - h_{lv}	2453550	366501	344314	J/kg
specific heat - liquid - $c_{p,l}$	4185.10	2412.85	2666.21	$J/kg \cdot K$
thermal conductivity - liquid - k_l	0.5984	0.1067	0.0961	$W/m \cdot K$
thermal diffusivity - liquid - D_l	$1.433 \cdot 10^{-7}$	$7.646 \cdot 10^{-8}$	$7.206 \cdot 10^{-8}$	m^2/s

When the fluid undergoes a phase change it will need energy from its surroundings, equal to the heat of evaporation to complete this change. If a cavitation bubble is formed, it will take away this heat from the surrounding liquid causing a local decrease in the temperature of the surrounding liquid. As observed in chapter 1.1 and figure 1-1 the saturation pressure is a function of temperature, when the temperature is decreased, the saturation pressure will also decrease. Combining these effects will result in a phenomena called the thermal suppression of cavitation. To analyze the sensitivity of a fluid to this effect, a coefficient has been derived by Brennen starting from a heat balance involving a mass of liquid and a (newly formed) mass of vapor:

$$m_v \cdot h_{lv} = m_l \cdot c_{p,l} \cdot \Delta T \tag{2-13}$$

$$m = \rho \cdot V \tag{2-14}$$

$$\rho_v \cdot V_v \cdot h_{lv} = \rho_l \cdot V_l \cdot c_{p,l} \cdot \Delta T \tag{2-15}$$

$$\Delta T = \frac{\rho_v \cdot V_v \cdot h_{lv}}{\rho_l \cdot V_l \cdot c_{p,l}} \tag{2-16}$$

The actual derivation of Brennen is more complicated, as it is based on the Rayleigh-Plesset equation but follows the same principle as described by equations 2-13 through 2-16. The interested reader is referred to his book on cavitation [4]. To relate the local reduction in temperature to a change in vapor pressure (suppression pressure) and eventually to fluid properties, the Clausius-Clapeyron relation was used by Brennen:

$$\frac{dp}{dT} = \frac{h_{lv}}{T \cdot (V_v - V_l)} \tag{2-17}$$

The diffusion and conduction of heat through the bubble and interface were also included by Brennen to provide a very compact but complete parameter that describes the influence of thermal properties on the total cavitation behavior. The final result will be the so called Brennen thermal parameter Σ:

$$\Sigma(T) = \frac{h_{lv}^2 \cdot \rho_v^2}{\rho_l^2 \cdot c_{p,l} \cdot T_\infty \cdot D_l^{\frac{1}{2}}} \tag{2-18}$$

$$D_l = \frac{k_l}{c_{p,l} \cdot \rho_l} \tag{2-19}$$

In table 2-2 the Brennen parameter for each fluid is calculated at 293K based on the data in table 2-1. The local gradient of vapor pressure as function of temperature Pa/K is defined by the Clausius-Clapeyron relation (equation 2-17) and also provided in table 2-2. The resulting values are clear, water is a very weak function of temperature at 293K. Butane and propane are still very dependent on temperature at 293K. The choice to model cavitation with a barotropic model, thus not including temperature dependencies, may not be ideal for fluids that score relatively high on the Brennen parameter. The barotropic model is validated in chapter 3.2.4. The assumption to base all fluid properties on free-stream temperatures will be thoroughly reviewed in chapter 3.2.5.

Table 2-2: Thermal parameters of water, butane and propane

fluid name	water	butane	propane	unit
library	IF97	RefProp	RefProp	-
Clausius Clapeyron	144.9	6703.4	22035.1	Pa/K
Brennen therm. parameter	3.9	57899.3	738842.6	-

2.2 Cavitation modeling in CFD

Over the years many different methods have been developed to model cavitation in CFD applications. One should be aware that each of these methods has its own area of application and depending on the application some methods will be computationally too expensive to

even consider. For instance, the interface tracking method is intended to model the bubble dynamics of a single bubble with very high detail. If this method were to be used for an entire cloud of bubbles the calculation would simply take too long. It would be more advisable to model this cloud of bubbles as a different phase with a lower density by using a vapor transport model or a barotropic model. Another important choice lies with the fact that the cavitation can be modeled as compressible or incompressible. The incompressible modeling of cavitation is generally associated with empirical models that directly create or destroy vapor based on the pressure field present. This allows for a time step that is much bigger than the physical time scale of the problem. Fully compressible modeling of cavitation is completely governed by the physics of the problem, meaning that the user should provide information on the behavior of the fluid in the form of an equation of state or a simplified barotropic expression. The main disadvantage is that the problem is bounded by physical timescale of the problem to keep the solution stable. In practical application, for instance a cavitating water flow, this means that the allowable time step will be around $\mathcal{O}\left(10^{-8}\right)$. More details on the difference between compressible and incompressible time step size is given in chapter 4.1.

2.2.1 Interface tracking

This method focuses on the interface between the bubble and the surrounding fluid. It utilizes the previously discussed Rayleigh-Plesset equation, possibly with additional interaction terms, to describe this interface in very high detail. The interested reader can read more on these algorithms and mathematical methods in the work of Chen and Heister [23]. These interface tracking methods are often used in conjunction with a type of VOF (Volume Of Fluid) method. These VOF-methods are used to give additional accuracy in describing the interface between the liquid and the gas. The main advantage of these methods is that they provide an extremely sharp interface since the interface is always contained by a single cell, thus having a relatively fine mesh will result in sharp interfaces. Due to computational limits it can be applied on a single bubble or on a group of bubbles to study the interaction between them. It should be stressed that these kind of models are not applicable to large cavitating structures as shown in chapter 2.1.1 when using highly detailed interface models. It is possible to use a very simplified type of these models to study large scale cavitation in hybrid Eulerian-Lagrangian simulations [24].

2.2.2 Barotropic modeling

Since the main goal of this thesis is to model cavitation using a barotropic model, several existing barotropic models from literature are analyzed and their strengths and weaknesses are identified. As mentioned before, barotropic models are used in the compressible modeling of cavitation and are bound by very small physical time steps to obtain stable solutions.

The simplest barotropic model is obtained by assuming a certain mathematical shape that provides a smooth transition from the liquid phase to the vapor phase as the pressure decreases. The relation between these barotropic models and the physical properties of the fluid is very weak. The vapor and liquid densities are used as outer limits of the function, but the only parameter to control the shape of the curve is the minimum value of the speed of sound. Typically at $p = p_{sat}$ the gradient of the curve is set to $1/c_{min}^2$ (see also chapter 2.2.3).

The first example is from Kueny and Delannoy [25], who used the first quarter period of a sine to provide the smooth transition. The advantage of this method is that it is easy to implement in existing codes. Another advantage is the fact that the user is to choose equations of state for the pure liquid and pure vapor phase, since the sine function has to be cut at zero and after a quarter of its period. The main disadvantage of this method is that the sine function has no physical meaning, it is an arbitrary function to connect the two phases. An example of the model is shown in figure 2-8 for water at 293K, assuming that c_{min} is equal to 1 m/s. The barotropic model by Kueny and Delannoy [25] is defined by the following equation:

$$\rho = \frac{\rho_l + \rho_v}{2} + \frac{\rho_l - \rho_v}{2} \cdot sin\left(\frac{p - p_{sat}}{c_{min}^2} \cdot \frac{2}{\rho_l - \rho_v}\right) \tag{2-20}$$

A very similar model has been used in the work by Koop [26]. The general idea is identical to the work of Kueny and Delannoy except that Koop opted for a hyperbolic tangent instead of a sine function to make the transition and rewritten the pressures to be dimensionless. The function is just as easy to implement as the sine based function. A hyperbolic tangent has two asymptotes, at 1 and -1. The advantage is that, if the function is rescaled to operate between liquid and vapor density, it is always limited. However, it is not possible to choose separate equations of state for the pure liquid and pure gas phase, these too are modeled by the hyperbolic tangent. An example of the model is shown in figure 2-8 for water at 293K, assuming that c_{min} is equal to 1 m/s, U_∞ is equal to 1 m/s and that P_∞ is equal to $1 \cdot 10^5 Pa$. The barotropic model by Koop is formed by the following equations:

$$\rho = \frac{1}{2}\left(\frac{\rho_l + \rho_v}{2} + \frac{\rho_l - \rho_v}{2} \cdot tanh\left(\frac{C_p - \sigma}{\frac{\rho_l - \rho_v}{\rho_l}} \cdot \frac{U_\infty^2}{a^2}\right)\right) \tag{2-21}$$

$$a^2 = \frac{\left(\frac{dP}{d\rho}\right)_{min}}{\frac{\rho_l - \rho_v}{\rho_v}} = \frac{c_{min}^2}{\frac{\rho_l - \rho_v}{\rho_v}} \tag{2-22}$$

The final barotropic model is provided by Schmidt [27]. The general approach of this barotropic model is quite different compared to the previous two. Instead of using a mathematical function to interpolate between the states, this method uses the fact that by integrating the speed of sound one can also obtain a barotropic relation. Chapter 2.2.3 and chapter 3 provide more details on this method. The barotropic model by Schmidt is formed by the following equations:

$$p = p_{sat} + p_{gl} \cdot ln\left[\frac{\rho_v \cdot c_v^2 \cdot \rho_l \cdot c_l^2 \cdot (\rho_l + \alpha\,(\rho_v - \rho_l))}{\rho_l \cdot (\rho_v \cdot c_v^2 - \alpha\,(\rho_v \cdot c_v^2 - \rho_l \cdot c_l^2))}\right] \tag{2-23}$$

$$p_{gl} = \frac{\rho_v \cdot c_v^2 \cdot \rho_l \cdot c_l^2 \cdot (\rho_v - \rho_l)}{\rho_v^2 \cdot c_v^2 - \rho_l^2 \cdot c_l^2} \tag{2-24}$$

$$p_{min} = -p_{gl} \cdot ln\left[\frac{\rho_v^2 \cdot c_v^2}{\rho_l^2 \cdot c_l^2}\right] \tag{2-25}$$

Compared to the previous two methods, this method is more related to the physical properties of the liquid, using the speed of sound and the vapor pressure in addition to the density of

both phases. The main disadvantage lies in the fact that resulting barotropic relation has numerical problems. Equation 2-25 gives an expression for p_{min}, which is minimum value that can be selected for p_{sat} to guarantee that the pressure remains positive for the entire density range. The paper by Khoo [21] illustrates that if the ratio between liquid and vapor density is equal to 1000, the minimum allowed pressure for the model is equal to 18.3 bar. This would also imply that the vapor pressure cannot be lower than 18.3 bar if the pressure should remain positive. This restriction complicates the implementation of the model, a numerical workaround has to be created in order to prevent the model from giving negative pressures as an output. An example of the physical correct fluid properties is shown in figure 2-8 (star markers) for water at 293K, clearly showing that physically correct fluid properties do not lead to a satisfying correlation between pressure and density. Another example of the Schmidt model is shown in figure 2-8 (triangle markers) but the values have been altered to represent satisfactory behavior of the model. The density of the vapor is lowered even further ($\rho_v = 0.0010 kg/m^3$) and for both cases the pressure has to be shifted to ensure that the curvature changes sign at $p = p_{sat}$.

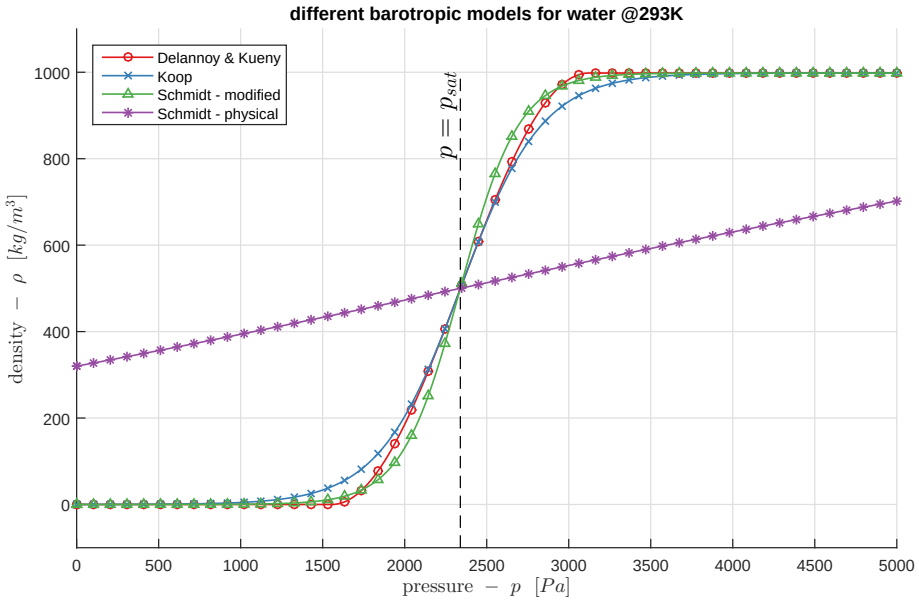

Figure 2-8: Barotropic curves of water at $293K$ using the models by Delannoy & Kueny [25], Koop [26] and Schmidt [27]

2.2.3 Speed of sound in relation to barotropic models

As previously observed in the barotropic relation by Schmidt, it is possible to derive a barotropic relation for a liquid if a function for the speed of sound is available. Per definition the following is true:

$$c^2 = \left(\frac{\partial p}{\partial \rho}\right)_s \tag{2-26}$$

$$c^2 = \frac{E}{\rho} \tag{2-27}$$

The gradient of a barotropic relation is equal to the compressibility of that fluid, which is again equal to the inverse of the speed of sound squared. Although the shapes of the sine function and the hyperbolic tangent used by Delannoy & Kueny [25] and Koop [26] respectively are not very physical, the slopes of the functions are related to the speed of sound, even though it is for a single point $\left(\frac{d\rho}{dp} = \frac{1}{c^2_{min}} \text{ for } p = p_{sat}\right)$. The previously discussed barotropic model by Schmidt is based on the assumption that the speed of sound can be modeled by an isentropic two-phase mixture. According to various sources, Wallis being the first [28], the speed of sound in an isentropic mixture can be described with the following expression:

$$\frac{1}{c^2} = \rho\left(\frac{\alpha}{\rho_v \cdot c_v^2} + \frac{1-\alpha}{\rho_l \cdot c_l^2}\right) \tag{2-28}$$

The minimum speed of sound is generally found when the fluid is a 50-50 volumetric mixture of gas and liquid ($\alpha = 0.5$) as can be observed in figure 2-9. The actual value of c_{min} is hard to predict and empirical data is also very limited on this subject. Work done by Karplus [29] and Gouse and Brown [30] is both focused on a bubbly mixture of water and air, no reference has been found on a fluid different from water. The (isothermal) experiments performed by Karplus and Gouse & Brown confirm that the minimum speed of sound at atmospheric pressure for a bubbly mixture of water and air is found at $\alpha = 0.5$ and that the speed of sound is equal to 21.3 and 18.7 m/s respectively. The calculated value of the isentropic model (equation 2-28) is equal to 23.6 m/s. It is concluded that the isentropic model gives a satisfactory approximation for the minimum speed of sound in a two-phase mixture and is a suitable candidate for a simple barotropic model. The resulting barotropic model, the Schmidt model still has some numerical issues, as described in chapter 2.2.2. Also note that the speed of sound cannot be linearly interpolated between the liquid state (1545 m/s) and the vapor state (472 m/s), the minimum value is far below any linear combination of the two. If void fraction α is not close to the asymptotic values of 0 or 1, equation 2-28 can be approached by:

$$\frac{1}{c^2} \sim \alpha\,(1-\alpha)\,\frac{\rho_l}{p} \tag{2-29}$$

Which results in $c_{min} \approx 20\ m/s$ for water at 1.013 bar, 50% void fraction.

2.2.4 Transport equation modeling

As mentioned before, transport equation based models are mostly used in the incompressible modeling of cavitation and are able to make much bigger time steps than the compressible modeling methods. In most commercial CFD packages this is the reason that transport equation based models are preferred. To give an example; simulating 10 revolutions for a pump that is rotating at 3000 rpm would require 0.2 seconds of physical time. With an average time step of 10^{-8} this will require 20 million iterations to complete on a compressible solver. If the same simulation is performed on a incompressible solver it can be executed with

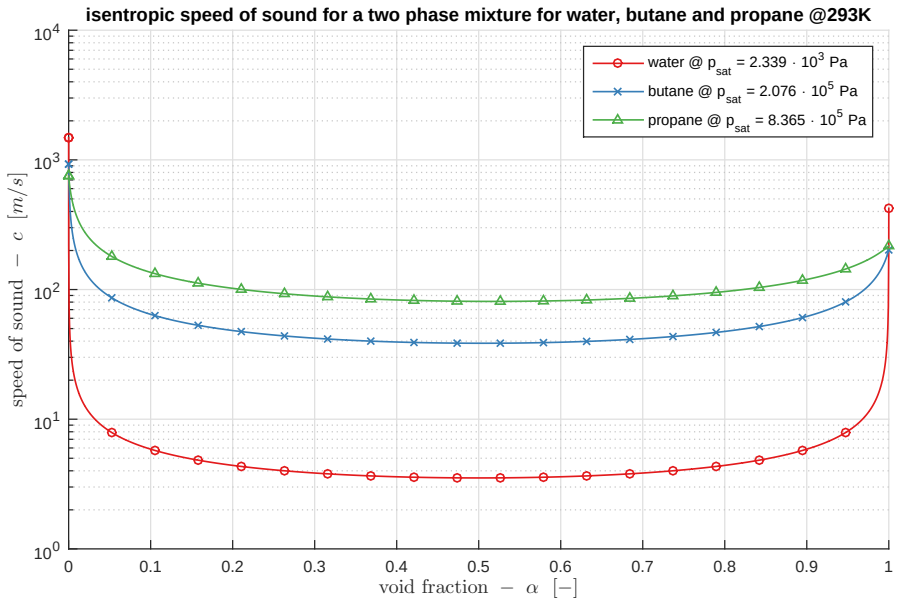

Figure 2-9: Isentropic speed of sound as a function of void fraction for $p = p_{sat}$ for all three fluids(water, butane and propane) at 293K

a time step that is roughly 100 times bigger, based on the CFL number[1] [31]. The difference between the compressible and incompressible CFL number can be found in chapter 4.1.

The general concept behind the vapor transport model is that the density is calculated through the void fraction α (as defined in equation 2-1) and that the void fraction is directly solved and influenced by source terms. The governing equation of the vapor transport models is:

$$\frac{\partial(\alpha\rho)}{\partial t} + \nabla \cdot (\alpha\rho U) = \Gamma \tag{2-30}$$

$$\Gamma = \dot{m}_c + \dot{m}_d \tag{2-31}$$

$$\dot{m}_c = F_e \frac{3r_n}{R_b} (1-\alpha)\, \rho_v \sqrt{\frac{2}{3}\frac{p_{sat}-p}{\rho_l}} \tag{2-32}$$

$$\dot{m}_d = -F_c \frac{3\alpha}{R_b} \rho_v \sqrt{\frac{2}{3}\frac{p_{sat}-p}{\rho_l}} \tag{2-33}$$

Equation 2-32 and equation 2-33 show the creation and destruction source term respectively. The source terms shown in these equations are the work of Zwart [32], but many others (Singhal [33], Kunz [34]) have suggested source terms based on different approaches. The source terms of Zwart still contain a few parameters that can be tuned to best represent the cavitating behavior of water. For water at 293K the following parameters, based on experiments, are considered the default values for this fluid [35]:

[1]The Courant-Friedrichs-Lewy (CFL) number is a dimensionless number that indicates the stability of an explicit numerical scheme. Any time step that results in a CFL number larger than 1 will generally cause the solution to destabilize. Implicit schemes can have a arbitrarily large CFL number, depending on the time stepping scheme used, a larger CFL number will lead to a lower numerical accuracy in time.

- $F_e = 50$
- $F_c = 0.01$
- $r_n = 5 \cdot 10^{-4}$
- $R_b = 10^{-6}$

Although these values are considered to be correct for any situation concerning water at $293K$, they are not by definition independent of geometry. A paper by Morgut and Nobile [36], showed that just by calibrating the source term with pressure measurement obtained from a hydrofoil and keep r_n and R_b at their default values, the constants F_e and F_c become 300 and 0.03 respectively. The other two parameters, that represent bubble radius and nucleation rate, are very difficult to obtain from experiments. Also the parameters F_e and F_c have no physical meaning, further complicating the relation between the model parameters and actual fluid properties. Even though these vapor transport models are numerically much more efficient than the barotropic models, it is almost impossible to correctly adjust and scale the model parameters without performing experiments.

2.2.5 Pros and cons

To summarize the above, there are three main options: surface tracking, compressible modeling using an equation of state or incompressible modeling using a vapor transport equation. Surface tracking is not taken into account at this point, it is clearly intended for the modeling of a small group of bubbles, not large scale cavitation structures.

The main advantage of barotropic modeling is that the relations used are based on physical properties of the liquid. If a pressure-density relation is found for water, it can easily be altered and applied to model butane or propane. However, it should be noted that if certain assumptions are made based on the fluid properties of water, these assumptions may not hold true for every fluid.

The main disadvantage of barotropic modeling is due to the compressible CFL number the time step must be chosen much smaller than for incompressible simulations, in the order of 200 times smaller. Another disadvantage of barotropic modeling is that by definition the gradients of pressure and density are aligned. The vorticity that would form when the gradients of pressure and density are not aligned, the so called baroclinic vorticity. This an important contributing factor to closing the vapor cavity. How much this will influence the final result is unclear. The work by Gopalan and Katz [37] provides more background on the influence of baroclinic vorticity in cavitation problems.

The advantage and disadvantage of the vapor transport modeling are the exact opposite of the barotropic modeling method. The time step can be chosen much larger, making the solver numerically more efficient, but the connection between the model and the physical properties of the fluid are lost. One of the goals of this project is to guarantee that the model is only dependent on physical fluid properties, no empiricism should be involved. If the same model is to be used for water, butane and propane, then the compressible solver in combination with a barotropic equation of station is the most viable option, according to these goals.

Chapter 3

Physical modeling

The purpose of this chapter is to provide an overview of the physical models used in the 1D and 2D calculations. Firstly the general outline of the CEV model as it was implemented in Tascflow is given, followed by a full derivation of the barotropic model for cavitating flows by Brennen. This model is taken as the starting point for the isenthalpic barotropic model which is validated for the fluids of interest (water, butane and propane). Secondly the chapter provides background on the equation of state used to model the non-cavitating flow and how the parameters of the model should be chosen to represent the fluid of interest.

3.1 Constant Enthalpy Vaporisation (CEV) model

In the introduction the goal of creating a barotropic model, using an isenthalpic two-phase expansion, was formulated. The motivation behind the choice for a barotropic model is given in the original documentation of the CEV-model by AEA Engineering [38], the creators of Tascflow.

The CEV model as it was implemented originally in Tascflow, was not a barotropic model. The model relied on the full solution of the Navier Stokes equations (mass, momentum and energy) to solve the cavitating flow. Figure 3-1 provides a schematic overview of the calculation method that is followed by CFX-Tascflow to update the density from a known pressure and enthalpy field. The CEV model is applied in the very last steps of an iteration to update the density based on the enthalpy of the fluid. But according to the documentation, even though the energy equation is solved by Tascflow and the fluid temperature is updated at the end of each iteration, all the fluid properties are evaluated at the (constant) free-stream temperature. It is not clear why, after the energy equation is solved, the temperature field is updated but the fluid properties are not updated. Depending on the Brennen thermal parameter (as discussed in chapter 2.1.7) the amount of cavitation can be heavily influenced by the temperature dependence of properties like density, heat capacity and of course the saturation pressure. It is concluded that the CEV model as implemented in Tascflow is only dependent on pressure, the evaluation of the temperature field is useful to visualize the cavitation zone but has no further influence on the physics taking place.

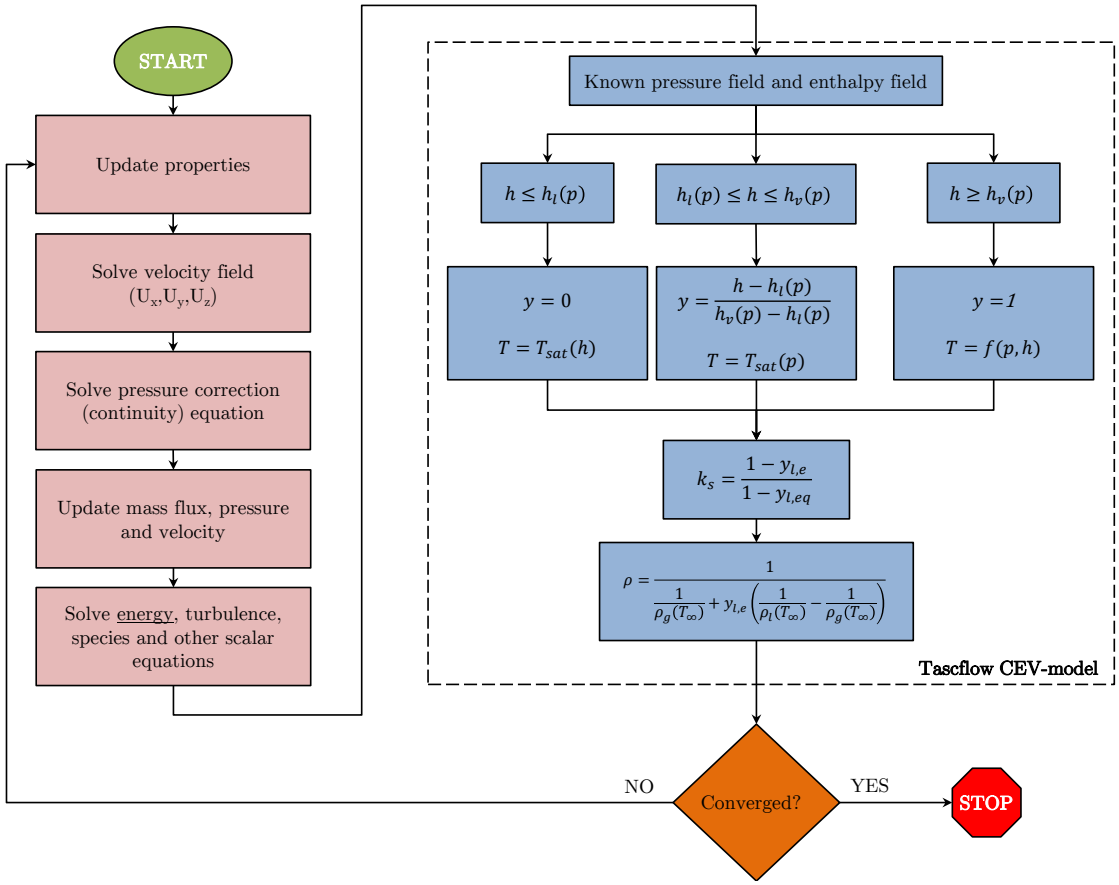

Figure 3-1: Flowchart of the CEV model calculation algorithm in Tascflow

3.2 Development of a barotropic model

To describe the isenthalpic two phase expansion of a fluid as a barotropic function, the general thermodynamic path taken during the isenthalpic expansion is reviewed, based on figure 3-2. Assuming that the fluid has a certain temperature T_∞ before and during the expansion from the free-stream condition to point 1 (figure 3-2). When the pressure is lowered further, the fluid enters the two-phase region, since p_1 is equal to $p_{sat}(T_\infty)$. In the two-phase region the enthalpy remains constant (definition), thus decreasing the pressure further will result in a decrease of temperature. From an abstract point of view, one could say that if the saturation curve is known as a function of pressure and the expansion path from point 1 to point 2 is always straight down along an isenthalpic line, it should be possible to describe the mass fraction of the two-phase mixture as a function of pressure. Referring back to chapter 3.1, the three essential fluid properties that are needed (liquid density, vapor density and saturation pressure) are always evaluated at point 1, which is equal to a known or prescribed free-stream temperature. The decision to neglect the temperature differences has to be made based on the fluid used. From chapter 2.1.7 it is known that butane and propane are much more susceptible to thermal effects than water. Knowing that propane and butane are in fact bad candidates for the free-stream temperature assumption, the influence of this assumption on the final result can be observed. The validity of the temperature assumptions is further discussed in chapter 3.2.4 and chapter 3.2.5. The energy conservation is removed from system, so that it can be replaced by a barotropic relation, directly coupling the pressure and the density of the fluid. This barotropic model will be based on Brennen's model for homogeneous bubbly flows [4].

3.2.1 Full derivation of Brennen's model for homogeneous bubbly flows

To gain a deeper understanding of the physics involved with a two-phase expansion, the barotropic model for homogeneous bubbly flows formulated by Brennen is taken as a starting point for the development of a new barotropic model. As will become clear during the derivation, the model is only partially assuming isenthalpic flow, the other part of the flow is assumed to be isentropic. This model follows the assumptions surrounding cavitation thermodynamics as described in chapter 2.1.6.

Let us consider a given mass m, occupying a volume V with corresponding density ρ. If the mass is assumed constant then the changes in volume and density are related to a pressure change dp as follows:

$$\frac{d\rho}{\rho} = -\frac{dV}{V} \Rightarrow c^2 = -\frac{V}{\rho}\frac{dp}{dV} \Rightarrow \frac{1}{\rho c^2} = -\frac{1}{V}\frac{dV}{dp} \tag{3-1}$$

A real cavitating liquid does not contain two perfectly mixed phases. A real mixture contains bubbles of a finite size, which would also mean that the thermal contact and thus the heat transfer is limited. Therefore assuming that the cavitating flow is in complete thermal equilibrium, or assuming that the cavitating flow is completely frozen (no heat transfer), is incorrect. This is also discussed in chapter 2.1.6. The original model by Brennen therefore assumes that only a part of each phase attains thermal equilibrium while the other part

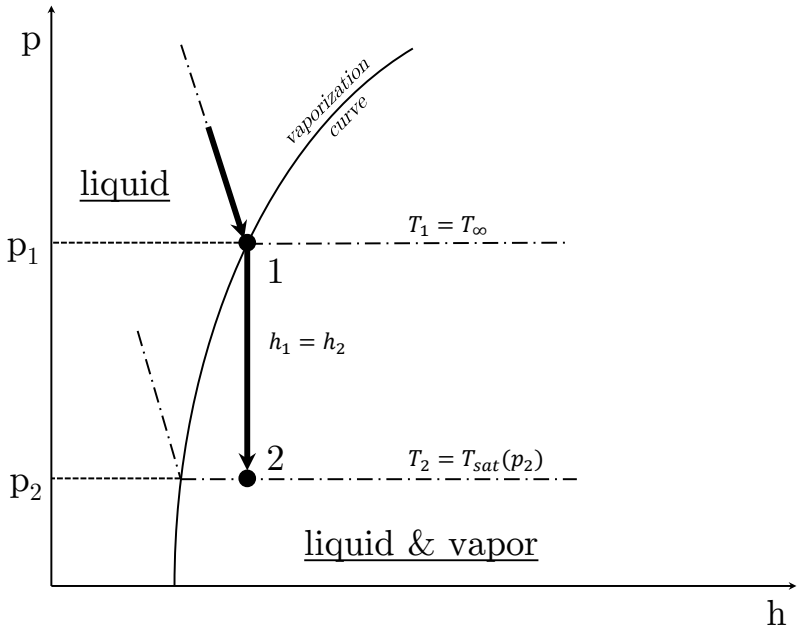

(a) $p - h$ diagram

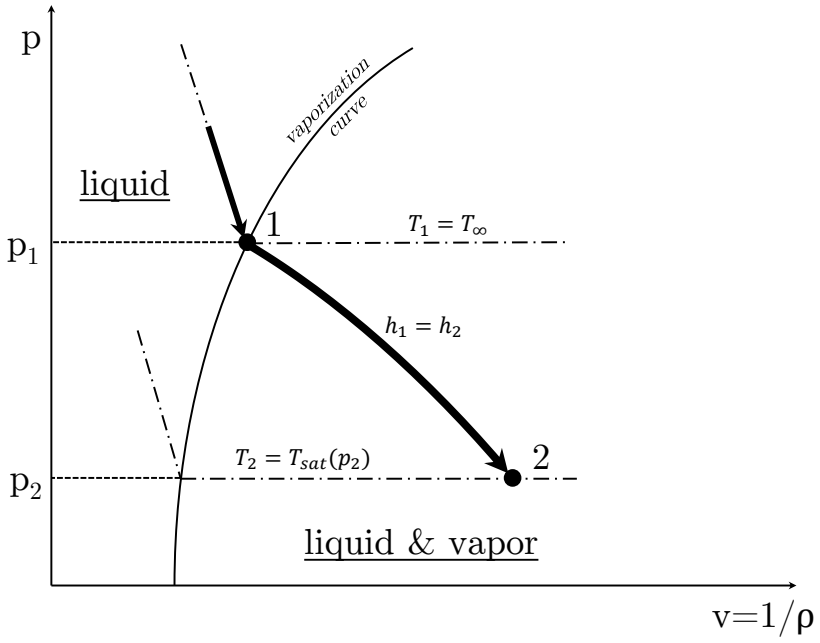

(b) $p - v$ diagram

Figure 3-2: Thermodynamical diagrams of an isenthalpic expansion

behaves as a frozen flow. A fraction $0 \leq \epsilon_v \leq 1$ of the vapor and a fraction $0 \leq \epsilon_l \leq 1$ of the liquid reach thermal equilibrium. The total volume of the fluid can be rewritten:

$$V = (1 - \epsilon_l) V_l + \epsilon_l V_l + (1 - \epsilon_v) V_v + \epsilon_v V_v \tag{3-2}$$

Differentiating the above equation, assuming that the fractions ϵ_l and ϵ_v are held constant:

$$\frac{dV}{V} = (1 - \epsilon_l) \frac{dV_l}{V} + \epsilon_l \frac{dV_l}{V} + (1 - \epsilon_v) \frac{dV_v}{V} + \epsilon_v \frac{dV_v}{V} \tag{3-3}$$

Using the definition of void fraction, being $\alpha_l = \frac{V_l}{V}$ and $\alpha_v = \frac{V_v}{V}$ the equation can be simplified to:

$$\frac{dV}{V} = (1 - \epsilon_l) \frac{dV_l}{V} + \epsilon_l \frac{dV_l}{V} + (1 - \epsilon_v) \frac{dV_v}{V} + \epsilon_v \frac{dV_v}{V} \tag{3-4}$$

The total mass of the fluid stays conserved, any increase in the mass of the vapor must come from a decrease of the mass of the liquid and vice versa. $dm_v = -dm_l$

$$\frac{dV_l}{V_l} = \frac{dm_l}{m_l} - \frac{d\rho_l}{\rho_l} \tag{3-5}$$

$$\frac{dV_v}{V_v} = \frac{dm_v}{m_v} - \frac{d\rho_v}{\rho_v} \tag{3-6}$$

For both the frozen isentropic phase and the equilibrium isenthalpic phase, barotropic relations are defined to quantify the changes in density:

$$d\rho_l = \begin{cases} \left(\frac{d\rho_l}{dp}\right)_{s_l} dp & \text{for the volume fraction } 1 - \epsilon_l \\ \left(\frac{d\rho_l}{dp}\right)_{sat} dp & \text{for the volume fraction } \epsilon_l \end{cases} \tag{3-7}$$

$$d\rho_v = \begin{cases} \left(\frac{d\rho_v}{dp}\right)_{s_v} dp & \text{for the volume fraction } 1 - \epsilon_v \\ \left(\frac{d\rho_v}{dp}\right)_{sat} dp & \text{for the volume fraction } \epsilon_v \end{cases} \tag{3-8}$$

Substituting equations 3-5 through 3-8 in equation 3-4 gives:

$$\begin{aligned} \frac{dV}{V} = & -\frac{\alpha_l}{m_l} dm_v - (1 - \epsilon_l) \frac{\alpha_l}{\rho_l} \left(\frac{d\rho_l}{dp}\right)_{s_l} dp - \epsilon_l \frac{\alpha_l}{\rho_l} \left(\frac{d\rho_l}{dp}\right)_{sat} dp \\ + & \frac{\alpha_v}{m_v} dm_v - (1 - \epsilon_v) \frac{\alpha_v}{\rho_v} \left(\frac{d\rho_v}{dp}\right)_{s_v} dp - \epsilon_v \frac{\alpha_v}{\rho_v} \left(\frac{d\rho_v}{dp}\right)_{sat} dp \end{aligned} \tag{3-9}$$

Furthermore:

$$\frac{\alpha_l}{m_l} = \frac{V_l}{V \cdot m_l} = \frac{1}{\rho_l \cdot V} \tag{3-10}$$

$$\frac{\alpha_v}{m_v} = \frac{V_v}{V \cdot m_v} = \frac{1}{\rho_v \cdot V} \tag{3-11}$$

Substituting equations 3-10 and 3-11 in equation 3-9 and using the expression for the speed of sound, $\frac{1}{\rho c^2} = -\frac{1}{V}\frac{dV}{dp}$, yields:

$$\begin{aligned}\frac{1}{\rho c^2} = {} & (1-\epsilon_l)\frac{\alpha_l}{\rho_l}\left(\frac{d\rho_l}{dp}\right)_{s_l} + \epsilon_l \frac{\alpha_l}{\rho_l}\left(\frac{d\rho_l}{dp}\right)_{sat} \\ & + (1-\epsilon_v)\frac{\alpha_v}{\rho_v}\left(\frac{d\rho_v}{dp}\right)_{s_v} + \epsilon_v \frac{\alpha_v}{\rho_v}\left(\frac{d\rho_v}{dp}\right)_{sat} + \left(\frac{1}{\rho_l} - \frac{1}{\rho_v}\right)\frac{1}{V}\frac{dm_v}{dp}\end{aligned} \tag{3-12}$$

To further expand the mass balance, the entropy balance of the phase change is considered. If it is assumed that the phase change is reversible, the entropy change of the entire fluid will be zero. This is also consistent with the claim for the isenthalpic steady approximation of the mean flow:

$$dS = d(m_l s_l + m_v s_v) = s_l dm_l + s_v dm_v + ds_l m_l + ds_v m_v = 0 \tag{3-13}$$

Where:

$$m_l = (1-\epsilon_l) V_l \rho_l + \epsilon_l V_l \rho_l \tag{3-14}$$

$$m_v = (1-\epsilon_v) V_v \rho_v + \epsilon_v V_v \rho_v \tag{3-15}$$

$$ds_l = \begin{cases} 0 & \text{for the volume fraction } 1-\epsilon_l \\ \left(\frac{ds_l}{dp}\right)_{sat} dp & \text{for the volume fraction } \epsilon_l \end{cases} \tag{3-16}$$

$$ds_v = \begin{cases} 0 & \text{for the volume fraction } 1-\epsilon_l \\ \left(\frac{ds_v}{dp}\right)_{sat} dp & \text{for the volume fraction } \epsilon_l \end{cases} \tag{3-17}$$

Again using that $dm_v = -dm_l$:

$$(s_v - s_l)\, dm_v + \epsilon_l V_l \rho_l \left(\frac{ds_l}{dp}\right)_{sat} dp + \epsilon_v V_v \rho_v \left(\frac{ds_v}{dp}\right)_{sat} dp = 0 \tag{3-18}$$

Solving for dm_v gives:

$$dm_v = -\left[\epsilon_l V_l \rho_l \left(\frac{ds_l}{dp}\right)_{sat} dp + \epsilon_v V_v \rho_v \left(\frac{ds_v}{dp}\right)_{sat} dp\right] \frac{dp}{s_v - s_l} \tag{3-19}$$

To rearrange this result further, the thermodynamic definition $dh = T \cdot ds + v \cdot dp$ is used:

$$T\left(\frac{ds_l}{dp}\right)_{sat} = \left(\frac{dh_l}{dp}\right)_{sat} - \frac{1}{\rho_l} \tag{3-20}$$

$$T\left(\frac{ds_v}{dp}\right)_{sat} = \left(\frac{dh_v}{dp}\right)_{sat} - \frac{1}{\rho_v} \tag{3-21}$$

For vaporization at constant pressure on the saturation line the definition $T(s_v - s_l) = h_v - h_l$, combined with equations 3-20 and 3-21, can be used to rearrange 3-19 into:

$$\frac{1}{V}\frac{dm_v}{dp} = \left\{\epsilon_l \alpha_l \left[1 - \rho_l \left(\frac{dh_l}{dp}\right)_{sat}\right] + \frac{\epsilon_l \alpha_l}{h_v - h_l}\left[1 - \rho_v \left(\frac{dh_v}{dp}\right)_{sat}\right]\right\} \tag{3-22}$$

Equation 3-22 is used to replace the last term in equation 3-12, which finally gives:

$$\begin{aligned}\frac{1}{\rho c^2} = {} & (1-\epsilon_l)\frac{\alpha_l}{\rho_l}\left(\frac{d\rho_l}{dp}\right)_{s_l} + \epsilon_l \frac{\alpha_l}{\rho_l}\left(\frac{d\rho_l}{dp}\right)_{sat} + (1-\epsilon_v)\frac{\alpha_v}{\rho_v}\left(\frac{d\rho_v}{dp}\right)_{s_v} + \epsilon_v \frac{\alpha_v}{\rho_v}\left(\frac{d\rho_v}{dp}\right)_{sat} \\ & + \left(\frac{1}{\rho_l} - \frac{1}{\rho_v}\right) + \left\{\epsilon_l \alpha_l \left[1 - \rho_l \left(\frac{dh_l}{dp}\right)_{sat}\right] + \epsilon_v \alpha_v \left[1 - \rho_v \left(\frac{dh_v}{dp}\right)_{sat}\right]\right\} \frac{\frac{1}{\rho_l} - \frac{1}{\rho_v}}{h_v - h_l}\end{aligned} \tag{3-23}$$

or:

$$\frac{1}{\rho c^2} = \frac{1-\alpha}{p}\left[(1-\epsilon_l) f_l + \epsilon_l g_l\right] + \frac{\alpha}{p}\left[(1-\epsilon_v) f_v + \epsilon_v g_v\right] \tag{3-24}$$

where:

$$f_V = \frac{p}{\rho_v}\left(\frac{d\rho_v}{dp}\right)_{s_v} = \frac{p}{\rho_v c_v^2} \tag{3-25}$$

$$f_L = \frac{p}{\rho_l}\left(\frac{d\rho_l}{dp}\right)_{s_l} = \frac{p}{\rho_l c_l^2} \tag{3-26}$$

$$g_V = \frac{p}{\rho_v}\left(\frac{d\rho_v}{dp}\right)_{sat} + \frac{p}{h_v - h_l}\left(\frac{1}{\rho_l} - \frac{1}{\rho_v}\right)\left[1 - \rho_v \left(\frac{dh_v}{dp}\right)_{sat}\right] \tag{3-27}$$

$$g_L = \frac{p}{\rho_l}\left(\frac{d\rho_l}{dp}\right)_{sat} + \frac{p}{h_v - h_l}\left(\frac{1}{\rho_l} - \frac{1}{\rho_v}\right)\left[1 - \rho_l \left(\frac{dh_l}{dp}\right)_{sat}\right] \tag{3-28}$$

3.2.2 Speed of sound

The final form of the barotropic relation for homogeneous bubbly flows by Brennen is given by equation 3-24. For the isenthalpic model, the model by Brennen is simplified by only taking the isenthalpic part of the model into account. As such, both ϵ_l and ϵ_v are set to 1, eliminating the terms containing f_L and f_V, and density ρ moves to the right hand side, resulting in an expression for the speed of sound c that reads:

$$\frac{1}{c^2} = \rho\left(\frac{\alpha}{p}\cdot g_V + \frac{1-\alpha}{p}\cdot g_L\right) \tag{3-29}$$

The parameters g_L and g_V in equation 3-29 are not used in the form as they are given by equations 3-28 and 3-27. The parameters are rewritten in the form of a fitting function that is only dependent on pressure. Chapter 3.4 will go into more detail concerning the function that will replace the full expressions given by equations 3-28 and 3-27. Figure 3-3 gives an example of how the speed of sound would behave in the case of isenthalpic two-phase expansion, showing the speed of sound for water, butane and propane at their respective saturation pressures for a temperature of 293K.

Comparing the isentropic case (figure 2-9) and the isenthalpic case (figure 3-3) for water, one observes that the minimum speed of sound is lower for the isenthalpic case, and no longer occurs at a 50/50 mix of liquid and vapor. This extremely low speed of sound will result in very high Mach numbers for relatively low flow velocities, which can be quite challenging to handle from a numerical standpoint as will be discussed in chapter 4. For the isenthalpic case it seems that as soon as any vapor forms, the speed of sound instantly drops to its minimum value, slowly increasing to the vapor speed of sound as the void fraction increases. According to Brennen [39] the physical behavior will be somewhere in between these extreme cases. However do note that the actual value of the minimum speed of sound remains a very difficult value to predict accurately due to the complex physics occurring at the interface.

3.2.3 Isenthalpic model

As discussed in chapter 2.2.3, by integrating the relation for the speed of sound one can obtain a barotropic model. Combining equation 2-26 and 3-29 gives:

$$\frac{\partial\rho}{\partial p} = \rho\left(\frac{\alpha}{p}\cdot g_V + \frac{1-\alpha}{p}\cdot g_L\right) \tag{3-30}$$

With g_V and g_L as per equation 3-27 and 3-28 respectively. Integrating 3-30, using the boundary condition $\rho(p_{sat}) = \rho_l$, results in:

$$\rho(p) = -\rho^*\left(tanh\left[ln\left(\frac{p}{p_{sat}}\right)^{\gamma} - arctanh\left(\frac{\rho_l}{\rho^*}\right)\right] - 1\right) \tag{3-31}$$

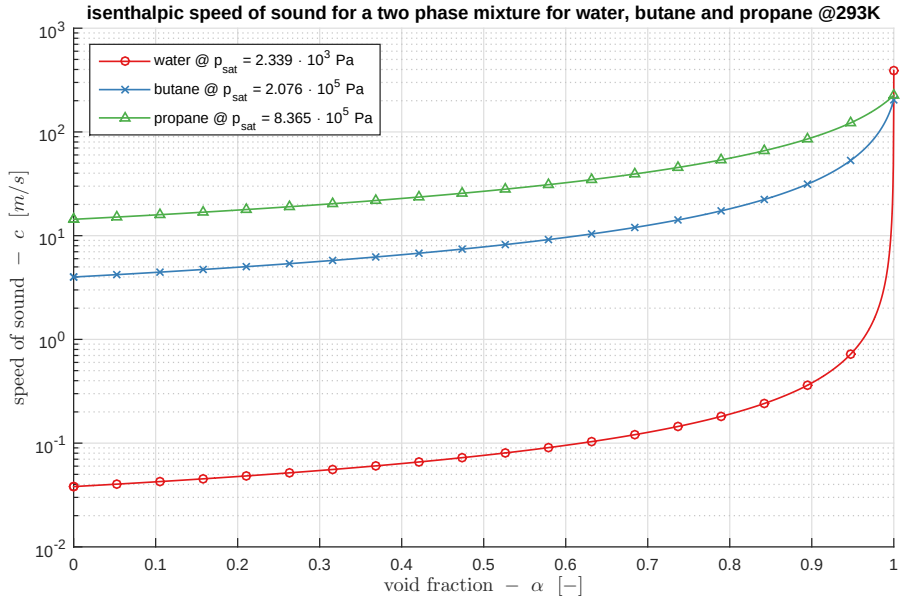

Figure 3-3: Isenthalpic speed of sound as a function of void fraction for $p = p_{sat}$ for all three fluids(water, butane and propane) at 293K

in which

$$\rho^* = \frac{g_L\rho_v - g_V\rho_l}{2\left(g_L - g_V\right)} \tag{3-32}$$

$$\gamma = \frac{g_L\rho_v - g_V\rho_l}{2\left(\rho_l - \rho_v\right)} \tag{3-33}$$

Without going into detail on how to determine the values of g_L and g_V, as will be discussed in chapter 3.4, it will be often the case that $g_V/g_L << 1$ and that $\rho_v << \rho_l$. Equation 3-31 can then be replaced by an asymptotic approximation:

$$\rho \sim \frac{-\rho_v}{e^{-\frac{\rho_v}{\rho_l}\left[1+g_L\cdot ln\left(\frac{p_{sat}}{p}\right)\right]} - 1} \tag{3-34}$$

as $g_V/g_L \to 0$ and $\rho_v/\rho_l \to 0$

In a later chapter (chapter 3.4) the exact determination of the values of g_L and g_V is given, also showing that neglecting g_V can be allowed. For cases where $g_L \cdot ln\left(\frac{p_{sat}}{p}\right) >> 1$, equation 3-34 can be further reduced to:

$$\rho \sim \frac{-\rho_v}{\left(\frac{p_{sat}}{p}\right)^{\left[-g_L\cdot\frac{\rho_v}{\rho_l}\right]} - 1} \tag{3-35}$$

It is important to note that the previous condition $g_L \cdot ln\left(\frac{p_{sat}}{p}\right) >> 1$ does not hold per se, limiting the situations in which this very simple expression can be applied. It only holds for fluids that are not significantly affected by the thermal effects of cavitation, i.e. the Brennen thermal parameter Σ should be relatively small for that fluid at the temperature of interest.

To demonstrate the effects of the simplifications made, equation 3-31, 3-34 and 3-35 are applied to water and propane and compared with data from Fluidprop [5] that provides the exact density of each fluid (ρ_{FP}). The Tait equation of state [40], which will be discussed in chapter 3.3, is used to model the saturated liquid phase of each fluid for $p > p_{sat}$. The results of this comparison are shown in figures 3-4 and 3-5. Note that water and propane are evaluated at $293K$ and that the temperature plays an important role. If the fluids are evaluated at a different temperature, both p_{sat} and g_L change, influencing whether $g_L \cdot ln\left(\frac{p_{sat}}{p}\right) >> 1$ is a valid assumption or not.

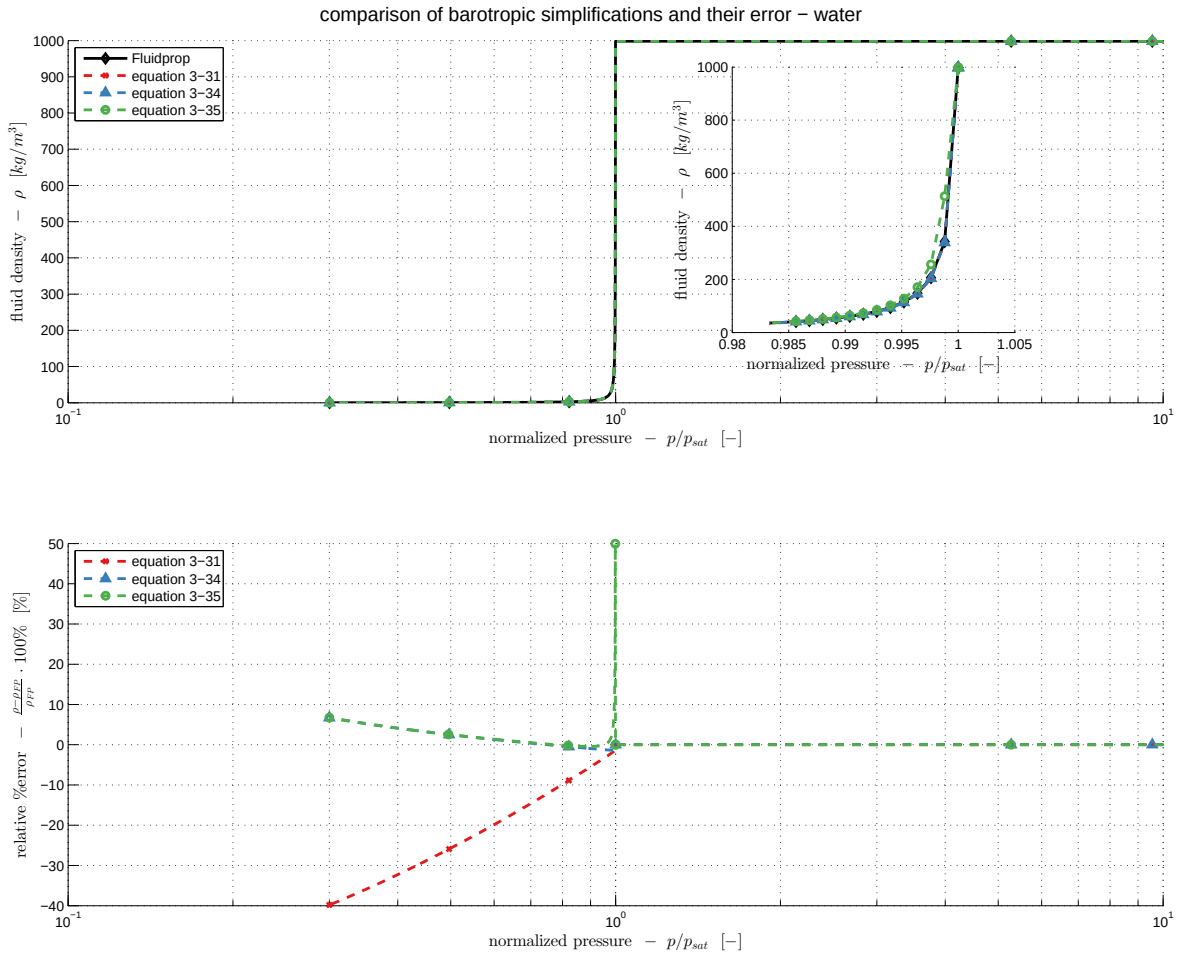

Figure 3-4: comparison of the simplified barotropic relations for water; density and relative error percentage as function of pressure

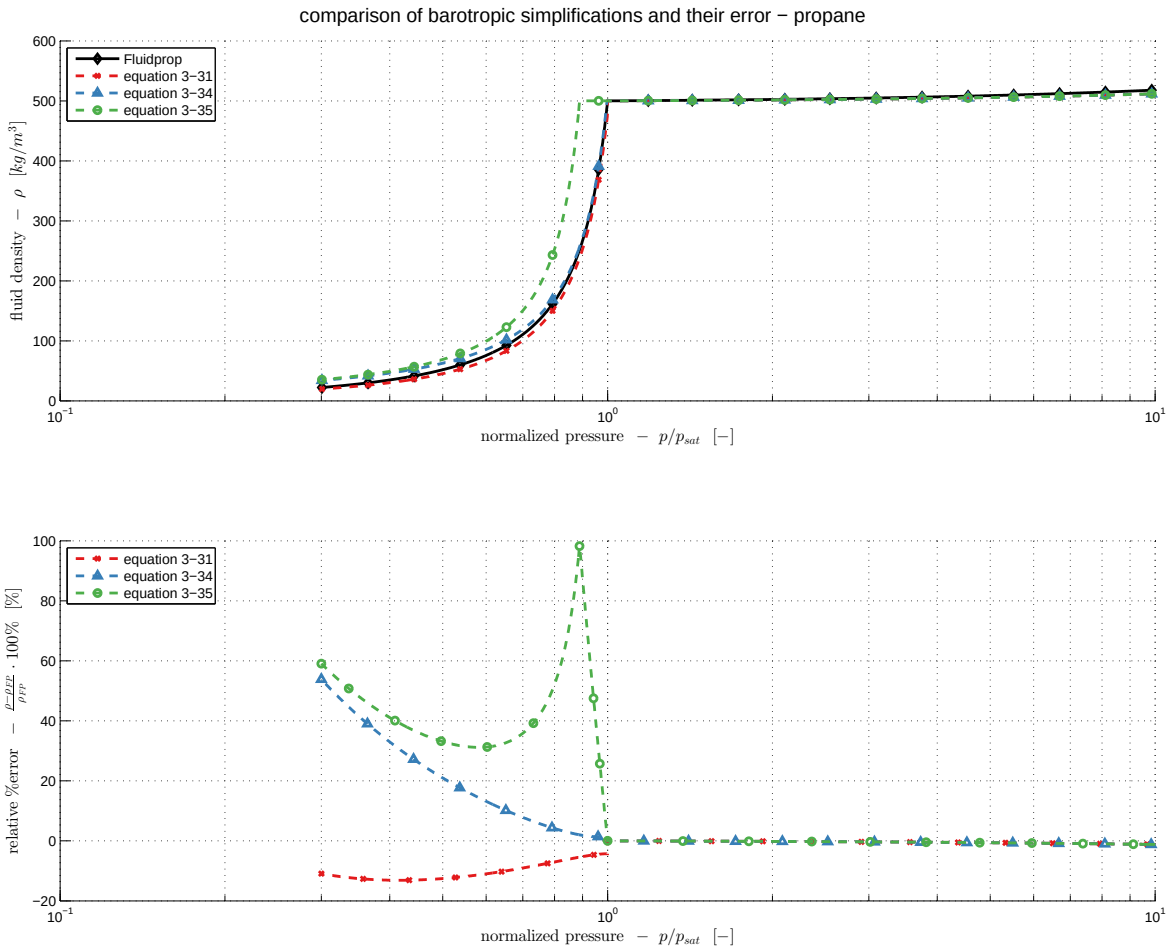

Figure 3-5: comparison of the simplified barotropic relations for propane; density and relative error percentage as function of pressure

From figure 3-4 it can be seen that equation 3-31, 3-34 and 3-35 all perform satisfactory in describing the isenthalpic expansion of water. Even equation 3-35 results in an almost identical approximation compared to the more complicated equation 3-31. The large spike that is seen for the relative and absolute error of equation 3-35, just left of p_{sat}, is due to a very small shift in pressure. Since 90% of the density of water is lost in the first 10 to 15 Pascals of pressure reduction, the small shift leads to a large mismatch between equation 3-35 and the data from Fluidprop. But if the small shift in pressure can be allowed, equation 3-35 is an excellent substitute for the full expression given by equation 3-31. It is also interesting to note that equation 3-34 gives an overall better approximation of the density than the other two equations, which is surprising because g_V (Brennen vapor index) is omitted in equation 3-34, thus neglecting the thermodynamic influence of the vapor. This however does not mean that equation 3-31 is replaced in the final implementation of the model, the full expression (equation 3-31) is still required to accurately model the barotropic behavior of butane and propane. Figure 3-5 shows why equation 3-35 cannot be applied in every situation. To avoid overshoot of the density per equation 3-35, the solution shown in figure 3-5 is cut off at the saturated liquid density between p_{sat} and $0.88 \cdot p_{sat}$. For pressures below $0.88 \cdot p_{sat}$ there is no overshoot but the relative error is found to be larger than 30% across the entire range ($p/p_{sat} < 0.88$). Hence, for propane (at $293K$) equation 3-35 cannot be used to model (by approximation) the isenthalpic expansion.

3.2.4 Validation of CEV-model with Fluidprop

The final step in the development of the barotropic model is the validation of the barotropic relation when compared to an isenthalpic expansion path obtained from a thermodynamic library. Figure 3-6 shows the results of this validation. Three solid lines indicate the isenthalpic expansion paths that are obtained from the Fluidprop software [5], starting at their respective saturation pressures, going down to 30% of that saturation pressure. The dashed lines with the cross-shaped markers indicate the results obtained from the model using the free-stream temperature assumption. The density along the y-axis is normalized by the saturated liquid density of the respective fluid. The general results of the model are more than satisfactory. The model and validation lines for water are indistinguishable, guaranteeing that water is accurately modeled for this purpose. The model and validation lines for butane and propane are very similar in shape but the density tends to be underestimated by a small amount. The cause for this deviation is likely due to inaccuracies in the curve fitting of g_L as will be described in chapter 3.4, or due to the free-stream temperature assumption as discussed in chapter 3.2.

3.2.5 Free-stream temperature assumption

It is well possible that the small mismatch discussed in the previous paragraph is caused due to differences in thermal behavior. As stated before, butane and propane are much more susceptible to the local thermal effects of cavitation. To check if this is causing the deviation the theoretical temperature drop accompanying the pressure drop is looked up in thermodynamical library of the respective fluid. The result is shown in figure 3-7, all three liquid start at the assumed free-stream temperature of 293K and start to cool down as the pressure is lowered to 30% of their respective saturation pressures. At the lowest pressures

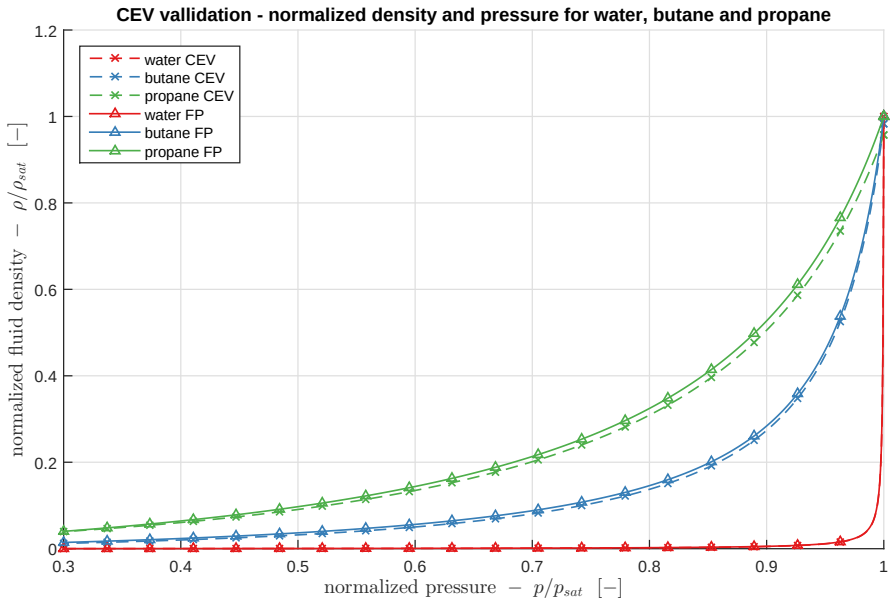

Figure 3-6: Density as a function of pressure comparing the CEV-model (equation 3-31) with Fluidprop [5] for all three fluids(water, butane and propane)

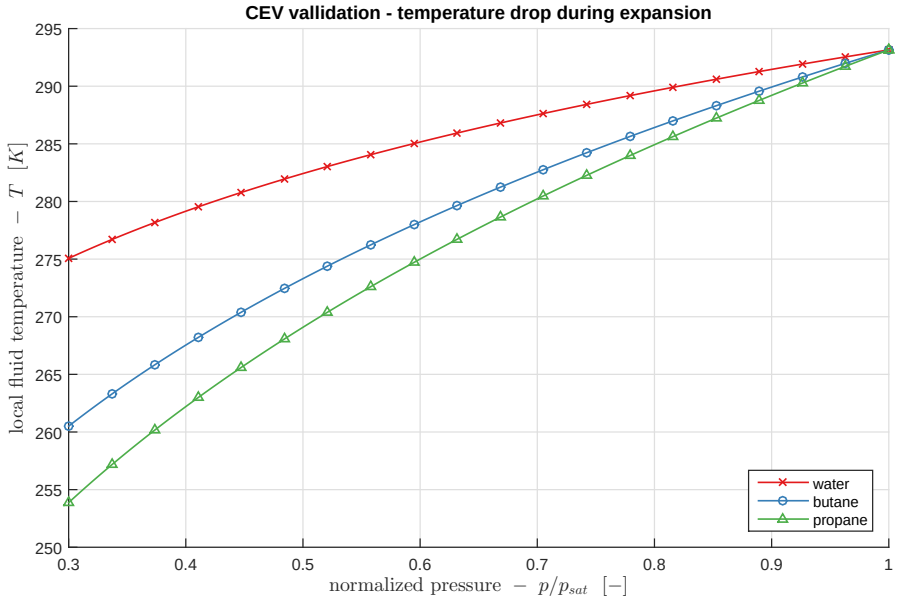

Figure 3-7: Temperature as a function of pressure showing the effect of an isenthalpic expansion

the temperatures of fluids are lowered anywhere from 18K to 39K, more than enough to check if the fluid properties significantly influence the result obtained from the barotropic model (equation 3-31). To that end the barotropic model is run again, but the fluid properties are adjusted for the temperature that corresponds with the current pressure according to figure 3-7. Figure 3-8 contains a second set of dashed lines with the circle-shaped markers to indicate the results obtained from the model using the temperature corrected fluid properties.

From the foregoing exercise two things are concluded. Firstly, the inaccuracy of the model is likely caused due to inaccurate fitting of g_L which can easily grow an order of magnitude in a relatively small pressure range, influencing the results obtained from the model. Secondly, the influence of temperature changes on the properties of the fluid is very limited, figure 3-8 clearly shows that the difference between temperature correction and free-stream assumptions is minimal. The temperature can be considered as a second-order effect, and is not taken into account for the current model.

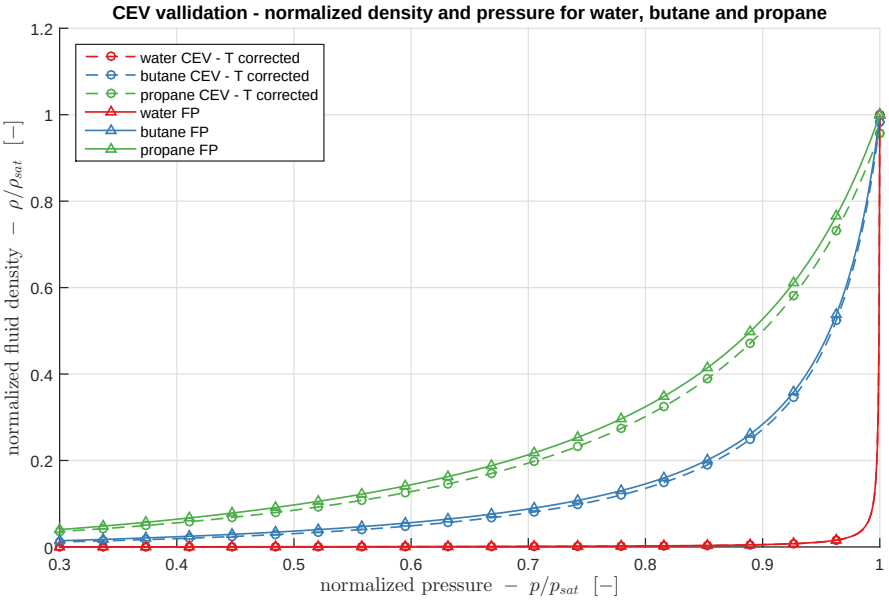

Figure 3-8: Density as a function of pressure comparing the CEV-model (equation 3-31) with Refprop for all three fluids(water, butane and propane), fluid properties are corrected for temperature drop

3.3 Completing the equation of state

The fluid is modeled for the scenario where p will be lower than p_{sat} assuming an isenthalpic expansion to lower densities. In the non cavitating fluid where p is equal to p_{sat} or higher, an equation of state is needed to model the (weakly) compressible liquid. The Tait equation of state is chosen for this purpose. In the work by Dymond and Malholtra [6] an excellent overview of the Tait equation of state is presented, describing the origin of the equation, several different forms and the recent developments on estimation of the coefficients for

complex multi-component mixtures. The original form of the Tait equation of state, used to fit isothermal density data for elevated pressures, is given by the following expression [40]:

$$\frac{\rho - \rho_0}{\rho} = C \cdot log\left(\frac{B + p}{B + p_0}\right) \tag{3-36}$$

3.3.1 Tait equation of state

The equation of state that is used in this work is the equation "attributed" to Tait, which reads (Koop [26]):

$$p = K_0 \left[\left(\frac{\rho}{\rho_l}\right)^N - 1\right] + p_{sat} \tag{3-37}$$

Although it is often referred to as the 'Tait' equation of state, multiple authors (Koop [26], Dymond and Malholtra [6]) voice the fact that this is actually not correct but that due to a misquotation of earlier work this is in fact the Tammann equation of state [41]. For the purpose of clarity equation 3-37 will also in this work be referred to as the Tait equation of state. Besides the two coefficients K_0 and N, which will need to be derived using a curve fitting procedure, the equation needs a reference state: i.e. a reference pressure, p_0, and a reference density, ρ_0. The reference pressure is chosen to be equal to the saturation pressure, p_{sat}, and the reference density is chosen equal to the liquid saturation density, ρ_l. Note that in theory both the reference quantities are a function of temperature, but since it is decided in chapter 3.2.5 that the problem is considered isothermal, this is of no concern.

3.3.2 Speed of sound

For barotropic relations the speed of sound can be easily obtained by taking the first derivative of the pressure with respect to the density, as seen in chapter 2.2.3, equation 2-26:

$$\frac{1}{c^2} = \frac{\partial p}{\partial \rho} \tag{3-38}$$

Applying this to the Tait equation of state (equation 3-37) gives for the speed of sound:

$$c = \sqrt{\frac{N K_0 \left(\frac{\rho}{\rho_l}\right)^{N-1}}{\rho_l}} \tag{3-39}$$

3.4 Parameter fitting

The strength of the barotropic models is that they can be fitted to any fluid if thermodynamic data of the fluid is present. The three fluids of interest for this thesis: water, butane and

propane have sufficient available data and measurements to accurately fit the fluid to the corresponding models. For $p < p_{sat}$ the models are fitted to the isenthalpic barotropic relation as described in chapter 3.2.3, for $p \geq p_{sat}$ the models are fitted to the Tait equation of state as described in chapter 3.3.1.

3.4.1 Tait equation of state: K_0 and N

A point of attention for barotropic relations is the fact that when fitting fluid data from a database (Refprop), fitting only the density to the pressure is not sufficient. The Tait equation of state for liquids, as treated in chapter 3.3.1, is an example of this problem. For the Tait equation the speed of sound is given by equation 3-39, this equation still contains K_0 and N. Depending on the starting point, a curve fitting algorithm can produce different sets of constants that fit the pressure-density relation with the same accuracy. Also in literature many different sets for K_0 and N are used by different authors (which are often only interested in the pressure-density relation). But when these sets of constants are evaluated for equation 3-39, the resulting speed of sound is not even close to the value provided by a thermodynamic database.

To remedy this discrepancy, the constants K_0 and N are determined by simultaneously fitting the pressure and the speed of sound with the density of the liquid. The algorithm performs a large number of curve fits, based on a wide range of starting points. At the end each curve fit (consisting of i points) is evaluated to obtain P^{fit} and c^{fit} and is then compared with data from the thermodynamic database, represented by P^{lib} and c^{lib}. The set of constants that is selected is the set that resulted in the lowest value of the object function defined by equation 3-40.

$$objfun = \left| \sum_{i=1}^{n} \left[p_i^{fit} - p_i^{lib} \right] \right| + \left| \sum_{i=1}^{n} \left[c_i^{fit} - c_i^{lib} \right] \right| \tag{3-40}$$

This procedure is performed for the three fluids of interest: water, butane and propane at $293K$. The resulting values of K_0 and N are presented in table 3-1 and are used for each calculation in this thesis, unless stated otherwise. An example can be found in figures 3-4 and 3-5, which use the values from table 3-1 to model the density of the saturated liquid phase of each fluid. In these figures it can also be seen that the error in calculated liquid density is close to zero for the entire range where $p > p_{sat}$.

Table 3-1: Tait equation of state constants for water, butane and propane

	K_0 [Pa]	N [-]
water	$3.6904 \cdot 10^8$	5.9496
butane	$4.7779 \cdot 10^7$	10.4209
propane	$2.5835 \cdot 10^7$	10.9740

3.4.2 CEV equation of state: g_L and g_V

The isenthalpic liquid and vapor indexes, as shown by equation 3-28 and 3-27, are too complex to directly implement into the code. The solid lines in figure 3-9 show the liquid index of water, butane and propane as a function of reduced pressure. The solid lines in figure 3-10 show the vapor index of water, butane and propane as a function of reduced pressure. The derivatives that are found in equation 3-28 and 3-27 are numerically approached by a central difference scheme, for instance for $\left(\frac{d\rho_l}{dp}\right)_{sat}$:

$$\left(\frac{d\rho_l}{dp}\right)_{sat} = \frac{\rho_{l,sat}\left(p+\Delta p\right)-\rho_{l,sat}\left(p-\Delta p\right)}{2\cdot\Delta p} \tag{3-41}$$

Brennen [4] suggested that it is possible to replace the full expression of liquid index g_L with a curve fit that makes the liquid index a function of reduced pressure, p_{red}. The reduced pressure is defined as the pressure divided by the critical pressure of the fluid $\left(p_{red}=\frac{p}{p_{crit}}\right)$. The function that relates the liquid index to the reduced pressure has the form of a second order polynomial on double logarithmic axes (Brennen [4]):

$$g_L = e^{\left[a\cdot log^2\left(\frac{p}{p_c}\right)+b\cdot log\left(\frac{p}{p_c}\right)+c\right]} \tag{3-42}$$

The dashed lines in figure 3-9 represent the fits that were found for water, butane and propane. The three coefficients a, b and c of the second order polynomial for each fluid, that resulted in a satisfactory fit, are shown in table 3-2.

The vapor index g_V is not being fitted to a curve. For relatively low reduced pressures $(p_{red} < 1\cdot 10^{-2})$ the liquid index is at least two orders of magnitude larger than the vapor index, thus dominating the solution. Therefore the average value of the vapor index over the entire pressure range is taken for g_V. The dashed lines in figure 3-10 represent the averages that were found for water, butane and propane. The values of the averages for g_V are listed in the last column of table 3-2.

Table 3-2: Isenthalpic liquid and vapor index constants for water, butane and propane

	g_L (equation 3-42)			g_V
	a	b	c	
water	0.01262	-0.6014	0.8241	0.887
butane	0.01726	-0.5168	1.4654	0.9424
propane	0.01747	-0.5136	1.2094	0.9084

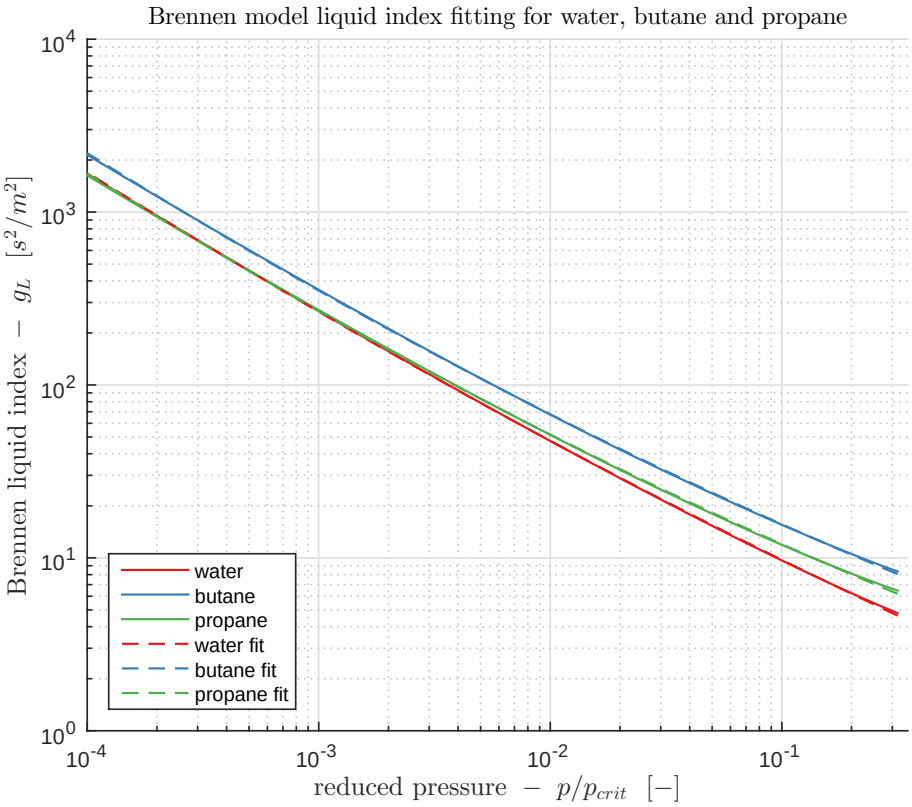

Figure 3-9: Brennen liquid index, g_L, as a function of reduced pressure comparing the library data (solid) with the fitted data (dashed) for all three fluids(water, butane and propane)

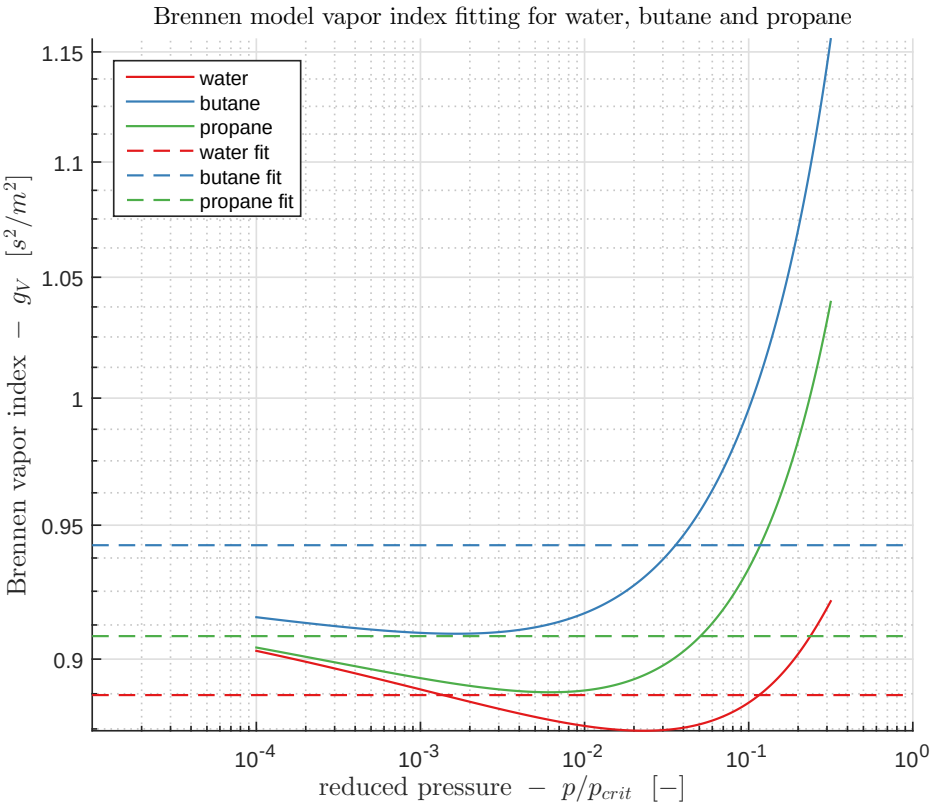

Figure 3-10: Brennen vapor index, g_V, as a function of reduced pressure comparing the library data (solid) with the fitted data (dashed) for all three fluids(water, butane and propane)

Chapter 4

Numerical modeling

The purpose of this chapter is to provide an overview of the numerical methods used in the 1D and 2D calculations. Firstly the general outline of the Finite Volume Method is given, including the MUSCL[1] center to face extrapolation method, Barth-Jespersen [43] and Venkatakrishnan [44] limiters and the AUSM-HLLC hybrid flux calculation algorithm. Secondly the chapter provides background on the implementation of the 1D and 2D calculations (in Matlab and OpenFOAM respectively) including matters such as boundary conditions and turbulence models.

4.1 Finite volume method and the Euler-equations

Before focusing on the solution of the Euler-equations, a more general transport equation is taken as an example to work out the principles of the finite volume method. The general 1D transport equation has the following form, with state vector Q and flux vector F, where $Q = Q(x,t)$ and $F = F(x,t)$:

$$\frac{\partial Q}{\partial t} + \frac{\partial F}{\partial x} = 0 \tag{4-1}$$

Defining that the grid is spaced in such a way that the center of the cell is denoted with index i and the two faces (or endpoints) are denoted by $i + \frac{1}{2}$ and $i - \frac{1}{2}$. This means that the length of the cell is equal to $\Delta x = x_{i+\frac{1}{2}} - x_{i-\frac{1}{2}}$. Also see figure 4-1 for a graphical representation of the grid.

The evaluation of a conserved quantity q can be formulated by the following integral, in which general autonomous flux $f(q)$ only depends on q, according to Leveque [45]:

[1] The Monotonic Upstream-Centered Scheme for Conservation Laws developed by van Leer [42] is a high-accuracy numerical scheme that can give stable solutions with the help of limiters, even if the system encounters shocks or discontinuities.

$$\frac{d}{dt}\int_{x_{i-\frac{1}{2}}}^{x_{i+\frac{1}{2}}} q(x,t)dx \quad = \quad f(q(x_{i-\frac{1}{2}},t)) - f(q(x_{i+\frac{1}{2}},t)) \tag{4-2}$$

This integral is then evolved in time, meaning that time is advanced by a known quantity $\Delta t = t_{n+1} - t_n$. The integral is also dived by Δx, resulting in the expression:

$$\begin{aligned} &\frac{1}{\Delta x}\int_{x_{i-\frac{1}{2}}}^{x_{i+\frac{1}{2}}} q(x,t_{n+1})dx - \frac{1}{\Delta x}\int_{x_{i-\frac{1}{2}}}^{x_{i+\frac{1}{2}}} q(x,t_n)dx = \\ &\frac{1}{\Delta x}[\int_{t_n}^{t_{n+1}} f(q(x_{i-\frac{1}{2}},t))dt - \int_{t_n}^{t_{n+1}} f(q(x_{i+\frac{1}{2}},t))dt] \end{aligned} \tag{4-3}$$

The division of the entire integral by Δx has been done for the reason that it is now possible to define a value Q that is the average of a property in a certain cell i at time t_n. A similar assumption can be made for the flux that passes through a surface at $x_{i+\frac{1}{2}}$ between time t_n and t_{n+1}

$$Q_i^n \quad \approx \quad \frac{1}{\Delta x}\int_{x_{i-\frac{1}{2}}}^{x_{i+\frac{1}{2}}} q(x,t_n)dx \equiv \frac{1}{\Delta x}\int_{C_i} q(x,t_n) \tag{4-4}$$

$$F_{i+\frac{1}{2}}^n \quad \approx \quad \frac{1}{\Delta t}\int_{t_n}^{t_{n+1}} f(q(x_{i+\frac{1}{2}},t_n)dt \tag{4-5}$$

The previous expressions (equations 4-4 and 4-5) can be used to drastically simplify the problem and to obtain a solvable discrete expression for the time evolution of a conserved quantity Q.

$$Q_i^{n+1} \quad = \quad Q_i^n - \frac{\Delta t}{\Delta x}\left(F_{i+\frac{1}{2}}^n - F_{i-\frac{1}{2}}^n\right) \tag{4-6}$$

Note that the flux $F_{i\pm\frac{1}{2}}^n$ is only an approximation and not equivalent to the solution of an exact integral. Although it would be reasonable to calculate the flux through the left wall of cell i ($F_{i-\frac{1}{2}}^n$) by using the value of cell i and its left hand neighbour cell $i-1$, it has the disadvantage that it is a first order approximation. Due to the large density ratios and discontinuities found in cavitation, it is a reasonable assumption that a higher order scheme will net better results than a first order scheme. The higher order scheme is based on MUSCL-interpolation and uses slope limiters to guarantee a stable and monotonous solution. The details of the higher order method and the flux calculations are discussed in the coming paragraphs.

To further increase the stability of the scheme the explicit forward Euler time stepping is replaced by a four step explicit Runge Kutta scheme. The advantage of this scheme is that it will provide fourth order accuracy in time but is still a very simple explicit method to implement into the code. Each of the four steps are written out in equations 4-7 through 4-10.

$$Q^{(1)} = Q^{(n)} + \frac{1}{2}\frac{\Delta t}{\Delta x}\left(F^{(n)}_{i+\frac{1}{2}} - F^{(n)}_{i-\frac{1}{2}}\right) \tag{4-7}$$

$$Q^{(2)} = Q^{(1)} + \frac{1}{2}\frac{\Delta t}{\Delta x}\left(F^{(1)}_{i+\frac{1}{2}} - F^{(1)}_{i-\frac{1}{2}}\right) \tag{4-8}$$

$$Q^{(3)} = \frac{2}{3}Q^{(n)} + \frac{1}{3}Q^{(2)} + \frac{1}{6}\frac{\Delta t}{\Delta x}\left(F^{(2)}_{i+\frac{1}{2}} - F^{(2)}_{i-\frac{1}{2}}\right) \tag{4-9}$$

$$Q^{(n+1)} = Q^{(3)} + \frac{1}{2}\frac{\Delta t}{\Delta x}\left(F^{(3)}_{i+\frac{1}{2}} - F^{(3)}_{i-\frac{1}{2}}\right) \tag{4-10}$$

The maximum allowed time step is calculated using the Courant-Friedrichs-Lewy (CFL) condition. Note that in equation 4-12 the speed of sound is included when calculating the CFL number. For incompressible flow solutions the CFL number is defined as the number of cells that are passed by a fluid element in a single time step; i.e.:

$$CFL = \frac{(u)\,\Delta t}{\Delta x} \tag{4-11}$$

For compressible flows the CFL number is defined as the number of cells that are passed by a pressure perturbation that is traveling trough the domain. This perturbation is traveling at the wave velocity which is the convecting velocity of the fluid plus the speed of sound. For this project a compressible solver is used, and the CFL number reads:

$$CFL = \frac{(u+c)\,\Delta t}{\Delta x} \tag{4-12}$$

Instead of applying the finite volume method to a general transport equation, it is applied to set of conservation equations know as the 1D Euler equations. This set governs the mass, momentum and energy balance of a 1D adiabatic inviscid flow field. Note that each conservation equation contains a time derivative and a convective term of certain conserved quantity (ρ, ρU or ρE). Thus it is possible to use the previously described methods to obtain a solution for the 1D Euler equations. The governing equations are:

$$\frac{\partial \rho}{\partial t} + \frac{\partial \rho u}{\partial x} = -\frac{\rho u}{A(x)}\frac{dA}{dx} \tag{4-13}$$

$$\frac{\partial \rho u}{\partial t} + \frac{\partial (\rho u^2 + P)}{\partial x} = -\frac{\rho u^2}{A(x)}\frac{dA}{dx} \tag{4-14}$$

$$\frac{\partial \rho E}{\partial t} + \frac{\partial (\rho E + P)u}{\partial x} = -\frac{\rho u E + Pu}{A(x)}\frac{dA}{dx} \tag{4-15}$$

The right hand side of the Euler equations should normally be equal to zero for conservation, but in the set described by equations 4-13 to 4-15, source terms have been added that can model variable cross-sectional area along a single dimension. One of the steps in the validation

process will be describing cavitating flow inside a Venturi-like nozzle in which these source terms will play a very important role. These source terms are not necessary to describe the flow field, but provide the possibility to describe the varying geometry of the nozzle along a single axis, keeping the simulation one-dimensional.

For the purpose of this thesis the cavitation will be modeled by a barotropic equation of state. As discussed in the previous chapter this implies that the cavitation occurs at constant temperature. By definition the density of a barotropic fluid is a function of pressure alone. The energy conversation equation (4-15) is replaced by a constitutive relation that connects pressure with density. The newly closed system becomes:

$$\frac{\partial \rho}{\partial t} + \frac{\partial \rho u}{\partial x} = -\frac{\rho u}{A(x)}\frac{dA}{dX} \tag{4-16}$$

$$\frac{\partial \rho u}{\partial t} + \frac{\partial (\rho u^2 + P)}{\partial x} = -\frac{\rho u^2}{A(x)}\frac{dA}{dX} \tag{4-17}$$

$$\rho = f(p) \tag{4-18}$$

4.1.1 MUSCL face extrapolation scheme

The Monotone Upwind Schemes for Scalar Conservation Laws, or MUSCL-schemes are collections of interpolation schemes that are used to estimate the values of a certain property at the face of a cell, based on the values that are saved in the center of the cell. The MUSCL-schemes show improved performance when handling, discontinuities , shocks and large density gradients. All of which are to be expected when modeling cavitation. The main improvement is in the fact that the flux through the face is no longer calculated by the taking value in the center of the cell but by extrapolating the value of the cell to the faces. The center values of each cell are extrapolated to the left and right face of the respective cell. The flux calculation can now be performed by taking the values directly at the face, extrapolated from the left and right neighbour. Figure 4-1 gives a graphical representation of the MUSCL-scheme.

The values are extrapolated to the faces by using the central difference to estimate the gradient. The resulting value for the left and right faces of cell i are:

$$q^L_{i-\frac{1}{2}} = q_{i-1} + \frac{1}{2}\cdot\frac{q_i - u_{i-2}}{2\Delta x}\cdot\Delta x \tag{4-19}$$

$$q^R_{i-\frac{1}{2}} = q_i - \frac{1}{2}\cdot\frac{q_{i+1} - u_{i-1}}{2\Delta x}\cdot\Delta x \tag{4-20}$$

$$q^L_{i+\frac{1}{2}} = q_i + \frac{1}{2}\cdot\frac{q_{i+1} - u_{i-1}}{2\Delta x}\cdot\Delta x \tag{4-21}$$

$$q^R_{i+\frac{1}{2}} = q_{i+1} - \frac{1}{2}\cdot\frac{q_{i+2} - u_i}{2\Delta x}\cdot\Delta x \tag{4-22}$$

$$q_{i+\frac{1}{2}} = \left[q^L_{i+\frac{1}{2}}, q^R_{i+\frac{1}{2}}\right] \tag{4-23}$$

$$q_{i-\frac{1}{2}} = \left[q^L_{i-\frac{1}{2}}, q^R_{i-\frac{1}{2}}\right] \tag{4-24}$$

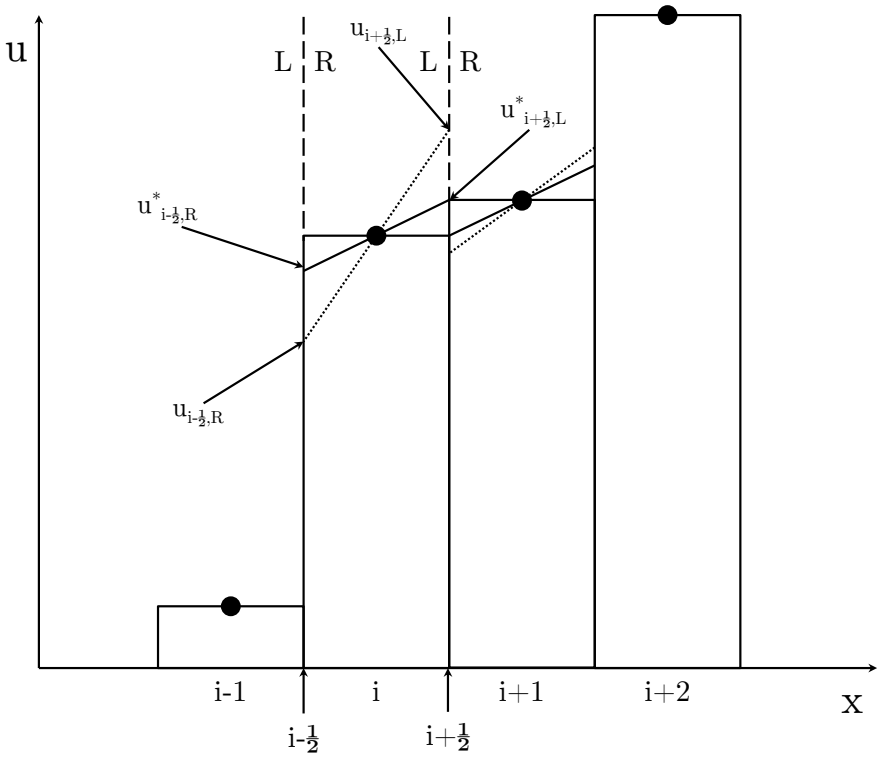

Figure 4-1: Sketch of the MUSCL method (with and without limiters)

If the face extrapolations are used directly as described by equations 4-19 through 4-24, the result would be equal to the dashed lines in figure 4-1. These results however are not monotonic and will lead to numerical instabilities (oscillations).

4.1.2 Slope limiters

The second part of the MUSCL scheme is to implement slope limiters that will ensure that values at the faces are monotonous with respect to the values in the center of the cell. Equations 4-19 through 4-24 are rewritten to include a factor ϕ that will correct the slope that was originally calculated with the central differences:

$$q^{L*}_{i-\frac{1}{2}} = q_{i-1} + \frac{1}{4} \cdot \phi^{R}_{i-\frac{1}{2}} \cdot (q_i - q_{i-2}) \tag{4-25}$$

$$q^{R*}_{i-\frac{1}{2}} = q_i - \frac{1}{4} \cdot \phi^{L}_{i-\frac{1}{2}} \cdot (q_{i+1} - q_{i-1}) \tag{4-26}$$

$$q^{L*}_{i+\frac{1}{2}} = q_i + \frac{1}{4} \cdot \phi^{R}_{i+\frac{1}{2}} \cdot (q_{i+1} - q_{i-1}) \tag{4-27}$$

$$q^{R*}_{i+\frac{1}{2}} = q_{i+1} - \frac{1}{4} \cdot \phi^{L}_{i+\frac{1}{2}} \cdot (q_{i+2} - q_i) \tag{4-28}$$

$$q^{*}_{i+\frac{1}{2}} = \left[q^{L*}_{i+\frac{1}{2}}, q^{R*}_{i+\frac{1}{2}} \right] \tag{4-29}$$

$$q^{*}_{i-\frac{1}{2}} = \left[q^{L*}_{i-\frac{1}{2}}, q^{R*}_{i-\frac{1}{2}} \right] \tag{4-30}$$

In figure 4-1, the graphical representation of the MUSCL scheme, the slope limited face extrapolations are equal to the solid lines. Note that the face extrapolated values are monotonic, eliminating the problem of spurious oscillations. The flux $F^{n}_{i\pm\frac{1}{2}}$ will be evaluated using the value $q^{*}_{i\pm\frac{1}{2}}$. Paragraphs 4.1.3 and 4.1.4 will provide details on two slope limiters used in this work: the Barth-Jespersen limiter [43] and the Venkatakrishnan limiter [44].

4.1.3 Barth-Jespersen limiter

The role of a limiter is to provide a factor ϕ for each extrapolation in such a way that the monotonicity for the entire domain is guaranteed. The slope limiter by Barth and Jespersen is defined as [43]:

$$q_i^{max} = max\left(q_{i-1}, q_i, q_{i+1}\right) \tag{4-31}$$

$$q_i^{min} = min\left(q_{i-1}, q_i, q_{i+1}\right) \tag{4-32}$$

$$r_{i-\frac{1}{2}}^{L} = \begin{cases} \frac{q_i^{max}-q_i}{q_{i-\frac{1}{2}}^{L}-q_i} & \text{if } q_{i-\frac{1}{2}}^{L} - q_i > 0 \\ \frac{q_i^{min}-q_i}{q_{i-\frac{1}{2}}^{L}-q_i} & \text{if } q_{i-\frac{1}{2}}^{L} - q_i < 0 \\ 1 & \text{if } q_{i-\frac{1}{2}}^{L} - q_i = 0 \end{cases} \tag{4-33}$$

$$r_{i+\frac{1}{2}}^{R} = \begin{cases} \frac{q_i^{max}-q_i}{q_{i+\frac{1}{2}}^{R}-q_i} & \text{if } q_{i+\frac{1}{2}}^{R} - q_i > 0 \\ \frac{q_i^{min}-q_i}{q_{i+\frac{1}{2}}^{R}-q_i} & \text{if } q_{i+\frac{1}{2}}^{R} - q_i < 0 \\ 1 & \text{if } q_{i-\frac{1}{2}}^{R} - q_i = 0 \end{cases} \tag{4-34}$$

$$\phi_{i-\frac{1}{2}}^{L} = min\left(1, r_{i-\frac{1}{2}}^{L}\right) \tag{4-35}$$

$$\phi_{i+\frac{1}{2}}^{R} = min\left(1, r_{i+\frac{1}{2}}^{R}\right) \tag{4-36}$$

The slope limiter used in figure 4-1 is the Barth-Jespersen limiter, and as can be observed in the figure, the unlimited dashed lines are corrected to the solid lines providing a monotonic increase or decrease between each cell center. However this limiter has problems with solutions converging to steady state, which is likely caused by the fact that functions like $min()$ and $max()$ cannot be differentiated. The limiter by Venkatakrishnan [44] is a suggestion to improve the limiter by Barth-Jespersen, improving the convergence for steady state.

4.1.4 Venkatakrishnan limiter

The general idea of the Venkatakrishnan limiter [44] is identical to the Barth-Jespersen limiter but replaces the $min()$ and $max()$ function with the continuous function $\phi = \frac{r^2+2\cdot r}{r^2+r+2}$. The difference between the function is visualized in figure 4-2, clearly showing that the Venkatakrishnan limiter is continuous, which will improve the convergence to steady state. To further improve the function a variable ϵ is added to the equation which will function as a threshold at which the limiter will function. This prevents the limiter from acting on very small disturbances that will diffuse on their own. As such, equation 4-35 and 4-36 become:

$$\phi_{i-\frac{1}{2}}^{L} = \frac{\left(r_{i-\frac{1}{2}}^{L}\right)^2 + 2\cdot r_{i-\frac{1}{2}}^{L} + \epsilon^2}{\left(r_{i-\frac{1}{2}}^{L}\right)^2 + r_{i-\frac{1}{2}}^{L} + 2 + \epsilon^2} \tag{4-37}$$

$$\phi_{i+\frac{1}{2}}^{R} = \frac{\left(r_{i+\frac{1}{2}}^{R}\right)^2 + 2\cdot r_{i+\frac{1}{2}}^{R} + \epsilon^2}{\left(r_{i+\frac{1}{2}}^{R}\right)^2 + r_{i+\frac{1}{2}}^{R} + 2 + \epsilon^2} \tag{4-38}$$

The suggestion of Venkatakrishnan was to set the variable ϵ as follows:

$$\epsilon^2 = K \cdot (\Delta x)^3 \tag{4-39}$$

Where Δx is the characteristic length of the cell and K is a parameter to be chosen in the $\mathcal{O}(1)$. Note that K is not dimensionless, according to the definition of ϵ and the definition of the limiter given by equation 4-37 and 4-38, the unit of K contains the dimension of the mesh size and the dimensions of the variable that is being limited. By setting $K = 0$ the limiter is always active and by setting K to some arbitrary number bigger than zero the limiter is not active until a certain threshold is surpassed, allowing for some deviations from monotonic behavior. Setting $K = 0$ is known to stall convergence, as can be seen in figure 4-3. Setting the value of K to higher values is known to create spurious oscillations near discontinuities (figure 4-4), or in other words, the limiter is not active when it should be to guarantee accurate numerical results.

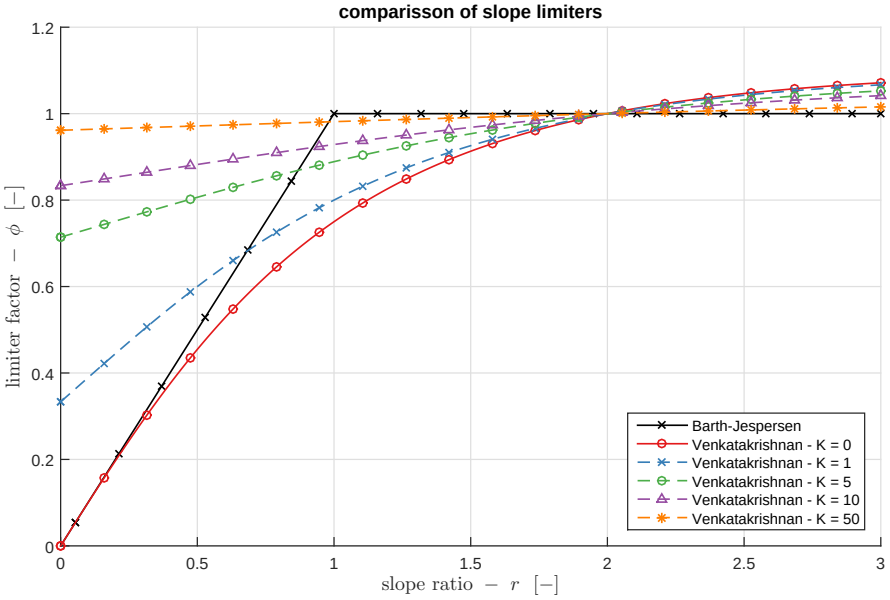

Figure 4-2: Comparison between Barth-Jespersen and Venkatakrishnan limiter

4.1.5 AUSM-HLLC hybrid flux scheme

As stated previously, the flux through the cell faces is evaluated using the extrapolated and limited value $q^*_{i\pm\frac{1}{2}}$, provided by the MUSCL scheme. Do note that each value of $q^*_{i\pm\frac{1}{2}}$ still has a left and a right state, as indicated by equation 4-29 and 4-30. To calculate the flux a hybrid scheme is used, consisting partially of the AUSM-plus-up scheme [8] [47] and partially of the HLLC scheme [7]. The scheme has been previously used by Koop [26] and Schmidt [48]. Both authors showed that the scheme is exceptionally useful for cavitating flows, which are characterized by high density ratios and a large differences in compressibility between the phases.

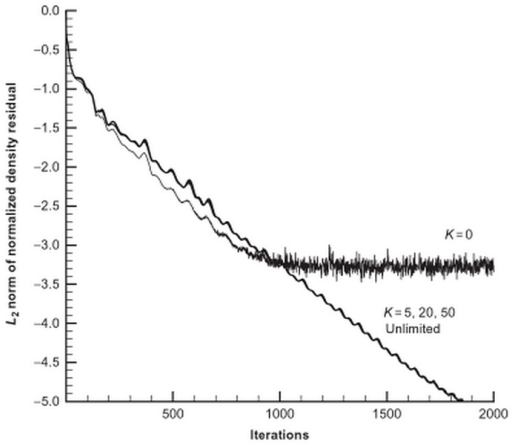

Figure 4-3: Convergence with Venkatakrishnan limiter for different values of K [46]

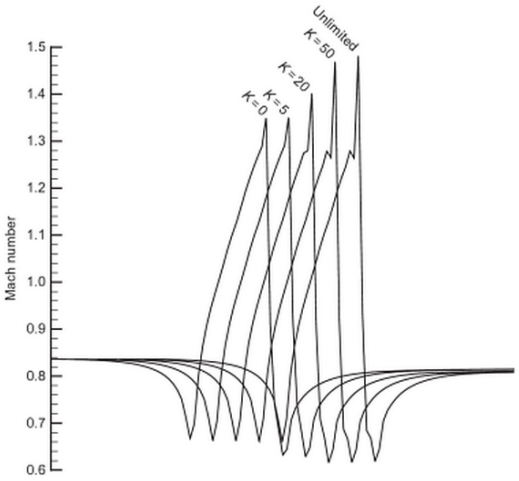

Figure 4-4: Solution with Venkatakrishnan limiter for different values of K [46]

The total flux $\hat{F}$ through the cell faces is given by:

$$\hat{F} = \dot{m}F_{conv} + F_{pressure} \tag{4-40}$$

For a three-dimensional situation the vectors of the fluxes are defined as:

$$F_{conv} = \begin{bmatrix} 1 \\ u_{L,R} \\ v_{L,R} \\ w_{L,R} \\ H_{L,R} \end{bmatrix} \tag{4-41}$$

$$F_{pressure} = \begin{bmatrix} 0 \\ \hat{p} \\ \hat{p} \\ \hat{p} \\ 0 \end{bmatrix} \tag{4-42}$$

The calculation of the total flux $\hat{F}$ is done in a similar manner to the AUSM schemes. The flux is split into two parts, a convective flux and a pressure flux. The hybrid scheme uses the AUSM-plus-up scheme to calculate the pressure flux. The convective flux is calculated by multiplying the mass flow through the cell with the convective velocities as given by vector F_{conv}. The mass flow for the convective fluxes is calculated by HLLC-scheme.

Equation 4-43 through 4-51 describe the procedure to obtain the pressure flux using the AUSM-plus-up scheme:

$$\begin{aligned}\hat{p} &= \mathcal{P}^{+}_{(5)}(M_L)\cdot p_L + \mathcal{P}^{-}_{(5)}(M_R)\cdot p_R \\ &- K_u \cdot \mathcal{P}^{+}_{(5)}(M_L)\cdot \mathcal{P}^{-}_{(5)}(M_R)\cdot p_R \cdot (\rho_L+\rho_R)\cdot(u_R-u_L)\cdot f_c \frac{c_L+c_R}{2}\end{aligned} \tag{4-43}$$

$$\mathcal{P}^{\pm}_{(5)} = \begin{cases} (1/M)\mathcal{M}^{\pm}_{(1)} & \text{if } |M|\geq 1 \\ \mathcal{M}^{\pm}_{(2)}\left[(\pm 2 - M) \mp 16\gamma M \mathcal{M}^{\mp}_{(2)}\right] & \text{if } |M|<1 \end{cases} \tag{4-44}$$

$$\mathcal{M}^{\pm}_{(1)} = \pm(M\pm 1)^2 \tag{4-45}$$

$$\mathcal{M}^{\pm}_{(2)} = \frac{1}{2}(M\pm|M|) \tag{4-46}$$

$$f_c = M_0(2-M_0)\in[0,1] \tag{4-47}$$

$$K_u = \frac{3}{4} \tag{4-48}$$

$$M_0 = min\left(1, max\left(\bar{M}^2, M_\infty^2\right)\right)\in[0,1] \tag{4-49}$$

$$\bar{M}^2 = \frac{u_L^2+u_R^2}{2\left(\frac{c_L+c_R}{2}\right)^2} \tag{4-50}$$

$$\gamma = \frac{3}{16}(-4+5f_c) \tag{4-51}$$

The value of M_∞^2 in equation 4-49 is the Mach number squared of the flow in the far field. The purpose of this parameter is to provide additional stability to the scheme. For the purpose of cavitating flows, the value of M_∞^2 will be close to zero in the far field, due to the combination of flow velocities with $\mathcal{O}(10)$ and the speed of sound around 1430 m/s for pure liquid water. Equation 4-52 through 4-55 describe the procedure to obtain the mass flow for the convective flux using the HLLC scheme:

$$\dot{m} = \begin{cases} \rho_L u_L & \text{if } Z_L \geq 0 \\ \rho_L u_L + Z_L\left(\rho_L \frac{Z_L-u_L}{Z_L-Z_M} - \rho_L\right) & \text{if } Z_L<0\leq Z_M \\ \rho_R u_R + Z_R\left(\rho_R \frac{Z_R-u_R}{Z_R-Z_M} - \rho_R\right) & \text{if } Z_M<0\leq Z_R \\ \rho_R u_R & \text{if } Z_R<0 \end{cases} \tag{4-52}$$

$$Z_L = min(u_L-c_L, u_R-c_R) \tag{4-53}$$

$$Z_R = max(u_R+c_R, u_L+c_L) \tag{4-54}$$

$$Z_M = \frac{p_R-p_L+\rho_L u_L(Z_L-u_L)-\rho_R u_R(Z_R-u_R)}{\rho_L(Z_L-u_L)-\rho_R(Z_R-u_R)} \tag{4-55}$$

4.2 Implementation of the cavitation model in 1D

The eventual goal of the 1D-simulations is to model cavitation in a Venturi-like nozzle. This simulation will combine the physical models discussed in chapter 3 and the numerical methods from this chapter to obtain a full model of cavitating flow in a nozzle. The 1D-simulation will not provide a fully accurate picture of cavitation since it is area averaged along a single axis. In reality the vapor will form pockets that are attached to the wall of the nozzle as shown by fig 4-5, requiring at least 2 dimensions to accurately depict the flow field. As stated in the introduction the 1D simulation will be used as proof of concept for the solving strategy, observing if the solver is stable and to qualitatively validate the physics involved in the cavitation process.

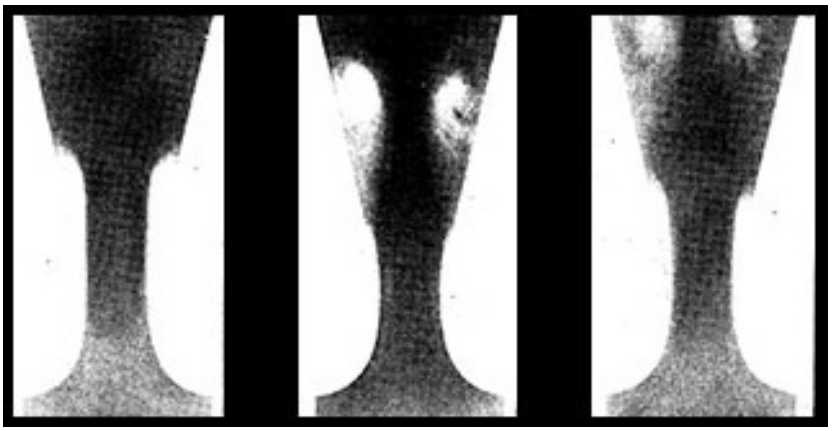

Figure 4-5: Visualization of cavitation in a nozzle [49]

4.2.1 Non-reflecting boundary conditions

Due to the nature of the compressible solver, the formation of shock waves is captured by the numerics. When general zero-gradient boundary conditions are applied for the pressure field, these spurious pressure waves will reflect off the boundaries of the domain and keep reflecting back and forth. Eventually the diffusion created by the solver (numerical or physical) will absorb the shock waves. There are different options to prevent these shock waves from interfering with the solution and stop the reflecting behavior. One option could be to enlarge or lengthen the domain of the calculation, forcing the shock waves to travel longer distances through the diffusive fluid before hitting a boundary. But in the case of the Matlab solver this is not possible, as it uses inviscid Euler equations, meaning that the shock waves need to damp out using only the very limited numerical diffusion present. Depending on the severity of the numerical diffusion this could take a very long time.

The other option is to use non-reflecting boundary conditions. The mathematical framework of these special boundary conditions can be found in the work of Poinsot and Lele [50]. In the work of Koop [26] these boundary conditions are worked out further so they can be applied to the set of Euler equations. Assuming that the velocity is prescribed at the inlet and the pressure is prescribed at the outlet, the following set can be used to calculate the boundary conditions:

$$\bar{c} = mean\left(c(1), c(2), c(n-1), c(n)\right) \tag{4-56}$$

$$CFL = \frac{u \cdot \Delta t}{\Delta x} \tag{4-57}$$

$$p_{g,inlet} = \frac{p(1) + \frac{1}{2} \cdot CFL\left[p(2) + p(1) + \rho(1) \cdot c(1) \cdot (u_{inlet} - u(2))\right]}{1 + CFL} \tag{4-58}$$

$$p_{g,outlet} = \frac{p(n) + \frac{1}{2} \cdot CFL\left[p(n-1) + p_{outlet} + \rho(n) \cdot c(n) \cdot (u(n-1) - u(n))\right]}{1 + CFL} \tag{4-59}$$

$$u_{g,inlet} = \frac{u(1) + \frac{1}{2} \cdot CFL\left(\frac{p(1)-p(2)}{\rho(1)\cdot c(1)} + u_{inlet} + u(2)\right)}{1 + CFL} \tag{4-60}$$

$$u_{g,outlet} = \frac{u(n) + \frac{1}{2} \cdot CFL\left(\frac{p(n-1)-p_{outlet}}{\rho(n)\cdot c(n)} + u(n) + u(n-1)\right)}{1 + CFL} \tag{4-61}$$

$$\rho_{g,inlet} = \left[\frac{p_{g,inlet} - p_{sat}}{K_0} + 1\right]^{\frac{1}{N}} \cdot \rho_l \tag{4-62}$$

$$\rho_{g,outlet} = \left[\frac{p_{g,outlet} - p_{sat}}{K_0} + 1\right]^{\frac{1}{N}} \cdot \rho_l \tag{4-63}$$

In the equations the grid is one-dimensional having n cells, starting at 1. The internal grid starts at 2 and stops at n-1. The first and last cell are so called 'ghost points', these two points are not part of the solution but are used to enforce the boundary conditions and can assume values that strongly differ from the internal grid.

4.2.2 MATLAB code

Matlab version R2014b [51] is used to implement the previously discussed set of physical models and numerical methods to provide a solution for the 1D problem. The Matlab code is too extensive and contains too many sub-functions to be fully discussed and reviewed. A full printout of the code has been included in appendix A. The features used in the 1D code are:

- 4^{th} order Runge Kutta time stepping (chapter 4.1)
- MUSCL face extrapolation scheme (chapter 4.1.1)
- AUSM-HLLC hybrid scheme (chapter 4.1.5)
- Euler equations with 1-dimensional area change (chapter 4.1)
- CEV equation of state (chapter 3.2.3)
- CFL limited time step (chapter 4.1)
- non-reflecting boundary conditions (chapter 4.2.1)

The flowchart shown in figure 4-6 gives an overview of the iterative algorithm followed by the implementation of the models for the 1D situation:

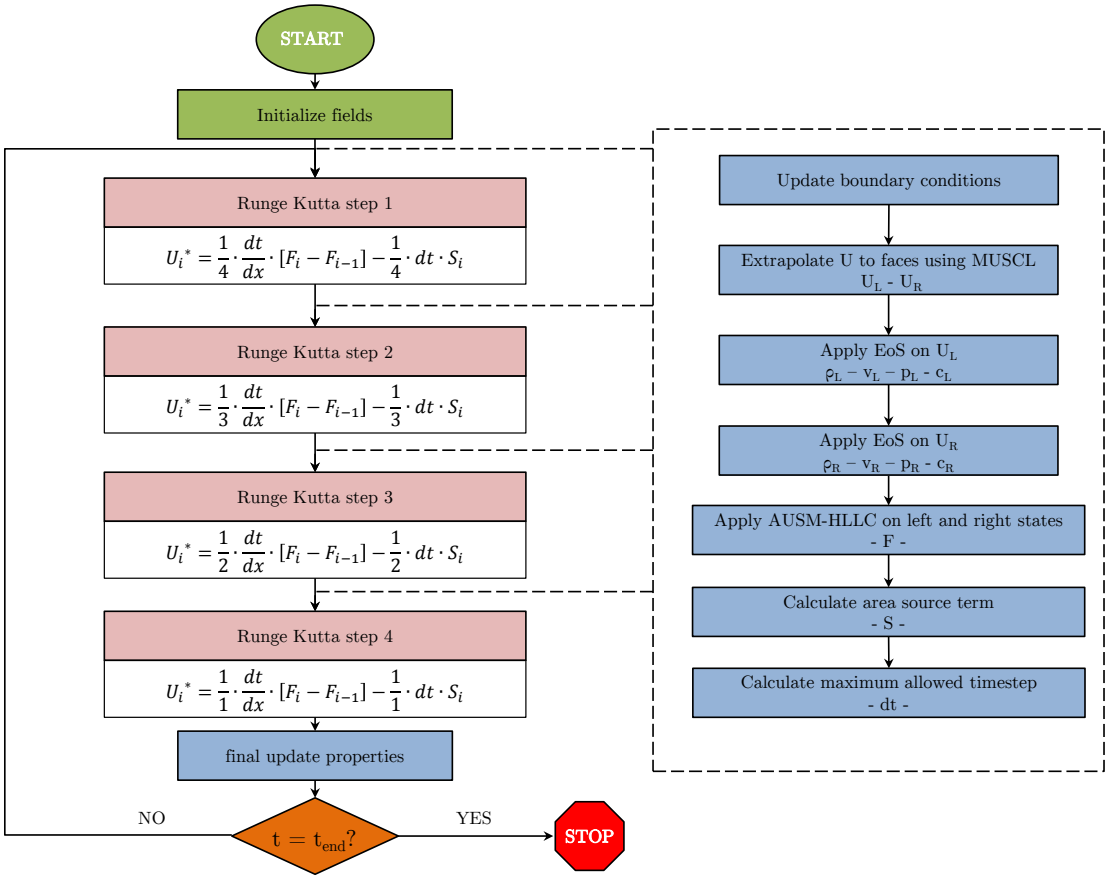

Figure 4-6: Flowchart of the 1-dimensional calculation algorithm

4.3 Implementation of the cavitation model in 2D

The eventual goal of the 2D-simulations is to model cavitation around a hemispherical head shape. The simulation is developed as an application inside the OpenFOAM library. This simulation will combine the physical models discussed in chapter 3 and the numerical methods from this chapter to obtain a full model of cavitating flow. The 2D-simulation will provide a more accurate picture of the cavitation than the 1D-simulation, in the sense that it will actually show a zone of cavitation instead of a mean quantity along a single axis. Having a visual cavitation zone also provides the possibility to visually check if the shape of the cavitation is physically possible and comparable to images taken during the reference experiments. As stated in the introduction the 2D simulation will be used to further validate the models used, observing if the solver is still stable in 2D on a structured grid and to quantitatively validate the physics involved in the cavitation process.

4.3.1 Compressible Navier-Stokes

The Euler equations are inviscid, but the viscosity of a liquid plays an important role in the closure of the cavitation pocket and the shape of the cavitation pocket, as explained in the work of Tseng and Shyy [52]. To obtain quantitatively accurate results during the validation in 2D, the inviscid simplification is no longer valid. Thus the inviscid Euler equations are upgraded to include viscosity, forming the compressible Navier-Stokes equations, shown in equation 4-64 through 4-68. These equations completely replace the Euler equations shown in equation 4-13 through 4-15. The viscosity is the summation of two parts, the physical viscosity of the mixture and the turbulent viscosity provided by the turbulence models, as seen in equation 4-66. Also the assumption is made that the viscosity of the fluid can be taken as the volume (void fraction) averaged viscosity of the liquid and the vapor phase, as seen in equation 4-67.

$$\frac{\partial \rho}{\partial t} + \nabla \cdot (\rho U) = 0 \tag{4-64}$$

$$\frac{\partial \rho U}{\partial t} + \nabla \cdot (\rho U \otimes U) + \nabla (pI) = \nabla \cdot \left[\mu_{eff} \left(\nabla U + (\nabla U)^T - \frac{2}{3} I \nabla \cdot U \right) \right] \tag{4-65}$$

$$\mu_{eff} = \mu + \mu_t \tag{4-66}$$

$$\mu = \alpha \cdot \mu_l + (1 - \alpha) \cdot \mu_v \tag{4-67}$$

$$\rho = f(p) \tag{4-68}$$

Equations 4-64 through 4-68 can be written into a single system containing the vectors U, F and V. The system formed by vectors U (equation 4-70) and F (equation 4-71) is basically identical to the set of Euler equations as shown in chapter 4.1. The vector V (equation 4-72) only contains the term τ, which represents the total viscous stresses, formed by the right hand side of equation 4-65. By writing the compressible Navier-Stokes equation as a system, it is shown that this system is almost identical to the Euler equations, only including an additional stress component to account for the viscosity caused by the fluid and the turbulence. The main advantage is that this system can be treated with the same numerical methods and schemes as the Euler equations used for the 1D implementation.

$$\frac{\partial U}{\partial t} + \nabla \cdot F = \nabla \cdot V \tag{4-69}$$

$$U = \begin{bmatrix} \rho \\ \rho U \end{bmatrix} \tag{4-70}$$

$$F = \begin{bmatrix} \rho U \\ \rho U U \end{bmatrix} \tag{4-71}$$

$$V = \begin{bmatrix} 0 \\ \tau \end{bmatrix} \tag{4-72}$$

4.3.2 κ-ω Shear Stress Transport (κ-ω-SST) model

The κ-ω-SST by Menter [53] is chosen to model the turbulence. This model is a merger of the κ-ϵ model by Launder and Sharma [54] and the original κ-ω by Wilcox [55]. The κ-ω model is known for its abilities to accurately predict the turbulence close to the wall, all the way down to the viscous sub-layer and to correctly predict separation zones. The downside of the κ-ω model is that it is heavily influenced by the turbulence boundary conditions in the free-stream zone far away from the wall. The κ-ϵ model is relatively insensitive to these boundary conditions and provides a more accurate view of the turbulence development in the area far away from the wall. The κ-ω-SST model combines the best of both worlds by switching and averaging between the κ-ϵ and the κ-ω models depending on the distance from the wall. Equations 4-73 through 4-82 fully describe the κ-ω-SST model:

$$\nu_t = \frac{a_1 k}{\max(a_1\omega, SF_2)} \tag{4-73}$$

$$\frac{\partial k}{\partial t} + U_j \frac{\partial k}{\partial x_j} = P_k - \beta^* k\omega + \frac{\partial}{\partial x_j}\left[(\nu + \sigma_k \nu_T)\frac{\partial k}{\partial x_j}\right] \tag{4-74}$$

$$\frac{\partial \omega}{\partial t} + U_j \frac{\partial \omega}{\partial x_j} = \alpha S^2 - \beta\omega^2 + \frac{\partial}{\partial x_j}\left[(\nu + \sigma_\omega \nu_T)\frac{\partial \omega}{\partial x_j}\right] + 2(1-F_1)\sigma_{\omega 2}\frac{1}{\omega}\frac{\partial k}{\partial x_i}\frac{\partial \omega}{\partial x_i} \tag{4-75}$$

$$F_2 = \tanh\left[\left[\max\left(\frac{2\sqrt{k}}{\beta^*\omega y}, \frac{500\nu}{y^2\omega}\right)\right]^2\right] \tag{4-76}$$

$$P_k = \min\left(\tau_{ij}\frac{\partial U_i}{\partial x_j}, 10\beta^* k\omega\right) \tag{4-77}$$

$$F_1 = \tanh\left\{\left\{\min\left[\max\left(\frac{\sqrt{k}}{\beta^*\omega y}, \frac{500\nu}{y^2\omega}\right), \frac{4\sigma_{\omega 2} k}{CD_{k\omega} y^2}\right]\right\}^4\right\} \tag{4-78}$$

$$CD_{k\omega} = \max\left(2\rho\sigma_{\omega 2}\frac{1}{\omega}\frac{\partial k}{\partial x_i}\frac{\partial \omega}{\partial x_i}, 10^{-10}\right) \tag{4-79}$$

$$\sigma_{k1} = 0.85, \qquad \sigma_{k2} = 1 \tag{4-80}$$

$$\sigma_{\omega 1} = 0.5, \qquad \sigma_{\omega 2} = 0.856 \tag{4-81}$$

$$\mu_t = \rho\nu_t \tag{4-82}$$

The parameters α and β are different for the κ-ϵ and the κ-ω models. The F1-function (equation 4-78) is used to provide a weighted average between the two parameters.

$$\phi = \phi_1 F_1 + \phi_2(1 - F_1) \tag{4-83}$$

$$\alpha_1 = \frac{5}{9}, \qquad \alpha_2 = 0.44 \tag{4-84}$$

$$\beta_1 = \frac{3}{40}, \qquad \beta_2 = 0.0828 \tag{4-85}$$

$$\beta^* = \frac{9}{100} \tag{4-86}$$

This model is readily implemented in the OpenFOAM library but still requires input from the user, in the form of suitable boundary conditions.

4.3.3 Turbulence boundary conditions

Unless one is interested in the full startup of turbulence, starting with a stationary flow field, it is sensible to prescribe a certain amount of turbulence at the inlet of the domain. To correctly prescribe the levels turbulence at the inlet of the domain, the user is required to calculate or estimate the kinetic energy (E_k) and the specific turbulence dissipation (ω) at these boundaries. Kinetic energy E_k can easily be estimated by the known free stream velocity U_∞ and an assumed value for the intensity I of the turbulence [56]:

$$E_k = \frac{3}{2}(UI)^2 \tag{4-87}$$

The value of I is generally chosen between 0.001 (0.1%) for very weak turbulence and 0.05 (5%) for very strong turbulence. The specific turbulence dissipation is hard to estimate directly because it is not directly related to free stream quantities. One way to estimate the specific turbulence dissipation is to base its value on the dominant length scale of the problem, for instance the inlet diameter of the nozzle. However for external flows, as is the case for the current 2D problem, it is very hard to identify the characteristic length scale of the problem and how it relates to the dimensions of the object. For external flow it is preferable to assume a turbulent viscosity ratio β in the free stream and derive a free stream value for the specific turbulence dissipation given that ratio. The following relation is used to estimate the specific turbulence dissipation, given the density, ρ, viscosity, μ, turbulent viscosity ratio, β, and the kinetic energy E_k of the turbulence [56]:

$$\omega = \frac{\rho E_k}{\mu} \cdot \beta^{-1} \tag{4-88}$$

The value of β is generally chosen between 1 for almost laminar flows and 10 for highly turbulent flows when external flow problems are considered. For internal flows the value of β can increase to 100 for highly turbulent flows, but as stated before, most internal turbulent flows are easier to describe using characteristic length scales.

4.3.4 Far-field treatment

Although the 1D and 2D implementation use the same basic code and can both be described by roughly the same system of equations, there are differences in the approach for the boundary conditions. The 1D implementation required the use of non-reflecting boundary conditions in order to minimize the reflections that would otherwise be reflected back into the nozzle, introducing unphysical oscillations in the solution. The 2D implementation has the advantage that the flow for this scenario is external and viscous, in other words, the shock waves are free to travel away from the relevant geometry, while being dissipated through the viscosity of the surrounding fluid. If the domain is chosen large enough, most of the shock waves will dissipate before hitting any boundaries. The disadvantage of this method is that it will enlarge the domain far beyond what would be necessary to accurately model the flow, meaning that the flow is not influenced by the presence of the walls at the far edges of the domain. To guarantee that the flow field is not disturbed by the shock waves, the previously discussed methods are combined. The domain is chosen sufficiently large to prevent influences from the walls, and the relevant boundary edges contain non-reflecting boundary conditions. This combination ensures that shock waves are weakened before hitting the wall, where the boundary conditions stop the shock wave from reflecting back to the cavitating zone of the geometry. The non-reflecting boundary conditions are implemented in an identical manner to the 1D implementation, as described in chapter 4.2.1. The documentation that is accompanying OpenFOAM refers to the same paper by Poinsot and Lele [50], confirming that the mathematics involved are functionally identical to the 1D implementation.

4.3.5 OpenFOAM code

OpenFOAM Extend edition version 3.1 is used to implement the previously discussed set of physical models and numerical methods to provide a solution for the 2D problem. The OpenFOAM code is much more complex than the Matlab code. OpenFOAM is a very elaborate library for mathematical field manipulations. The solver is based on the existing density-based Navier Stokes solver "dbnsTurbFoam" by Hrvoje Jasak [57] [58]. Runge Kutta time stepping and MUSCL face extrapolation using the Venkatakrishnan limiter are already present in this application. The existing solver is modified to include the AUSM-HLLC flux scheme, barotropic EoS and volume averaged fluid viscosity. Instead of writing out every modification, a printout of the code that covers the main application has been included in appendix B. This application contains many references to other parts of the OpenFOAM library, the interested reader can further explore the OpenFOAM library by visiting the online depository of the code [59]. The flowchart shown in figure 4-7 gives an overview of the application written in OpenFOAM used for the 2-dimensional application. The features used in the 2D code are:

- 4^{th} order Runge Kutta time stepping (chapter 4.1)
- MUSCL face extrapolation scheme (chapter 4.1.1)
- AUSM-HLLC hybrid scheme (chapter 4.1.5)
- Compressible Navier-Stokes equations (chapter 4.3.1)

- κ-ω-SST turbulence model (chapter 4.3.2)
- CEV equation of state (chapter 3.2.3)
- CFL limited time step (chapter 4.1)

The flowchart shown in figure 4-7 gives an overview of the iterative algorithm followed by the implementation of the models for the 2D situation:

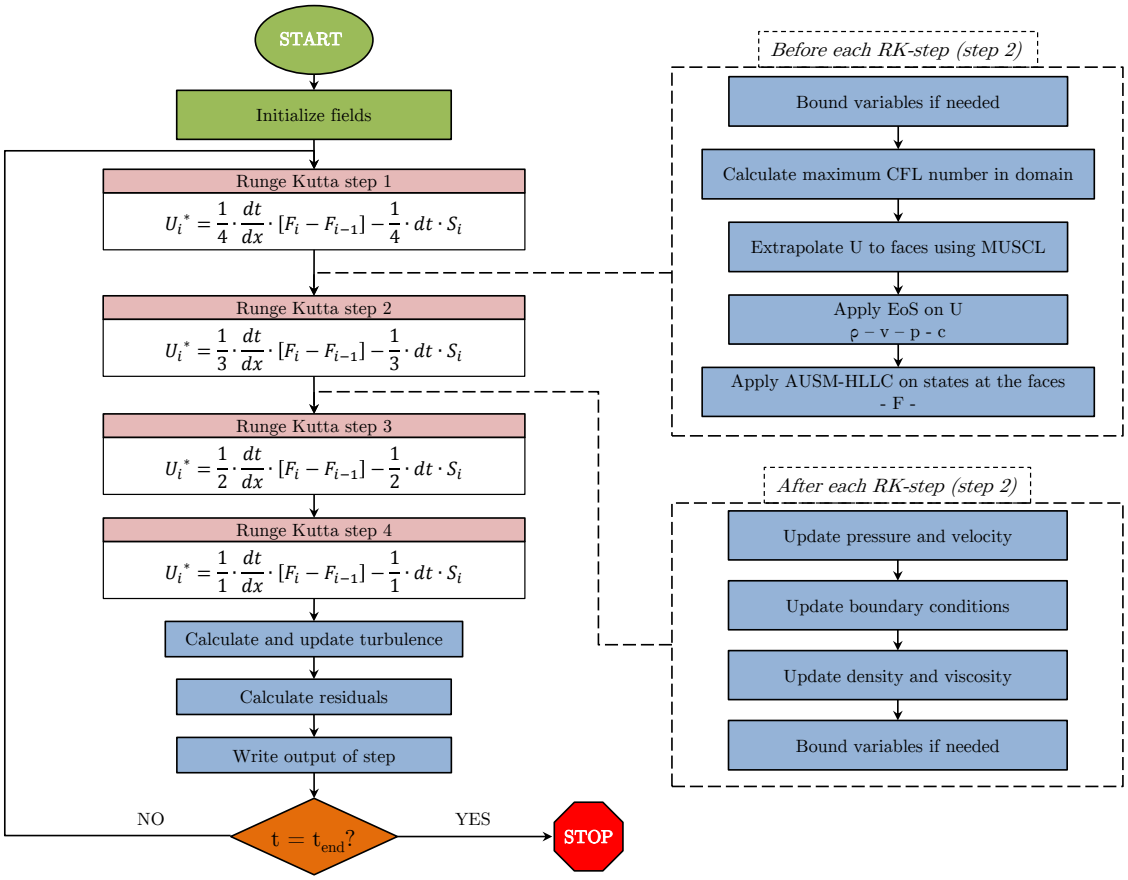

Figure 4-7: Flowchart of the 2-dimensional calculation algorithm

Chapter 5

1D modeling results

The purpose of this chapter is to present and review the results obtained with the 1D models, pointing out key observations derived from the results. Firstly an overview of the input of the model is presented, listing all fluid properties and boundary conditions that are imposed on the model. Secondly the output of the model is studied, making general observations on the functioning of the model. Also the output for each fluid is studied to observe how cavitation will differ for different fluids and their properties, resulting in a qualitative validation of the model.

5.1 Setup and boundary conditions

The first step in the process to validate the models, as presented in chapters 3 and 4, is to implement the models in a simplified 1D situation. The objective of this step is pure qualitative validation. The details describing the 1D implementation can be found in chapter 4.2 including the motivation behind the choice to only qualitatively validate the 1D situation. The maximum allowable time step for each iteration is calculated based on the compressible CFL number (equation 4-12). The compressible CFL number is taken equal to 0.9.

The geometry of interest is a Venturi-like nozzle with a circular cross section as depicted in figure 5-1. The area of the inlet and outlet of the nozzle is $2m^2$, the throat of the nozzle narrows to $1m^2$. The nozzle is $2m$ in length, the converging section starts $0.5m$ after the inlet and is fully diverged again $0.5m$ before the outlet. The throat area is described by: $A(x) = 1 + sin(\pi \cdot x)^2$, in which x is defined as the axial coordinate in meters. The 1D domain is divided in 252 cells, 250 cells form the actual solution domain of the problem and a single cell at both the inlet and the outlet are marked as 'ghost points' to assist with the application of the boundary conditions.

The boundary conditions are implemented as non-reflecting boundaries, described in chapter 4.2.1. At the inlet the velocity is prescribed and at the outlet the pressure is prescribed. The inlet velocities are equal to $8m/s$, $9m/s$ and $10m/s$ for all three fluids.

Water is taken as the reference case, the outlet pressure for water is taken equal to 1.0 *bar* for all three inlet velocities. This results in cavitation numbers equal to $\sigma = 3.0575$, $\sigma = 2.4158$ and $\sigma = 1.9568$, respectively for each inlet velocity. The inlet velocities for butane and propane are equal to those of water. The outlet pressures for butane and propane are scaled with the cavitation number (equation 2-7) to obtain comparable cases between the three fluids.

The Venkatakrishnan limiter [44] contains a tunable parameter K that has to be set in order to limit the solution without influencing the final answer. After a process of trial and error the parameter K was set to a value of 0.3 to obtain the best results in the 1D cavitating nozzle. Note that for the 2D situation, the value of K likely has to been changed to be compatible with the flow and geometry of that problem (internal flow vs. external flow).

To prevent confusion all 9 scenarios (3 cavitation numbers for 3 different fluids) are printed at the end of this chapter, figure 5-2 through 5-10. The red plots represent the cases involving water, the blue plots represent the cases involving butane and the green plots represent the cases involving propane. The conclusions that can be drawn from the results are split into two parts, one part commenting on the general performance of the model (chapter 5.3) and the second part commenting on the differences that have been found between the fluids (chapter 5.4).

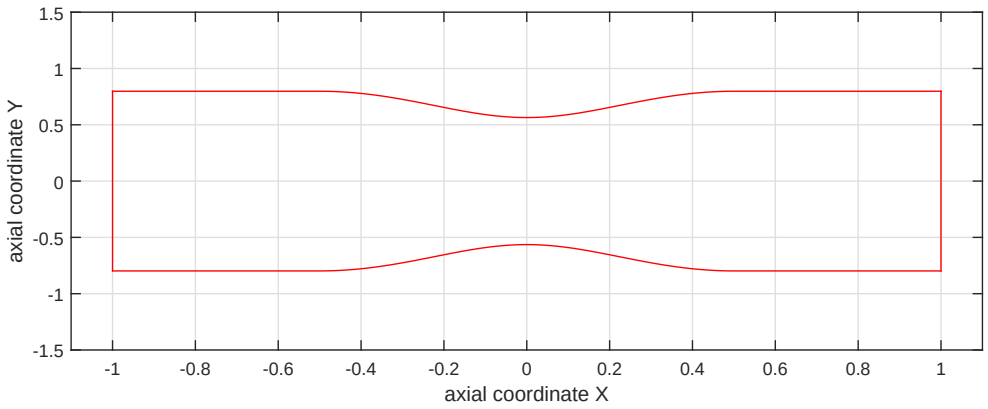

Figure 5-1: plot of nozzle geometry, throat section is defined by $A(x) = 1 + sin(\pi \cdot x)^2$

5.2 Fluid properties used in the simulations

To avoid ambiguity surrounding the fluid properties, table 5-1 provides a full overview of all the fluid properties used. All three fluids are evaluated at $293K$, using the Fluidprop [5] software that relies on the Refprop [60] library for butane and propane and relies on the IF97-library [61] for the properties of water. The constants and coefficients used for the equations of state are fitted according to the methods described in chapter 3.4 At the bottom of the table all the inlet and outlet boundary conditions can be found as calculated using the cavitation number to scale the outlet pressures for each fluid.

Table 5-1: Overview of all parameters, coefficients and constants as used in the 1D cases

fluid name	water	butane	propane	unit
library	IF97	RefProp, butane	RefProp, propane	-
temperature - T	293.15	293.15	293.15	K
density - liquid - ρ_l	998.1608	578.5912	500.0569	kg/m^3
density - vapor - ρ_v	0.0173	5.3126	18.0823	kg/m^3
ratio	57655	109	28	-
saturation pressure - p_{sat}	$2.3392 \cdot 10^3$	$2.0765 \cdot 10^5$	$8.3646 \cdot 10^5$	Pa
critical pressure - p_{crit}	$2.2064 \cdot 10^7$	$3.7960 \cdot 10^6$	$4.2512E \cdot 10^6$	Pa
Tait equation - K_0	$3.6904 \cdot 10^8$	$4.7779 \cdot 10^7$	$2.5835 \cdot 10^7$	Pa
Tait equation - N	5.9496	10.4209	10.9740	–
CEV model - coefficient a	0.01262	0.01726	0.01747	–
CEV model - coefficient b	-0.6014	-0.5168	-0.5136	–
CEV model - coefficient c	0.8241	1.4654	1.2094	–
CEV model - parameter gV	0.8870	0.9424	0.9084	–
inlet velocity - case 1	8.00	8.00	8.00	m/s
inlet velocity - case 2	9.00	9.00	9.00	m/s
inlet velocity - case 3	10.00	10.00	10.00	m/s
outlet pressure	$1.0000 \cdot 10^5$	$2.6426 \cdot 10^5$	$8.8539 \cdot 10^5$	–
cavitation number - σ - case 1	3.0575	3.0575	3.0575	Pa
cavitation number - σ - case 2	2.4158	2.4158	2.4158	Pa
cavitation number - σ - case 3	1.9568	1.9568	1.9568	Pa

5.3 Cavitation in a nozzle: general observations

The general idea of compressible modeling has clearly succeeded since even the highest cavitation numbers, which show no cavitation for butane and propane (figure 5-5 and 5-8), are compressed by a very small amount. The density changes for butane and propane in these cases are in the order of a tenth of a percent or even less. Even for these 'weakly' compressible liquids the model provides satisfying results, confirming that the AUSM-HLLC works for very low Mach flows and weakly compressible liquids. The effects of high compressibility are also captured by the scheme, as can be seen for the lowest cavitation number (figure 5-4, 5-7 and 5-10), where the inlet pressure and the outlet pressure substantially differ due to the compressibility of the vapor phase. Most likely there is also a small difference in inlet and outlet pressure for the non-cavitating situations (figure 5-5 and 5-8) due to the weakly compressible saturated liquid, but this effects is so small that it cannot be observed in the results.

One of the properties of the Euler equations is that they are inviscid. If the weakly compressible effects of the fluid are ignored, the solution of the Euler equations can be approached with Bernoulli's principle. The calculation of the classical case of the Venturi nozzle results in values that are very close to the results of the Euler equations (neglecting compressibility of the liquid). For instance, the solution of water for $\sigma = 3.075$ (figure 5-2) shows that the lowest pressure very close to p_{sat} since the fluids is barely cavitating. Using Bernoulli's principle and assuming that the inlet conditions are saturated liquid density, $1.0bar$ of pressure, and $8m/s$ inlet velocity, the result would be equal to a velocity of $16.1m/s$ through the throat of the Venturi. This is in good agreement with the model.

The boundaries are enforced at the inlet and the outlet. No oscillations are observed at either the inlet or the outlet and no waves are traveling back and forth through the domain, concluding that the non-reflecting boundary conditions are working as intended.

Another interesting feature of the barotropic model is the fact that it actually has to operate below vapor pressure to lower the density below the saturated liquid density. This is easily observed in figure 5-10. The saturation pressure is around $8.36bar$ but at the minimum value for the density the pressure goes slightly below $7bar$. As will be discussed in the conclusions (chapter 7), detailed information about the pressure inside the cavitation zone can be used to estimate the energy that will be released when the bubbles implode and what level of damage can be expected.

From figure 3-3 in chapter 3.2.3 it was known that the isenthalpic speed of sound can assume extremely low values and that this lowest values occurs as soon as any vapor forms in the liquid. When the vapor content is increased, the isenthalpic speed of sound steadily increases towards the speed of sound of the saturated vapor. This effect is also clearly observed in the results of the 1D models. In all situations where cavitation occurs, the inception point is just to the right of the throat ($x = 0$). The inception point coincides with the largest value of the Mach number, as would one expect based on the findings from figure 3-3. Also the decrease of Mach number for increasing void fraction is found back in the models. In figure 5-4 one can clearly see that the velocity is constant between $x = 0$ and $x = 0.4$, but the Mach number decreases due to the decreasing density. Figure 5-4 provides another example to validate correct barotropic behavior of the model, namely in the section between $x = 0.6$ and $x = 0.8$ the density, pressure, velocity and mach number are all constant. If the density is constant,

the pressure should also be constant due to the barotropic nature of the model. The speed of sound is related to the density through the void fraction, thus the speed of sound should also be constant in the range between $x = 0.6$ and $x = 0.8$. Finally, the constant velocity combined with the constant speed of sound results in a constant Mach number in the range between $x = 0.6$ and $x = 0.8$, concluding that the coupling between density, pressure and speed of sound is correct.

The closure of the cavitation zone is very sudden in the 1D models. In general it appears that the density switches from its minimum value back to the saturated liquid density within 1 or 2 cells. From a numerical standpoint it shows that the combination of the MUSCL interpolation scheme and the AUSM-HLLC flux scheme handles this discontinuity very well. From a physical standpoint the behavior is deemed physical. The time needed for a cavitation bubble to collapse (the so-called "Rayleigh time") has been described by Rayleigh [62] [63], resulting in the following equation:

$$t_{Rayleigh} = 0.915 \cdot R_0 \sqrt{\frac{\rho_l}{p_\infty - p_{sat}}} \tag{5-1}$$

For a cavitation bubble with a radius of 1 cm in water ($\rho_l = 998\ kg/m3$ and $p_{sat} = 2339\ Pa$) with a far-field pressure of 1 bar, the bubble collapses in about 1 ms. This calculation shows that the bubble collapses very fast en very violent, supporting the statement that the density change can physically take place in the span of only a few cells. If some sort of stable sheet cavitation would form on the inside of the nozzle (left picture in figure 5-1) it is possible that the interface from a 1D perspective is very sharp, resulting in the very sudden switch from minimum density back to saturated liquid density. On the other hand, one has to keep in mind that the physics that govern the closure of the sheet and the flow patterns that emerge in this zone are very complex and cannot be fully described in only one dimension.

The biggest shortcoming of the 1D implementation is the area-averaged density. All three fluids go down to 40%-60% of their saturated liquid density ($\alpha = 0.4 - 0.6$), but never come close to the actual density of their respective vapor phases. One could try to relate the void fraction of the fluid to the cross area of the nozzle that is occupied by vapor. However for this to work, one must assume that the fluid is either saturated liquid or saturated vapor and that this area grows annularly from the walls of the nozzle to the central axis of the flow. The density of the fluid, as shown in figures 5-2 through 5-10, can be taken as an indicator of the intensity of the cavitation by calculating the void fraction. Thus knowing what part of the cross section is occupied by vapor at a certain axial coordinate x. But since the cavitation is not perfectly mixed, the shape and location of the cavitation cannot be predicted by a 1D model.

5.4 Cavitation in a nozzle: different fluids

Except for general observations that look at the model as a whole, interesting observation can also be made by looking at the similarities and differences that exist between the fluids. These differences can occur either due to the fluid properties that influence the fluid mechanics directly (like density) or they can occur due to the fluid properties that influence the numerics

of the problem, like the speed of sound heavily influences the flux calculations of the AUSM scheme.

In the cavitating regions of water (figure 5-2 through 5-4) the Mach number reaches values between 300 and 500. This is a consequence of the very low isenthalpic speed of sound for relatively low void fractions. If the void fraction is lower than 0.5, the isenthalpic speed of water is lower than $0.08m/s$ with a minimum of $0.03m/s$ for the smallest possible void fraction. Most likely this is not physical, since the experiments by Karplus [29] and Brown & Gouse [30] have shown that the physical values are close to the isothermal speed of sound as discussed in chapter 2.2.3. The problem however is not the physics but the numerics, the very high Mach numbers combined with the high liquid-vapor density ratios will cause the scheme to struggle with discontinuities.

Propane for $\sigma = 2.4158$ (figure 5-9) shows a different numerical problem related to the Mach number. In the plot of the Mach number it can be observed that the Mach number is relatively close to 1.0 when the fluid is cavitating. Without going in too much detail, the AUSM scheme contains a number of functions that are intended to switch between subsonic and supersonic treatment for the flux terms. If the fluid in a cell is well below $Ma = 1.0$, but the neighbour is above and close to this switching point at $Ma = 1.0$, the resulting flux calculation can become inaccurate due to averaging between subsonic and supersonic treatment. The eventual result is a small discontinuity, as can be observed in the pressure results of figure 5-9 and 5-10 at $x = -0.05$.

Another interesting difference can be found when comparing the three fluids for the highest cavitation number ($\sigma = 3.0575$) near inception. Comparing figures 5-2, 5-5 and 5-8, it appears that butane and propane, although very close to inception, do not cavitate. Water on the other hand just crosses the inception threshold, resulting in a small dip in density. It is most likely caused by the differences in fluid properties, since the liquid density is almost two times larger and the speed of sound is almost two times larger for water ($\rho_l = 998\ kg/m^3$ and $c_l = 1483\ m/s$), than for butane ($\rho_l = 578\ kg/m^3$ and $c_l = 928\ m/s$), and propane ($\rho_l = 500\ kg/m^3$ and $c_l = 752\ m/s$), resulting in a significantly lower compressibility for water compared to butane and propane. If the numerical scheme introduces a small error that is enough to lower the pressure below the saturation pressure, this could also result in the different inception behavior for water. In an attempt to rule out numerical issues, the calculation for the scenario (water $\sigma = 3.0575$) has been repeated several times with different limiter options and time step sizes. The resulting steady states of the scenarios remained unchanged, showing that the difference in inception is caused by the physical differences between the fluids and not due to numerical treatment. The compressibility of liquid water is significantly lower than the compressibility of liquid butane and liquid propane. The lower liquid compressibility resulted in a slightly lower pressure in the throat, causing the water scenario to cross the cavitation threshold, as observed in figure 5-2.

The main difference between the three fluids is the liquid-vapor density ratio, which is equal to 57655 for water, 109 for butane and a mere 28 for propane at a temperature of $293K$. The influence of the liquid-vapor density ratio is also observed in the momentum of the vapor phase. Even if large volumes of water vapor were to form, the total weight of the vapor is much smaller than the total weight of the liquid due to the low density of the vapor. Thus for water the momentum of the vapor phase is negligible compared to the momentum of the vapor. But for butane and propane the weight of the vapor will play a role for equal amounts

of volume. Looking at figure 5-4, 5-7 and 5-10, which show the most severe cavitation for each fluid, the influence of the momentum difference is seen in the velocity plots for each fluid. For water the cavitation starts at $x > 0$ and even though the density is lowered significantly and large amounts of vapor are created the velocity stays at a (near) constant $20m/s$. For butane and propane the cavitation also starts at $x > 0$ but this time the velocity that is obtained at the throat (around $20m/s$) is increased by the (non-negligible) momentum contribution of the vapor phase, increasing the velocity obtained, which is now higher than the velocity obtained at the throat. This effect appears to be stronger for lower liquid-vapor density ratios, which makes sense from the perspective of the momentum balance that exists between the phases and the relative contribution of the vapor phase.

The pressure oscillations that occur when the cavity is closed (for instance the pressure plot in figure 5-4) also seem to depend on the liquid-vapor density ratio of the fluid, since these oscillations are clearly present for water, less pronounced for butane, but almost invisible for propane. Which can be explained by the fact that, if for each liquid equal amounts of volume are fully evaporated through cavitation at $293K$, water will increase its volume by a factor of 57655, while butane will only increase its volume by a factor of 28. The cause of these oscillations is numerical instead of physical, the numerical scheme can compensate for large changes in density but when the order of the change becomes too large, the scheme can no longer facilitate a smooth transition and this will result in an overshoot of the solution. The oscillations can be weakened by adjusting constant K of Venkatakrishnan's limiter as discussed in chapter 4.1.4. If constant K is chosen large enough ($K = 15$) the oscillations will almost disappear but this will also heavily influence the steady state solutions, since monotonicity is no longer guaranteed (also see figure 4-4 and 4-3). In summary, it is clear that the severity of the pressure oscillations is dictated by the liquid-vapor density ratio, but that it is the limiting procedure that introduces the oscillations into the solution. The solution to increase constant K is not an option because it will heavily influence the steady state solution.

Finally, some observations concerning the actual differences in the density profile development for equal values of cavitation number σ are discussed. The most important observation is related to the cavitation length for each fluid. This is the axial distance between the x-coordinate at which the cavitation begins and the x-coordinate at which the cavitation disappears. In general the cavitation length of water is the longest, followed by butane and propane has the shortest cavitation length. This is contrasted by the lowest density obtained in the cavitation zone, the density of propane is lowered to about 40% of its liquid saturated density. Butane is lowered to about 48% and water is lowered to about 50% of its liquid saturated density. From these observations it may be stated that propane has a shorter cavity length than water, but the intensity or density reduction is larger. One may even speculate that the mass involved in each fluid is about equal but there is a certain trade-off between the intensity and the cavitation length for each fluid. However for 1D models this remains speculation. Also the choice for a void fraction that represents the actual cavitation region is rather arbitrary. For instance, is it reasonable to call a region with a void fraction of only 1% cavitation? The vapor transport models, as described in chapter 2.2.4, assume a certain threshold for the void fraction (50% or 80%) below which the fluid is considered to cavitate. It is important to be aware of the value of this threshold because the same threshold is used to calibrate the empirical coefficient of these models. A more detailed 2D picture is

required to actually see the cavitation shape and the density profile differences from the edge of the sheet down to the wall.

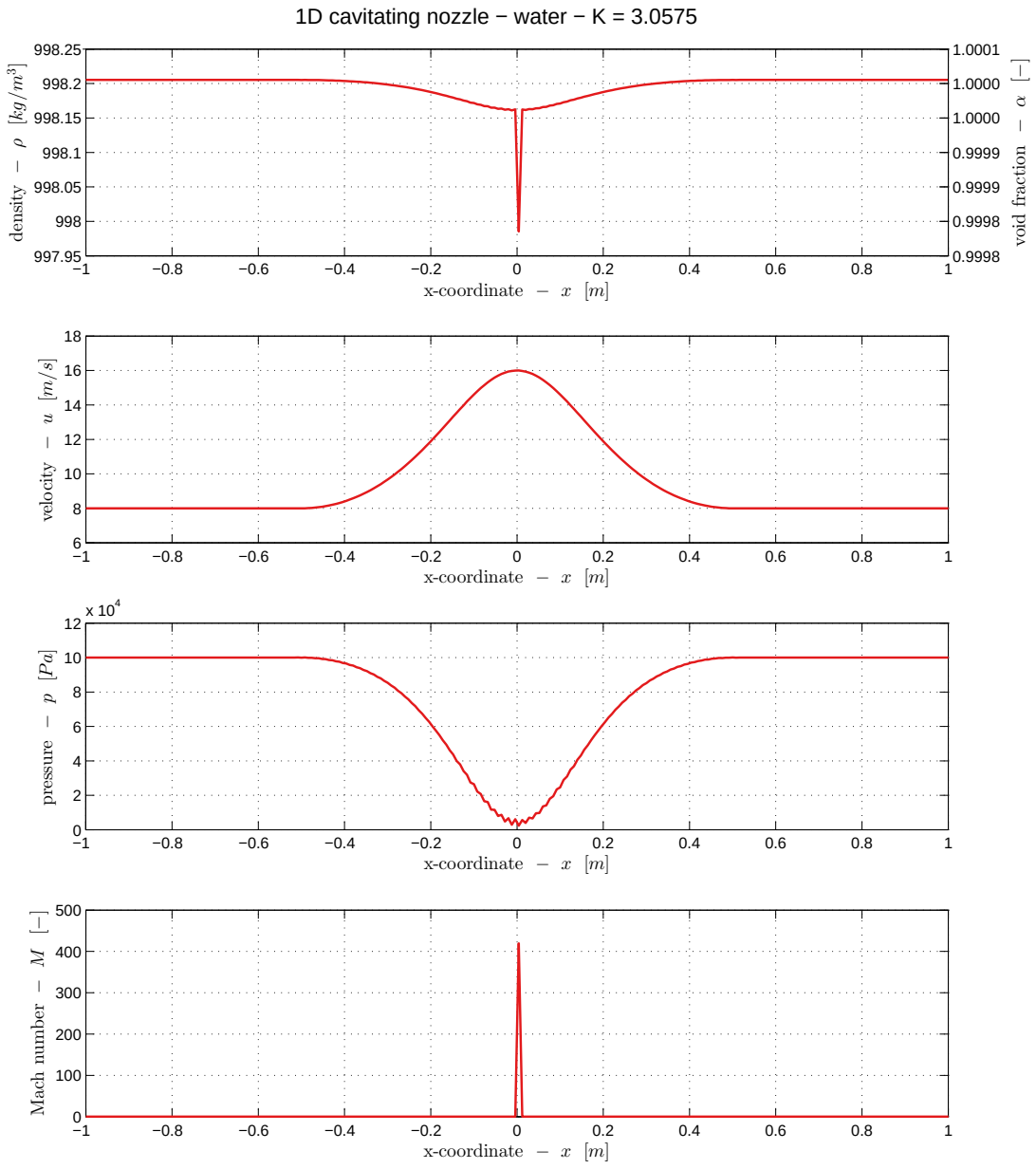

Figure 5-2: 1D cavitating nozzle - water - $\sigma = 3.0575$, plots of density, velocity, pressure and Mach number versus the axial coordinate x

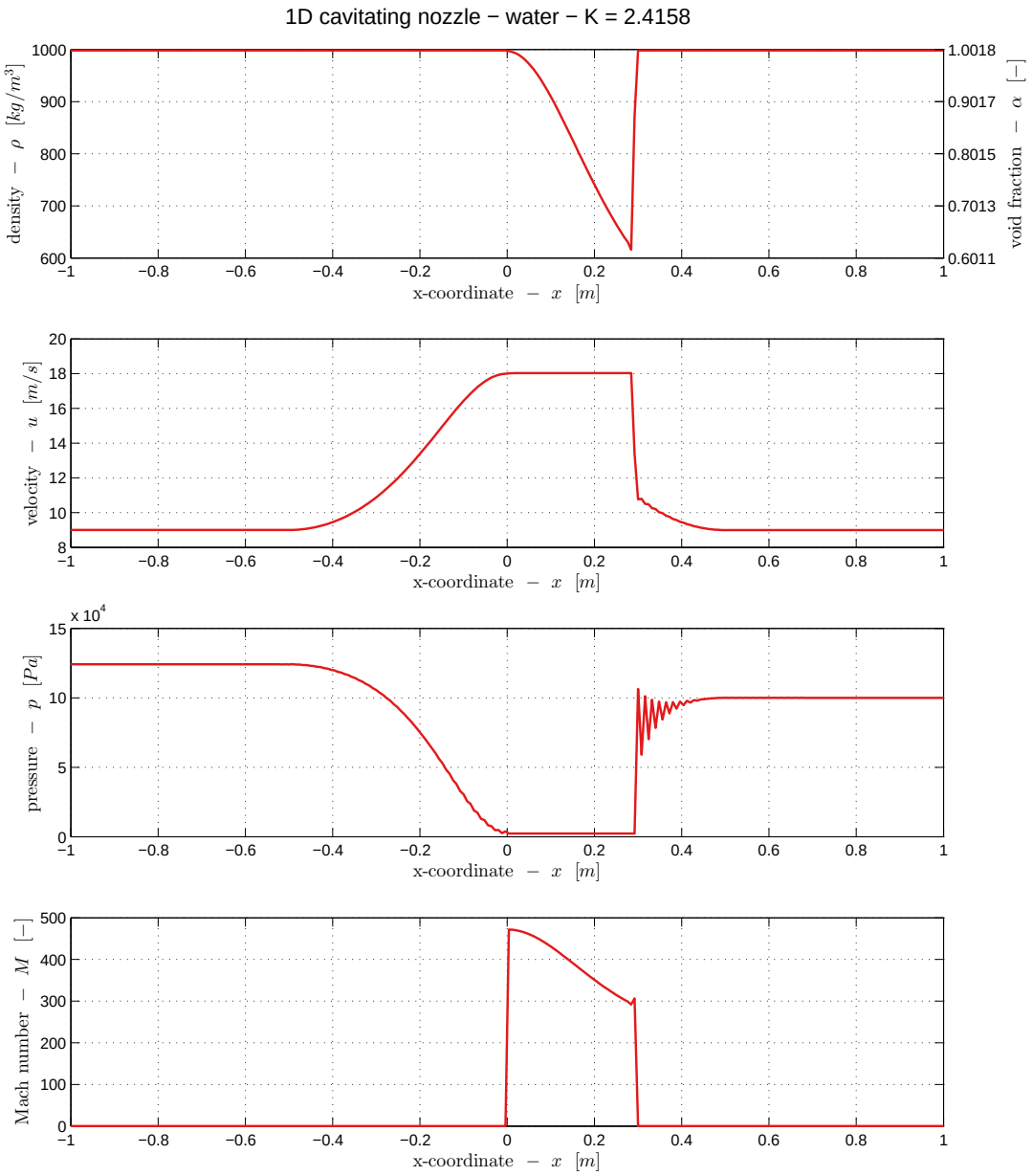

Figure 5-3: 1D cavitating nozzle - water - $\sigma = 2.4158$, plots of density, velocity, pressure and Mach number versus the axial coordinate x

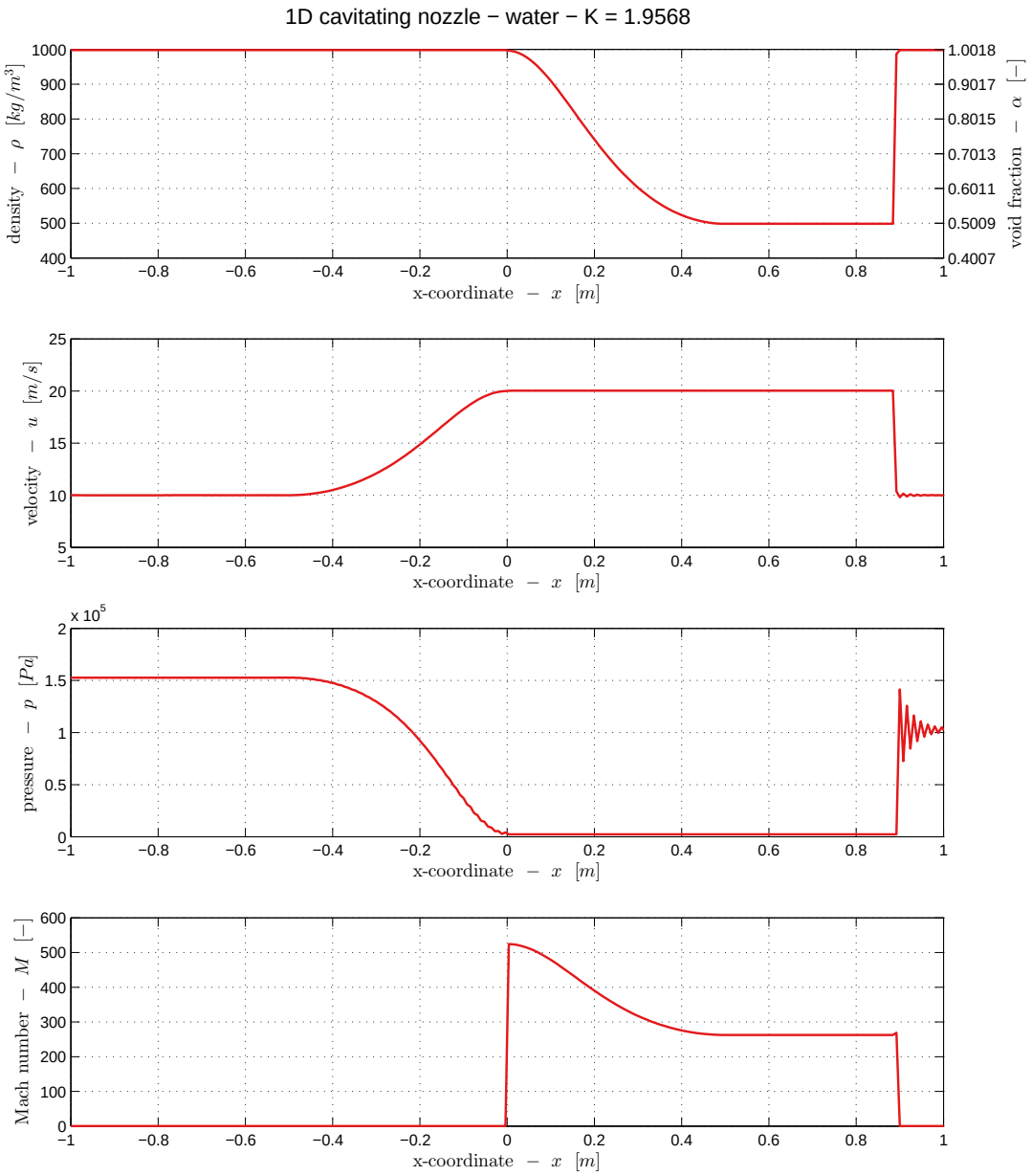

Figure 5-4: 1D cavitating nozzle - water - $\sigma = 1.9568$, plots of density, velocity, pressure and Mach number versus the axial coordinate x

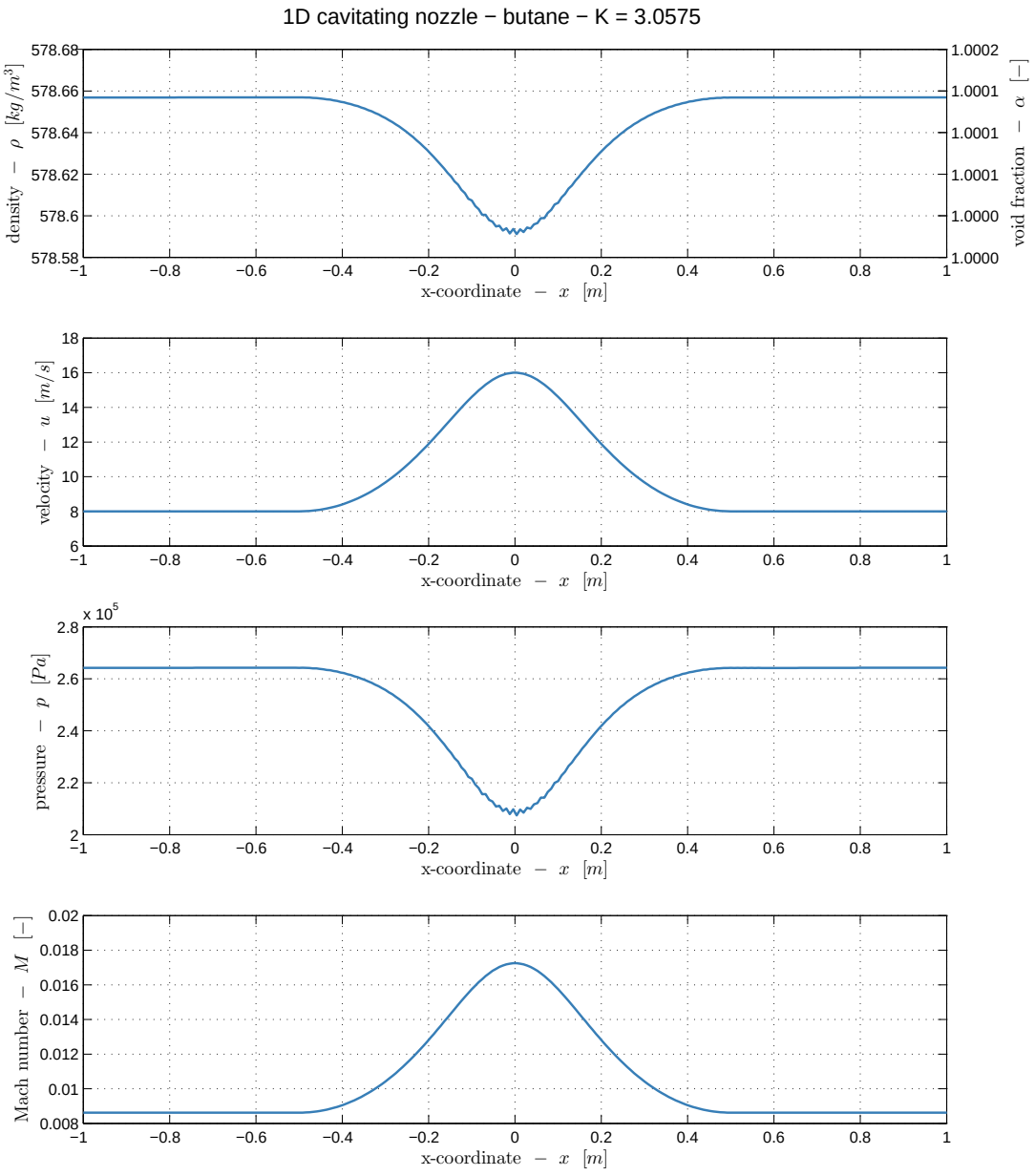

Figure 5-5: 1D cavitating nozzle - butane - $\sigma = 3.0575$, plots of density, velocity, pressure and Mach number versus the axial coordinate x

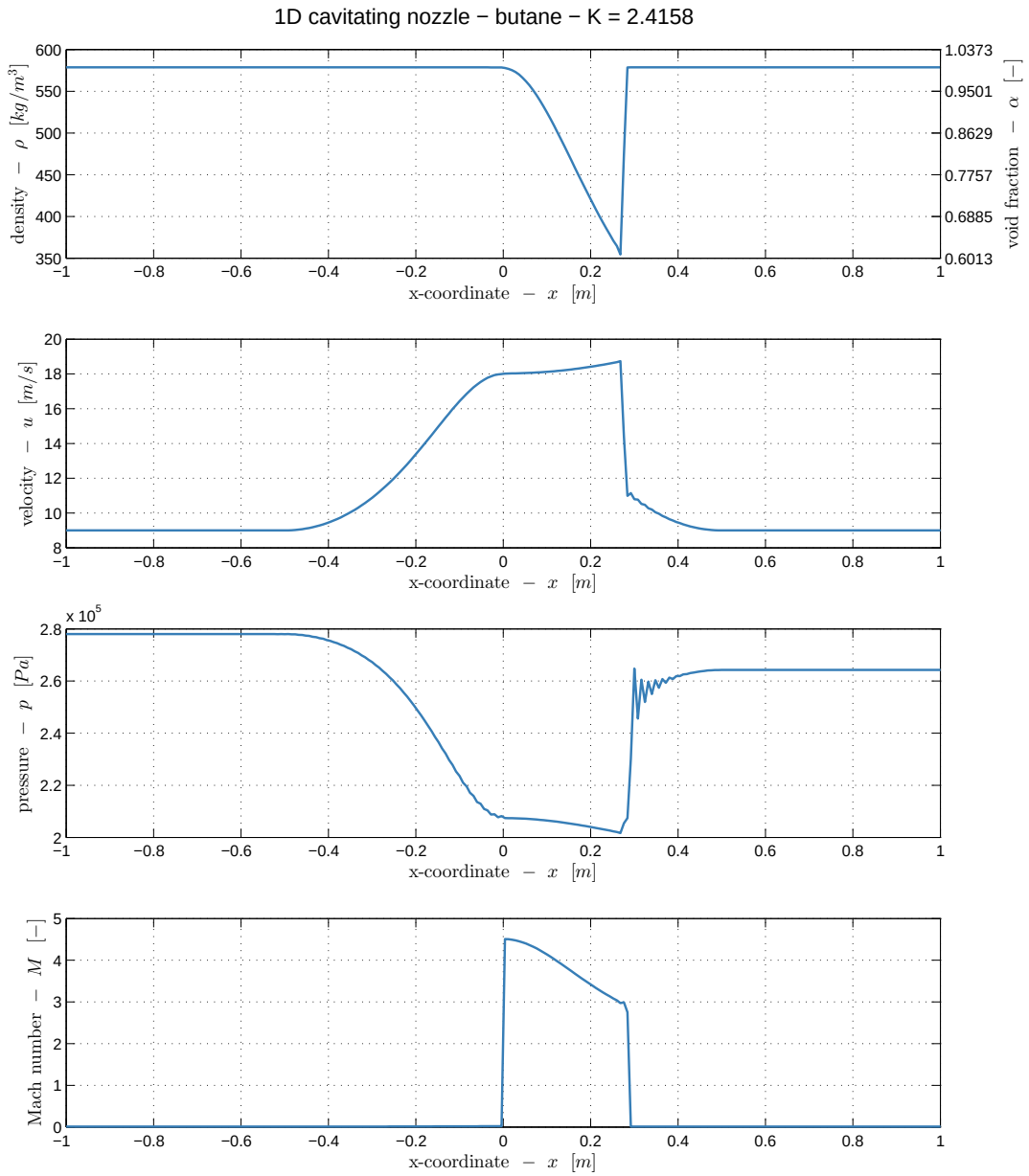

Figure 5-6: 1D cavitating nozzle - butane - $\sigma = 2.4158$, plots of density, velocity, pressure and Mach number versus the axial coordinate x

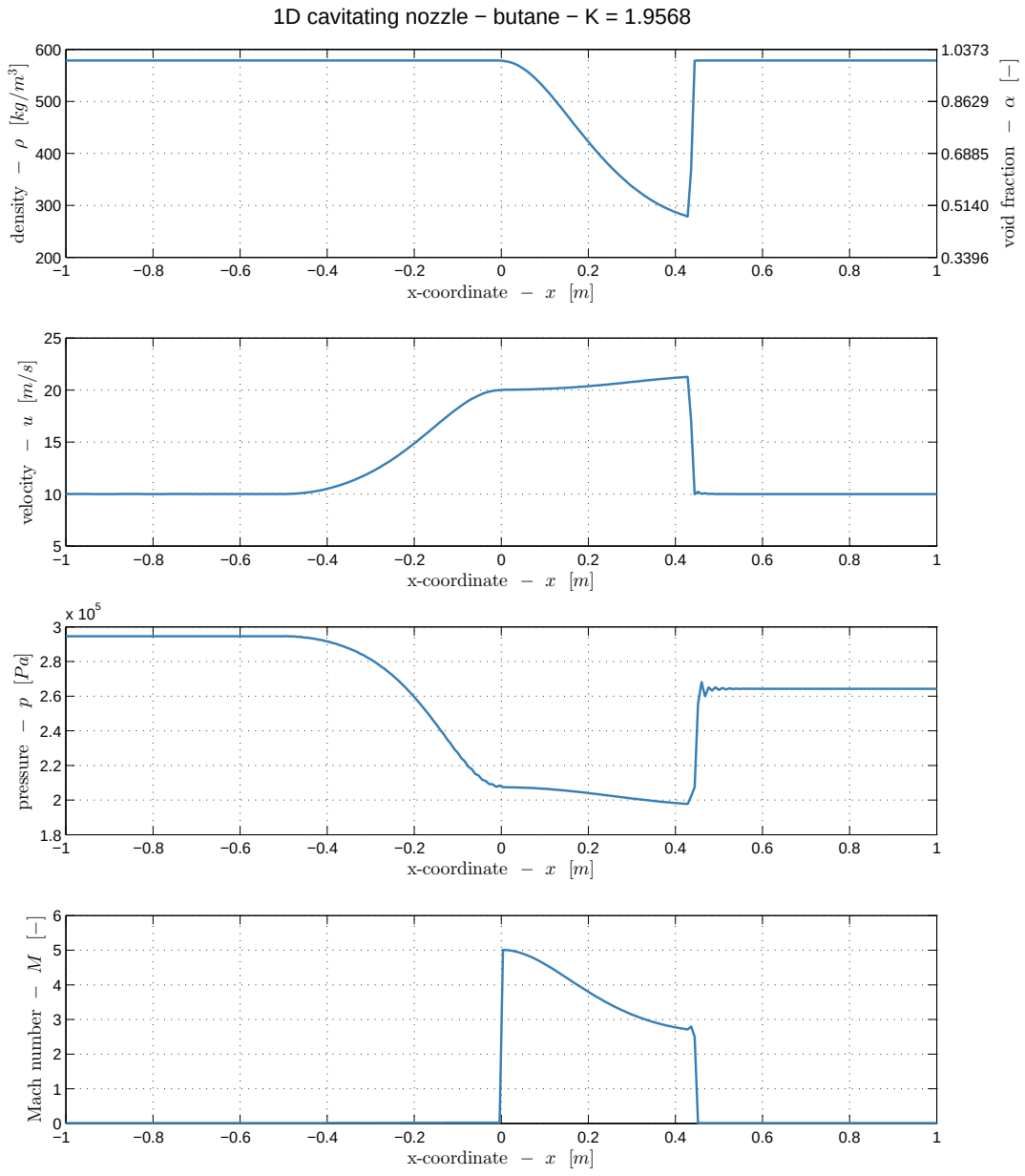

Figure 5-7: 1D cavitating nozzle - butane - $\sigma = 1.9568$, plots of density, velocity, pressure and Mach number versus the axial coordinate x

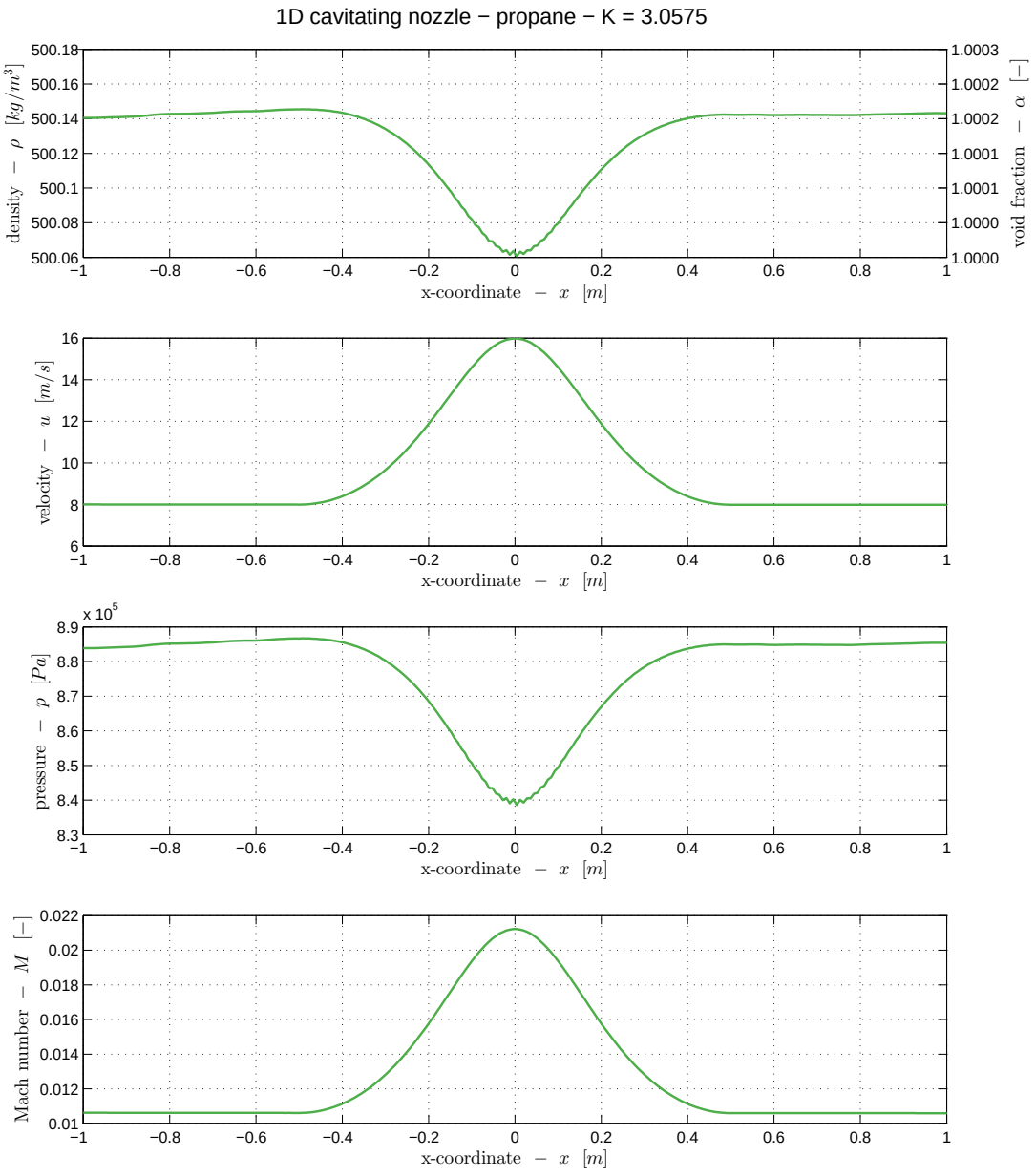

Figure 5-8: 1D cavitating nozzle - propane - $\sigma = 3.0575$, plots of density, velocity, pressure and Mach number versus the axial coordinate x

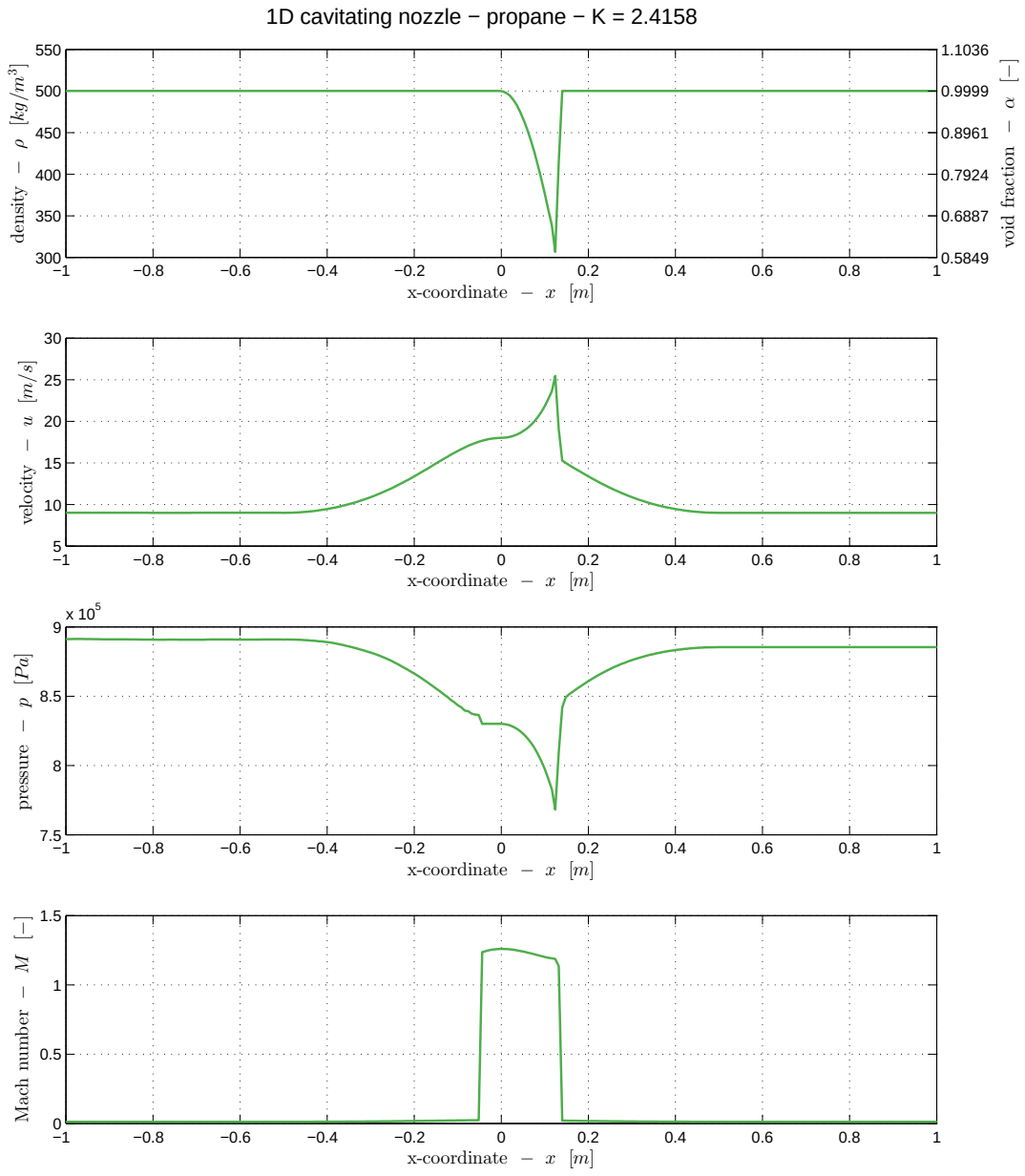

Figure 5-9: 1D cavitating nozzle - propane - $\sigma = 2.4158$, plots of density, velocity, pressure and Mach number versus the axial coordinate x (note the discontinuity at $x = -0.05$ as discussed in the third paragraph of chapter 5.4)

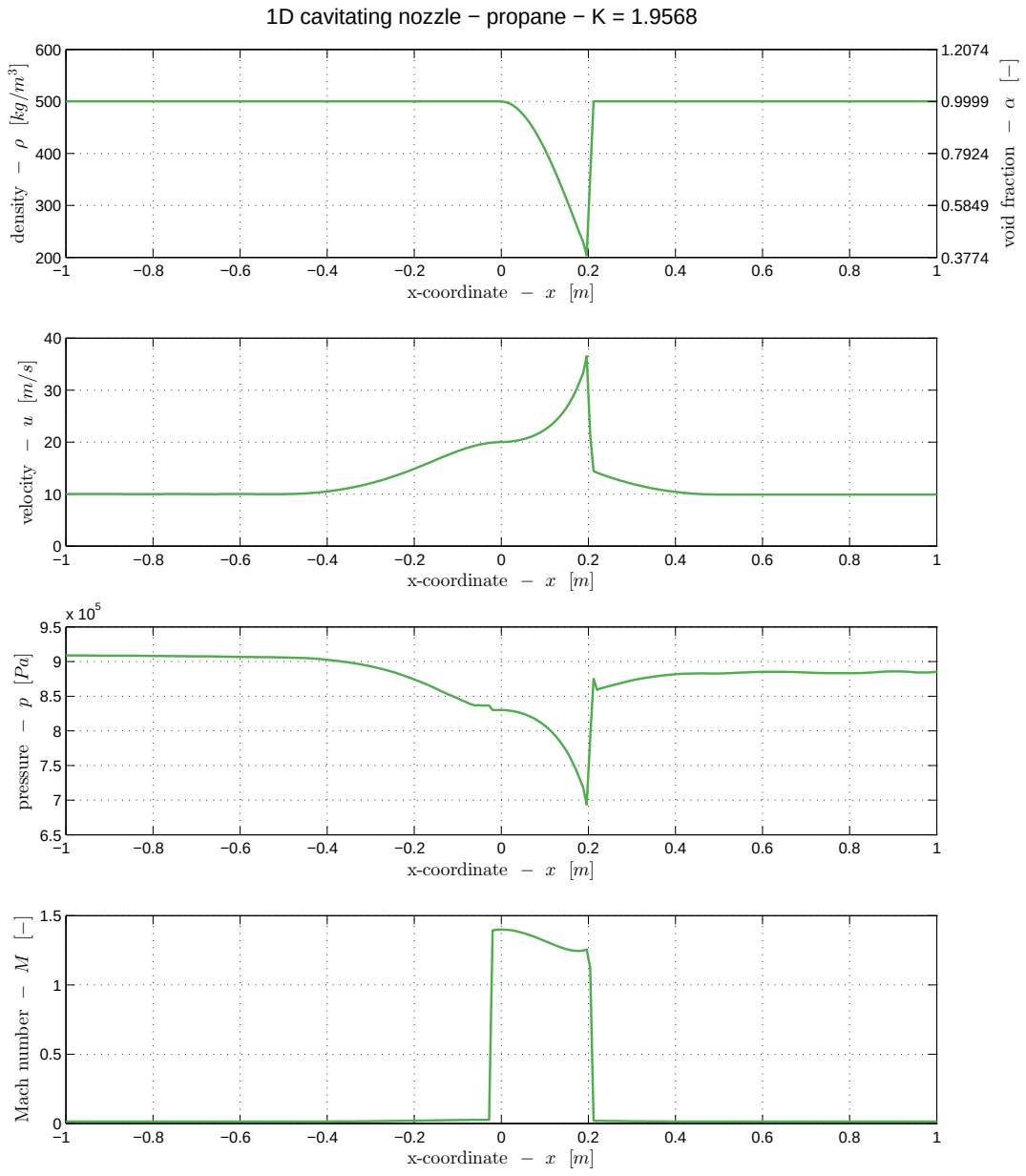

Figure 5-10: 1D cavitating nozzle - propane - $\sigma = 1.9568$, plots of density, velocity, pressure and Mach number versus the axial coordinate x (note the discontinuity at $x = -0.05$ as discussed in the third paragraph of chapter 5.4)

Chapter 6

2D modelling results

The purpose of this chapter is to present and review the results obtained with the 2D-models, pointing out key observations derived from the results. Firstly an overview of the input of the model is presented, listing all fluid properties and boundary values that are imposed on the model. Secondly the output of the model is studied, making general observations on the functioning of the model. Also the output of water simulation is processed to obtain a pressure profile and is compared with the experimental results by Rouse & McNown [9], resulting in a simple quantitative validation of the model.

6.1 Setup and boundary conditions

The second step in the process to validate the models as presented in chapters 3 and 4 is to implement the models in a full 2D situation. The objective of this step is simple quantitative validation by comparing the obtained pressure profile with experimental data by Rouse & McNown [9]. The details describing the 2D-implementation can be found in chapter 4.3. The maximum allowable time step for each iteration is calculated based on the compressible CFL number (equation 4-12). The compressible CFL number is taken equal to 0.1.

The geometry of interest is a round rod with a hemispherical head at the tip. When a fluid is flowing over the shape at the correct conditions, cavitation will form as depicted in figure 6-1. The rod has a cross-section with a radius r which is also the radius of the hemispherical head. In the experiments of Rouse & McNown [9] the rod has a diameter of exactly 1.00 inch, thus radius r is equal to 12.7 mm. All other dimensions of the calculation domain are based on radius r. The domain extends 50 radii behind the hemispherical head and the circular zone surrounding the hemispherical head extends 30 radii outwards. A sketch of the geometry is given by figure 6-2. Due to the extremely small time step ($\mathcal{O}(10^{-8})$) that has to be taken to keep the solution stable, based on the compressible CFL number (as explained in chapter 4.1), the total number of time steps that has to be taken in order to model only a few milliseconds is in the order of millions. Thus it is a priority to keep the cell count of the 2D model as low as possible or the total execution time will go towards an impracticable range. Due to

the symmetrical nature of the head shape and rod it is possible to reduce the 3D geometry to a 2D axisymmetric geometry. By taking a small pie-shaped wedge of the geometry, with the width of only 1 cell, the total number of cells is limited to 16,800. There are 80 cells along the curve of the nose, 200 cells from the end of the nose to the end of the domain and between the wall of the head shape and the edge of the domain are 60 cells. The cell count in each direction is given by the bracketed numbers in figure 6-2. The resulting structured mesh can be seen in figure 6-3. Note that the mesh is refined towards the nose, resulting in a more dense mesh in the region where cavitation is to be expected.

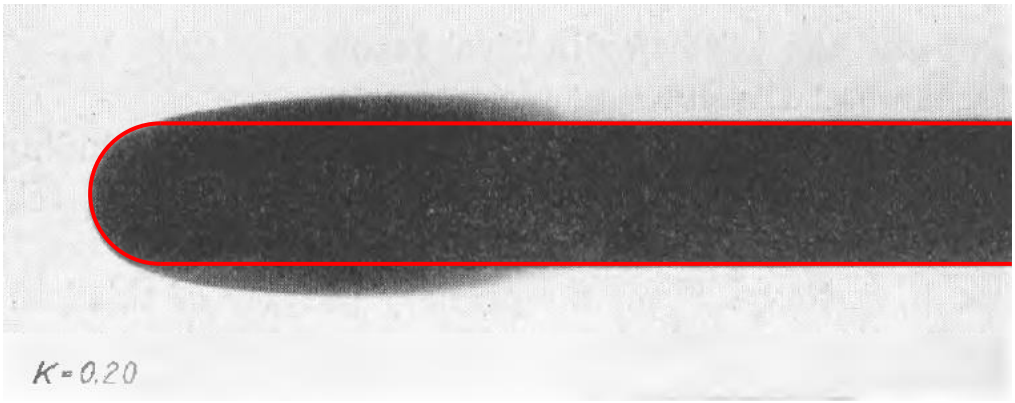

Figure 6-1: Image of cavitation experiment with the head shape geometry (red outline) for cavitation number $\sigma = 0.20$ (σ is denoted by K in the picture), the flow in the picture is from left to right

The boundary conditions are implemented as non-reflecting boundaries, as described in chapter 4.2.1. At the inlet the velocity is prescribed and at the outlet the pressure is prescribed. The red line in figure 6-2 signifies the inlet surface and that the blue line signifies the outlet surface. The green line signifies the wall of the head shape and will be treated as a no-slip wall in the CFD simulations.

From the work of Rouse & McNown [9] it is known that the experiments were performed using water at a Reynolds number, $Re = \frac{U \cdot d}{\nu}$, of 210,000. Using the Reynolds number and fluid properties of water, taking the characteristic length equal to two times the radius of the head shape ($d = 2r$), a inlet velocity of 8.2966 m/s was obtained for water. The inlet velocity for butane and propane is equal to the inlet velocity of water, being 8.2966 m/s. The inlet velocities are not scaled with the Reynolds number because it is assumed that, when different fluids are flowing through an identical pump, the flow rate through the pump is kept the same in accordance with an operating point specified by the manufacturer. Thus the resulting (higher) Reynolds number for butane is equal to 733,800 and the resulting (higher) Reynolds number for propane is equal to 1,030,000. The outlet pressure of each simulation is based on the cavitation number chosen for the simulation. The results obtained for a hemispherical head shape ($r = d/2$) by Rouse & McNown are shown in figure 6-4. The experiments by Rouse & McNown were performed over a wide range of cavitation numbers, from barely visible cavitation at $\sigma = 0.7$ till a cavitation length of several head diameters at $\sigma = 0.2$ (figure 6-1). For the purpose of this validation the cavitation numbers $\sigma = 0.3$, $\sigma = 0.4$ and $\sigma = 0.5$ from the experiments of Rouse & McNown are chosen. Choosing a higher cavitation number will result in a cavitation region that covers only a few cells, making the

mesh to coarse to properly capture that level of cavitation. Choosing a lower cavitation number will produce amounts of cavitation that will further impede the convergence of the solver as will be discussed later in this chapter.

For a given cavitation number ($\sigma = 0.5$) and saturated liquid density, ρ_l, saturation pressure, p_{sat}, and free stream velocity, v_∞, the outlet pressure of the domain can be calculated using the definition of the cavitation number given by equation 2-7. The free stream velocity is taken equal to the inlet velocity that was calculated using the Reynolds number. The values for E_k and ω are calculated using the formulas presented in chapter 4.3.3, respectively equation 4-87 and 4-88. A value of 1% is assumed for the intensity, I, of the turbulence. The choice to assume a value of 100 for the turbulent viscosity ratio, β, when considering external flow is extremely high. Generally the values for turbulent external flow are at least 10 times smaller than the current assumed value of 100. The motivation behind this choice and the influence of the turbulent viscosity ratio on the cavitation development are discussed later in this chapter.

The Venkatakrishnan-limiter contains a tunable parameter K that has to be set in order to limit the solution without influencing the final answer. After a process of trial and error the parameter K was set to a value of 5 to obtain the best results in the 2D cavitating nozzle. Note that for the 1D situation the value of K was equal to 0.3. At this point it is not clear if this difference is caused by the switch from 1D to 2D or switching from an internal geometry to an external geometry. Regardless, there is no clear procedure to determine K or estimate what the value will be based on known situations.

To prevent confusion, the output of all 5 scenarios: water for $\sigma = 0.5$, water for $\sigma = 0.4$, water for $\sigma = 0.3$, butane for $\sigma = 0.3$, and propane for $\sigma = 0.3$, is printed at the end of this chapter, figure 6-5 through 6-24. For the scenarios involving water, the pressure coefficient from the CFD simulation is compared with the experimental data of Rouse & McNown [9], presented in a similar way to figure 6-4. For the scenarios involving butane and propane, only the pressure coefficient from the CFD simulation is shown, since it cannot be compared with experimental data. Also the pressure, velocity and void fraction fields are shown for the solution of each scenario.

The conclusions that can be drawn from the results are split into two parts, one part commenting on the simulations with water, that are also used for the qualitative validation (chapter 6.3) and a second part commenting on the simulations with butane and propane (chapter 6.4). The reason that the simulations using butane and propane are split from the simulation using water, is that the simulations for butane and propane are predictions based on the current model. No validation data has been found on the exact pressure distribution for any liquid other than water.

6.2 Fluid properties used in the simulations

To avoid ambiguity surrounding the fluid properties, table 6-1 provides an full overview of all the fluid properties used. All three fluids are evaluated at a temperature of $293K$, using the Fluidprop [5] software that relies on the Refprop [60] library for butane and propane and relies on the IF97-library [61] for the properties of water. The constants and coefficients used for the equations of state are fitted according to the methods described in chapter 3.4. Near the end of the table all the inlet and outlet boundary conditions can be found, as calculated

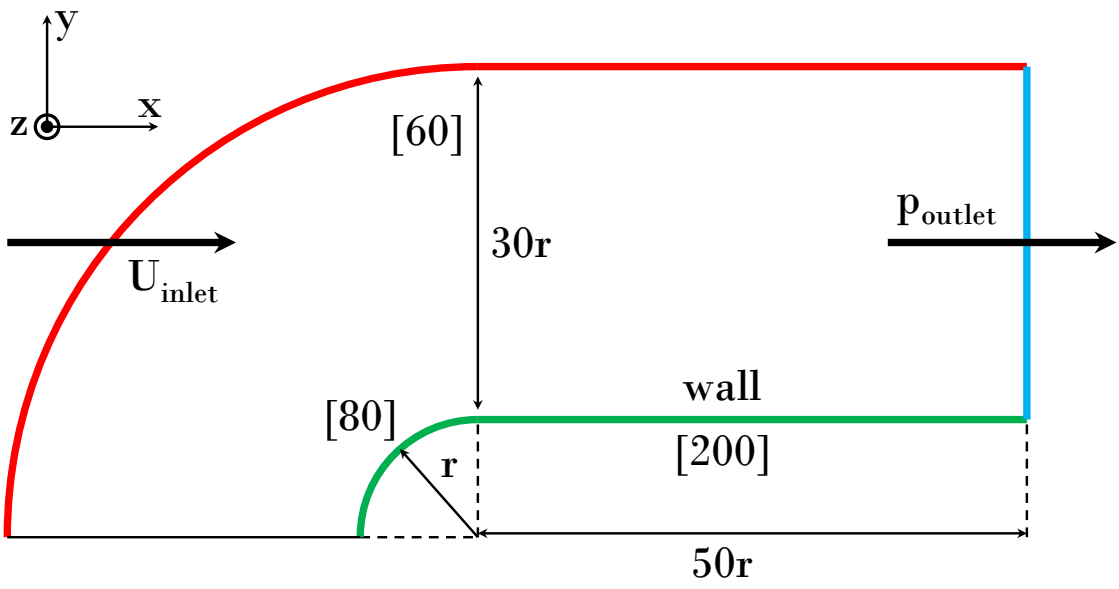

Figure 6-2: Head shape geometry, the rod has a radius r which is also the radius of the hemispherical head

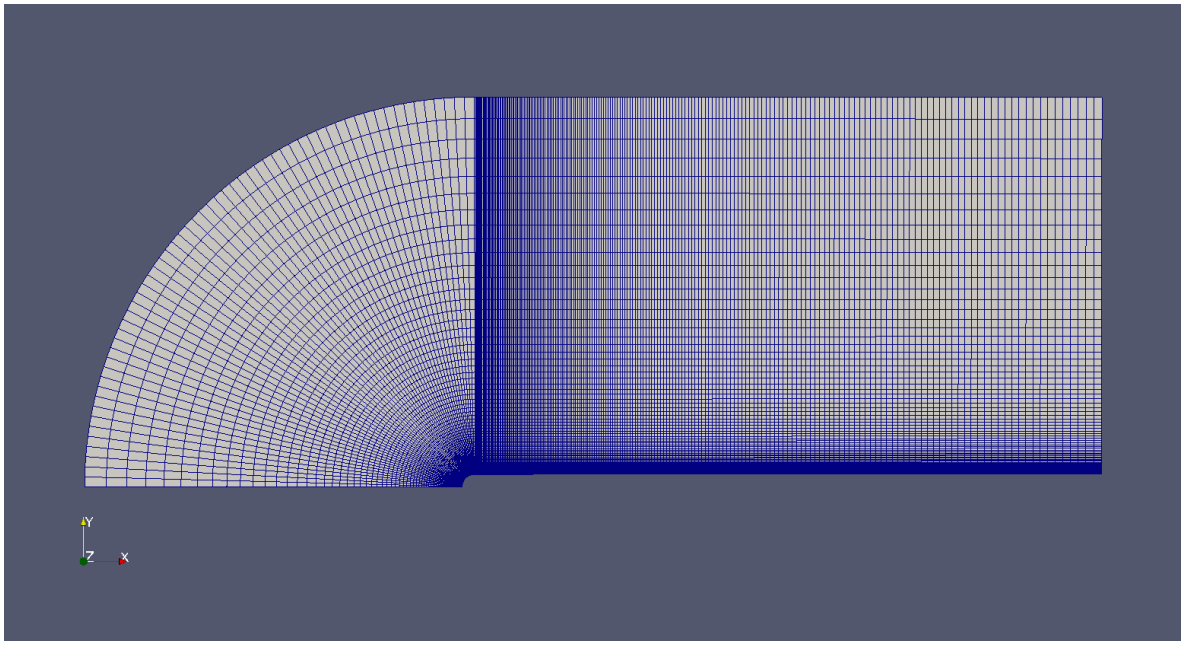

Figure 6-3: Mesh for the 2D model

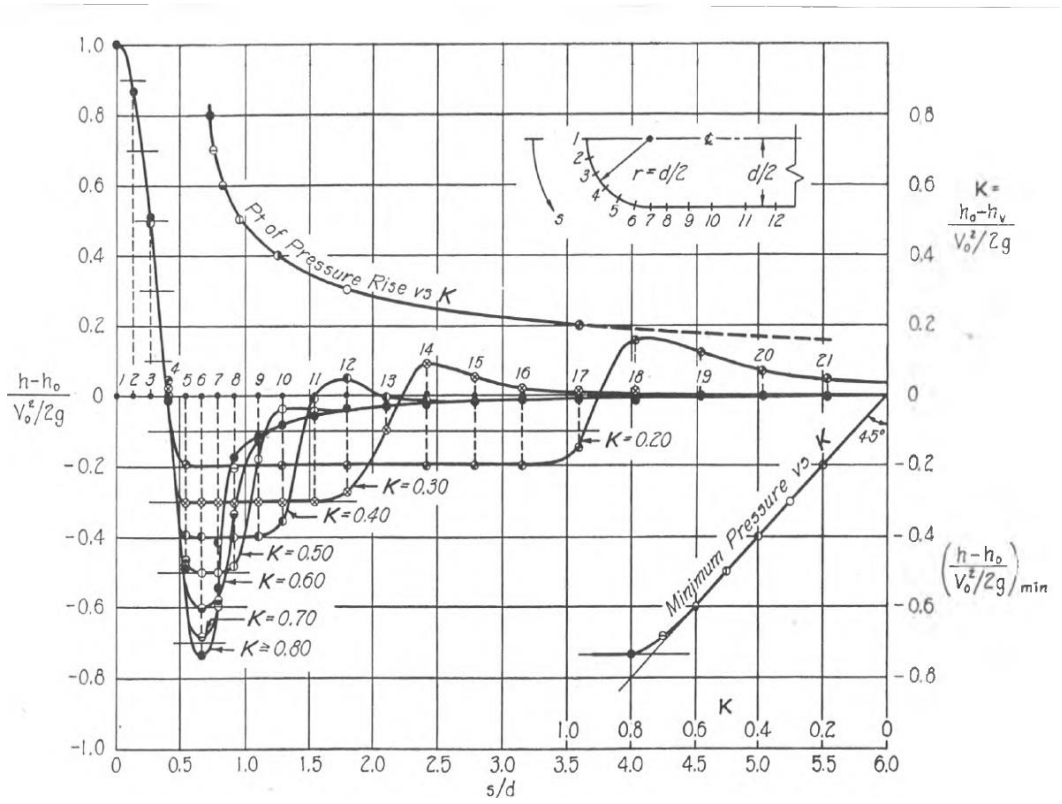

Figure 6-4: Pressure coefficient as a function of dimensionless edge length, for various cavitation numbers, ranging from $\sigma \geq 0.8$ till $\sigma = 0.2$ (σ is denoted by K in the picture); taken from Rouse & McNown [9]

using the cavitation number and Reynolds number to scale the outlet pressures and calculate the inlet velocity for each fluid. At the bottom of the table the boundary conditions for the turbulence model are presented.

6.3 Cavitation over a caliber headshape: water

The result of the quantitative results as shown in figure 6-5 through 6-7 and figure 6-10 through 6-18 are open for mixed interpretation. In general the model shows cavitation developing at the right location with a shape and size that are very comparable to the experiments of Rouse & McNown [9] (figure 6-1). On the other hand the oscillations in the pressure field never seem to fully disappear, stalling the convergence towards a stable cavitation region and a smooth pressure profile.

The cavitation lengths founds for $\sigma = 0.5$, $\sigma = 0.4$ and $\sigma = 0.3$ are 10.5 mm, 17.3 mm and 30.4 mm respectively. Note that the cavitation length is defined by the section of the head shape where the void fraction (at the surface) is above a certain arbitrary threshold, as discussed in chapter 5.4. For the determination of the previously mentioned cavitation lengths, this void fraction threshold was set at 10% ($\alpha > 0.10$). The sudden closure of the cavitation region, as observed in the 1D simulations, is also found in the 2D simulation. Note that the pressure is not fully representative for the cavitation region. For example in figure 6-7, the cavitation region is closed at $s/d = 1.8$ looking at the void fraction, while the pressure is slightly lagging behind, remaining below the vapor pressure until $s/d = 2.0$.

Comparing the pressure profiles from the CFD simulation with the experiments from Rouse & McNown [9] it is clear that the isenthalpic approach can be considered a satisfactory approach for modeling cavitation. The pressure profiles do not match perfectly with the measurements done by Rouse & McNown, which is likely caused by the relatively coarse grid. Also the fact that interactions between some of the sub-models and the local void fraction are not yet taken into account, is influencing the accuracy. For instance, the turbulence models or the viscosity of the liquid-vapor mixture. The general accuracy of the pressure profiles shown in figures 6-5, 6-6, and 6-7, is surprisingly high when considering that the mesh is relatively coarse. In each of the three cases involving water as the working fluid, the solver completed somewhere between 1 and 2 million time steps before the pressure field stabilized sufficiently to extract a relatively smooth and accurate pressure profile. As stated previously, the high amount of time steps requires that the cell count of the mesh is kept as low as possible in order to keep the total calculation time within a practicable range.

In figures 6-12, 6-15, and 6-18, it can be observed that the pressure field is not perfectly stable, especially near the start and closure regions of the cavitation. Also for water the liquid-vapor density ratio is the largest, meaning that numerically very big steps are made when vapor is formed or when the cavity is closed. Since density and pressure are coupled per definition through the barotropic model, any large step in density that is not fully resolved by the numerics of the solver, will result in local pressure oscillations. Barotropic modeling also implies that the lowest obtained density corresponds with the lowest obtained pressure. Due to the asymptotic behavior of the isenthalpic equation of state (figure 3-6) it is generally unlikely that the lowest density obtained in the domain is equal to the vapor density of the working fluid. For example, the lowest density obtained for water in the simulations is equal

Table 6-1: Overview of all parameters, coefficients and constants as used in the 2D cases

fluid name	water	butane	propane	unit
library	IF97	RefProp, butane	RefProp, propane	-
temperature - T	293.15	293.15	293.15	K
density - liquid - ρ_l	998.1608	578.5912	500.0569	kg/m^3
density - vapor - ρ_v	0.0173	5.3126	18.0823	kg/m^3
ratio	57655	109	28	-
dynamic viscosity - liquid - μ_l	$1.0016 \cdot 10^{-3}$	$1.6615 \cdot 10^{-4}$	$1.0229 \cdot 10^{-4}$	$Pa \cdot s$
kinematic viscosity - liquid - ν_l	$1.0035 \cdot 10^{-6}$	$2.8717 \cdot 10^{-7}$	$2.0455 \cdot 10^{-7}$	m^2/s
dynamic viscosity - vapor - μ_v	$9.7272 \cdot 10^{-6}$	$7.2617 \cdot 10^{-6}$	$8.0891 \cdot 10^{-6}$	$Pa \cdot s$
kinematic viscosity - vapor - ν_v	$5.6186 \cdot 10^{-4}$	$1.3669 \cdot 10^{-6}$	$4.4735 \cdot 10^{-7}$	m^2/s
saturation pressure - p_{sat}	$2.3392 \cdot 10^{3}$	$2.0765 \cdot 10^{5}$	$8.3646 \cdot 10^{5}$	Pa
critical pressure - p_{crit}	$2.2064 \cdot 10^{7}$	$3.7960 \cdot 10^{6}$	$4.2512 \cdot 10^{6}$	Pa
Tait equation - K_0	$3.6904 \cdot 10^{8}$	$4.7779 \cdot 10^{7}$	$2.5835 \cdot 10^{7}$	Pa
Tait equation - N	5.9496	10.4209	10.9740	-
CEV model - coefficient a	0.01262	0.01726	0.01747	-
CEV model - coefficient b	-0.6014	-0.5168	-0.5136	-
CEV model - coefficient c	0.8241	1.4654	1.2094	-
CEV model - parameter gV	0.887	0.9424	0.9084	-
Reynolds number - Re	210000	210000	210000	-
hydraulic diameter - d_h	0.0254	0.0254	0.0254	m
cavitation number	0.5	0.5	0.5	-
inlet velocity	8.2966	2.3742	1.6912	m/s
outlet pressure	19516.0	208465.2	836818.5	Pa
Turbulent intensity - I	0.010	0.010	0.010	-
Turbulent viscosity ratio - β	100.0	100.0	100.0	-
kinetic energy - E_k	$1.0325 \cdot 10^{-2}$	$8.4552 \cdot 10^{-4}$	$4.2902 \cdot 10^{-4}$	J
specific turbulence dissipation - ω	102.891	29.444	20.974	$1/s$

to $4.41 kg/m^3$ (or $\alpha = 0.9956$), which is still 260 times larger than the saturated vapor density of $0.017 kg/m3$ at $293K$.

The velocity field clearly indicates the complexity of the closure region of the cavitation, as seen in figures 6-11, 6-14 and 6-17. The flow locally becomes stationary, raising the local pressure, which will eventually suppress the formation of cavitation. A more detailed analysis of the flow field revealed that the x-component of the velocity field can become negative in the closure region, suggesting some kind of recirculation in the wake of the cavitation zone. Various authors, like Senocak and Shyy [64] and Bouziad [16], provide background on the complex flow fields that form in the closure region. The fact that the recirculation in the cavitation zone is also observed in the current model strengthens the fact that the model is providing a physically accurate representation of cavitation. Do note, that with the choice of barotropic modeling it is automatically assumed that the flows cannot contain any baroclinical component. Gopalan and Katz [37] show in their work that baroclinical torque can play a very prominent role in the correct modeling of the closure region. Thus barotropic modeling may not be the preferred choice if a large interest is taken in the detailed modeling of the closure region.

6.4 Cavitation over a caliber headshape: butane and propane

Before discussing the differences between water, butane, and propane, which are only compared for $\sigma = 0.3$, it is again stressed the simulations for butane and propane are predictions based on the current model, thus are unvalidated at this time.

The biggest difference in the cavitation development of water, butane and propane is found in the size of the cavitation region and the maximum void fraction obtained in this region. The cavitation length of water is 30.4 mm, while the cavitation length of butane is only 9.9 mm (counting only the first vapor pocket) and the cavitation length of propane is a mere 8.8 mm. Also the maximum void fraction obtained by water is in the order of 99%, coming relatively close to the density of the pure vapor phase. Butane reaches a maximum void fraction of 45% and propane reaches a maximum void fraction of 12%. Since the current model assumes a homogeneous mixture of the two phases, one could state the lower void fraction translates to less or smaller bubbles occupying the zone in which cavitation is taking place. It is hypothesized that the cavitation zones of butane and propane are more like a bubbly mixture of the two phases, while the cavitation zone of water is almost a pure pocket of vapor.

The 2D results are quite comparable with the 1D results as discussed in chapter 5. The influence of the liquid-vapor density ratio as discussed in chapter 5.4 is again seen in the 2D results. For example pressure profile for water (figure 6-7) is almost flat in the region that is cavitating, staying relatively close the saturation pressure. Propane and butane (figure 6-8 and 6-22) go well below the saturation pressure in the cavitating region, resulting in pressure profiles that are quite similar to pressure profiles in figure 5-7 and figure 5-10. The velocity fields on the other hand are completely different when comparing the 1D scenario (figure 5-4) with the 2D scenario (figure 6-17). As was already stated in chapter 5.4, one dimension is simply not enough to capture the complex flow patterns and circulation that occur in the closure region of the cavitation zone.

The velocity fields of butane and propane, when compared with water, are very similar in magnitude and are only slightly influenced by the changes in fluid properties. The general magnitude of the velocity field hardly changes. The recirculation in the closure region, as seen with water (figure 6-17), is not found back in the velocity fields of butane (figure 6-20) and propane (figure 6-23). The pressure field varies significantly between each of the fluids, in which the ratio between the free stream pressure and the saturation pressure plays an important role. For water the free stream pressure is in the order of 0.1-0.2 bar and the saturation pressure of water is 0.023339 bar, meaning that the free stream pressure is several times the value of the saturation pressure. For propane the free stream pressure is almost equal to the saturation pressure. The balance of the pressure forces is much more delicate in propane, a good initial field has to be provided to prevent large parts of the domain turning into vapor, which will destabilize the entire solution. Although the spurious pressure oscillations for water are much more intense due to the large pressure and liquid-vapor density ratios, the general solution tends to be more stable than the solution of propane, that cannot cope with a badly formulated initial guess.

The fact that it is very hard to develop a method that numerically treats every fluid equally, has also been noted in the previous chapter (chapter 5.4). The results for butane for $\sigma = 0.3$, as shown in figure 6-19 through 6-21, shows the consequence of choosing a single setting for the numerics of the solver. The cavitation zone stops abruptly at $s/d = 0.9$ and reforms itself at $s/d = 1.15$, resulting in very strange gap in between two separated parts of cavitation. The value of K in Venkatakrishnan's limiters is not adjusted individually for each fluid. The choice for $K = 5$ is based on the performance of the solver using water as the working fluid. A possible explanation for the gap found in the cavitation zone of butane could be that Venkatakrishnan's limiter is only triggered in a small section of the cavitation region, resulting in the gap that can be clearly observed in figure 6-19.

When the damage caused by cavitation needs to be predicted, water is used for the CFD simulations even when the actual working fluid is a hydrocarbon like butane or propane. The reasoning behind this method is that water, for a similar situation, will always cavitate more and will collapse with more energy. Thus predicting cavitation damage with water will result in a 'worst case' scenario. If the design is correctly adjusted so that the cavitation damage is within the required bounds, assuming water as the working fluid in the CFD calculations, the actual working fluid (some hydrocarbon) will never be able to cause more damage than the scenario based on water. A similar strategy could be applied to head drop curves, but when comparing figures 6-7, 6-19, and 6-22, it becomes clear that water cannot always be taken as the reference for the 'worst case' scenario, assuming that the head lost due to cavitation is always less than the head drop predicted with water as the working fluid. This is the main reason for developing this model. In order to predict head drop curves, and 'NPSH3' curves by extension, the shape and size of the cavitation region has to be predicted using the same fluid properties as the working fluid that will be used in the field. Calculating 'NPSH3' curves for hydrocarbons, but still basing the calculation on water, is simply not sufficient.

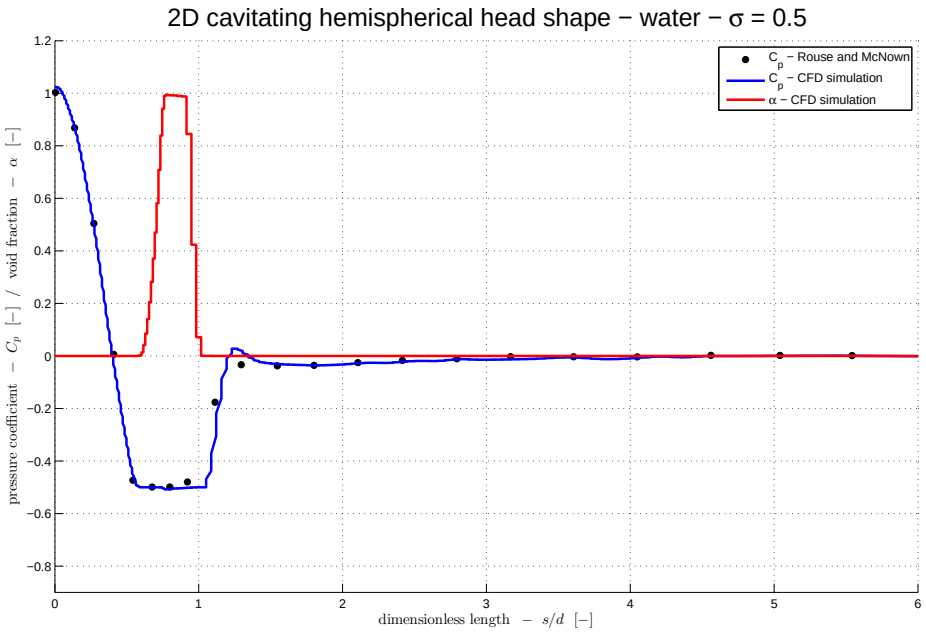

Figure 6-5: 2D cavitating head shape - water - $\sigma = 0.5$, plot of pressure coefficent as a function of dimensionless edge length, comparing the CFD simulation with data from Rouse & McNown [9]

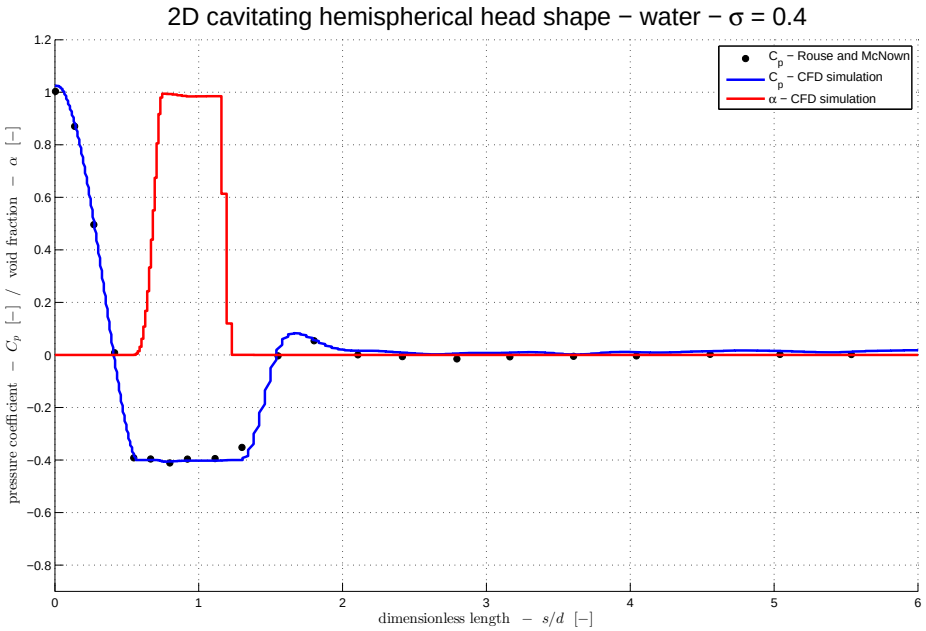

Figure 6-6: 2D cavitating head shape - water - $\sigma = 0.4$, plot of pressure coefficent as a function of dimensionless edge length, comparing the CFD simulation with data from Rouse & McNown [9]

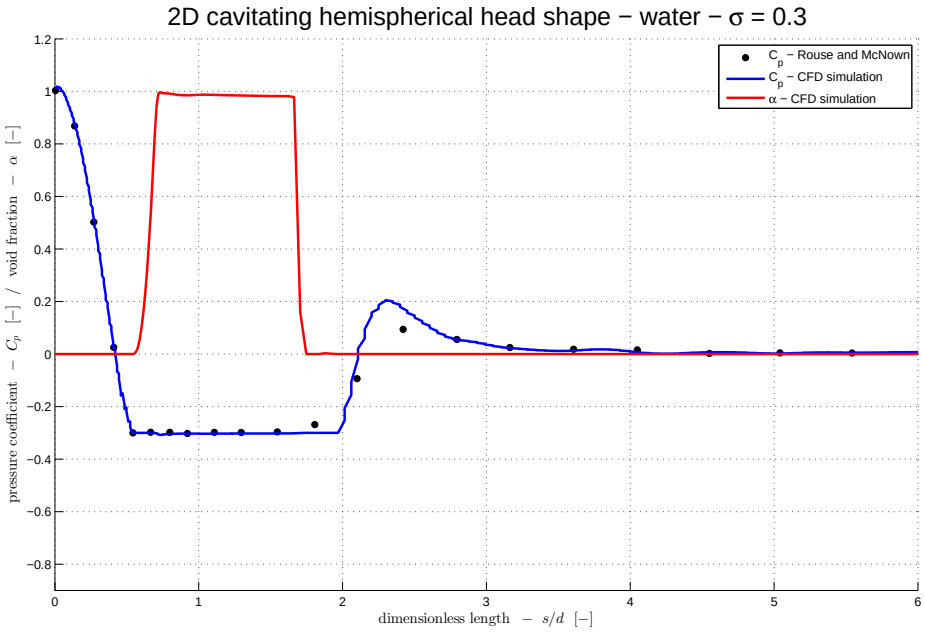

Figure 6-7: 2D cavitating head shape - water - $\sigma = 0.3$, plot of pressure coefficent as a function of dimensionless edge length,comparing the CFD simulation with data from Rouse & McNown [9]

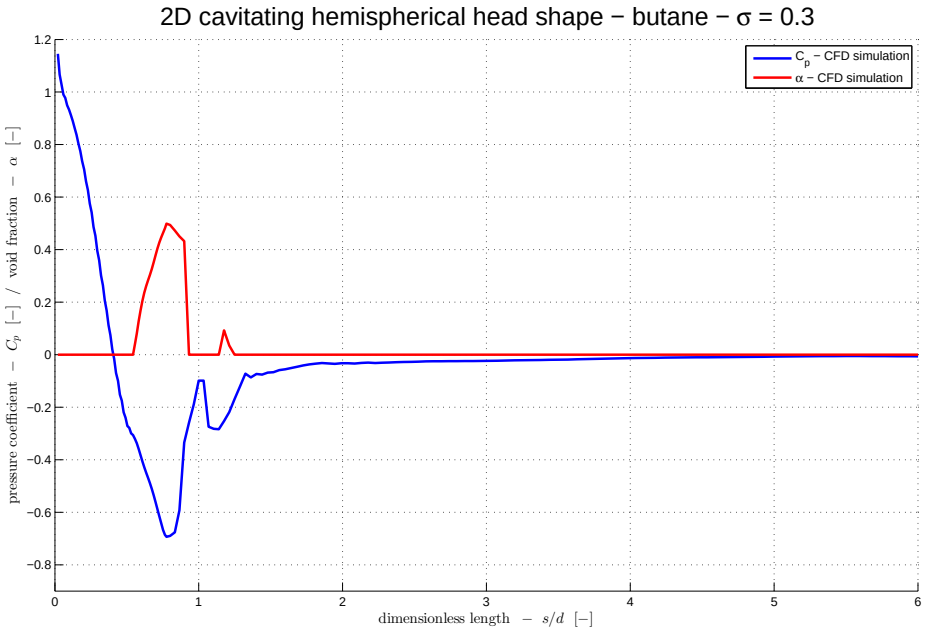

Figure 6-8: 2D cavitating head shape - butane - $\sigma = 0.3$, plot of pressure coefficent as a function of dimensionless edge length, CFD results only

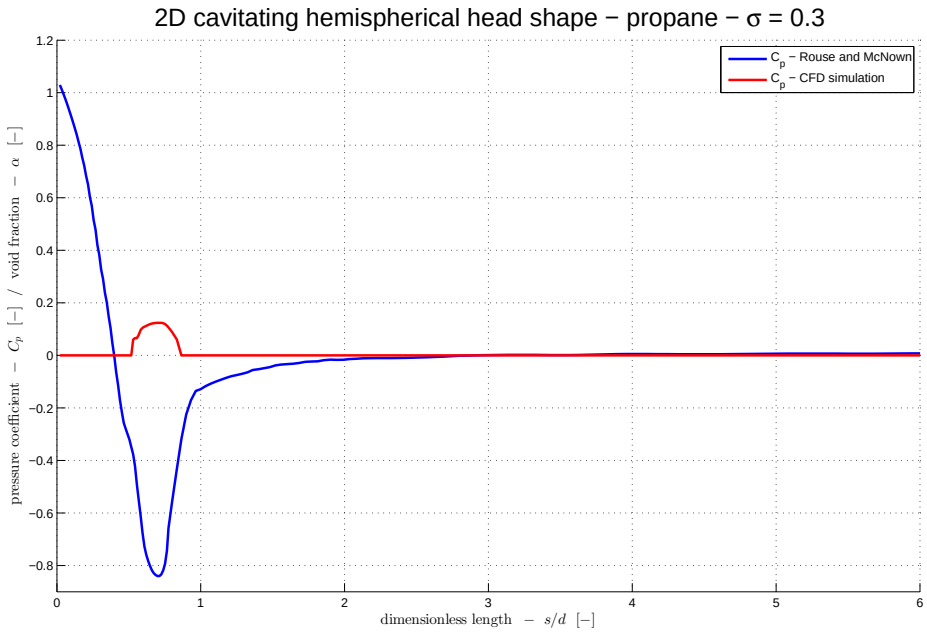

Figure 6-9: 2D cavitating head shape - propane - $\sigma = 0.3$, plot of pressure coefficent as a function of dimensionless edge length, CFD results only

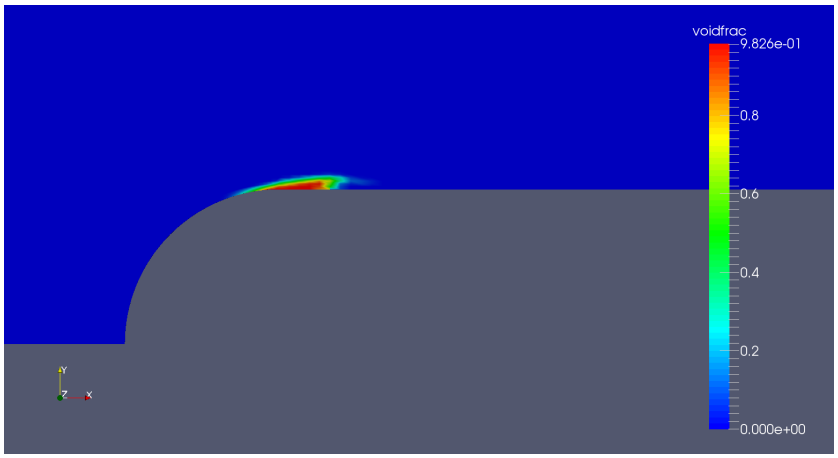

Figure 6-10: 2D cavitating head shape - water - $\sigma = 0.5$, plot of void fraction field

Figure 6-11: 2D cavitating head shape - water - $\sigma = 0.5$, plot of velocity field

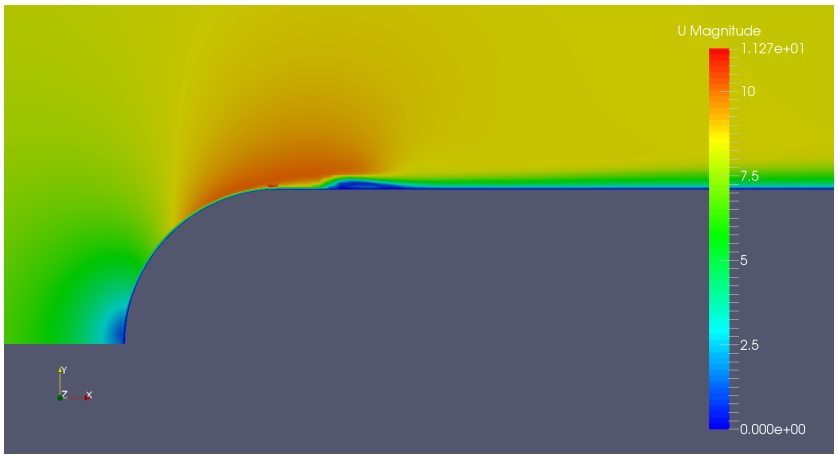

Figure 6-12: 2D cavitating head shape - water - $\sigma = 0.5$, plot of pressure field

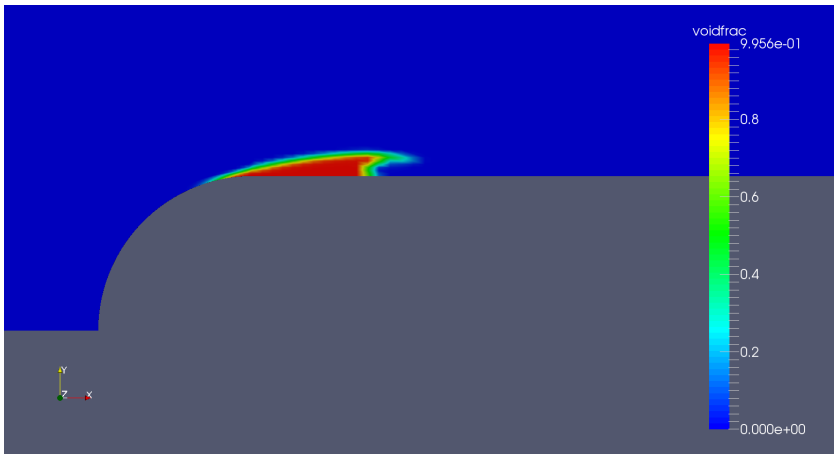

Figure 6-13: 2D cavitating head shape - water - $\sigma = 0.4$, plot of void fraction field

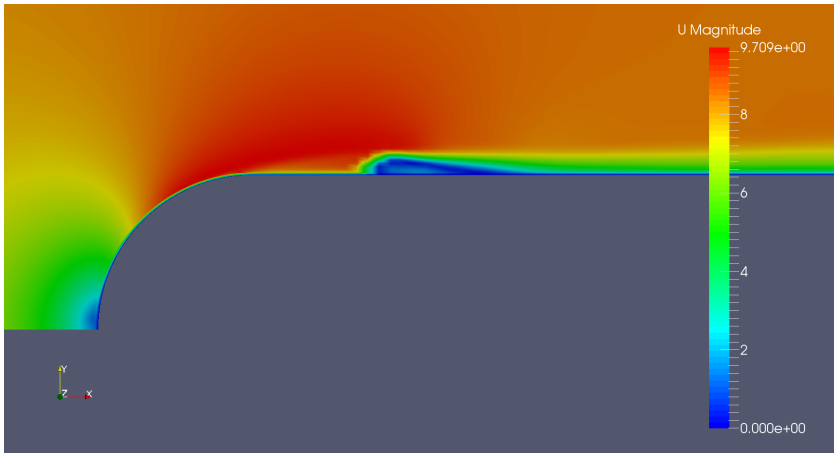

Figure 6-14: 2D cavitating head shape - water - $\sigma = 0.4$, plot of velocity field

Figure 6-15: 2D cavitating head shape - water - $\sigma = 0.4$, plot of pressure field

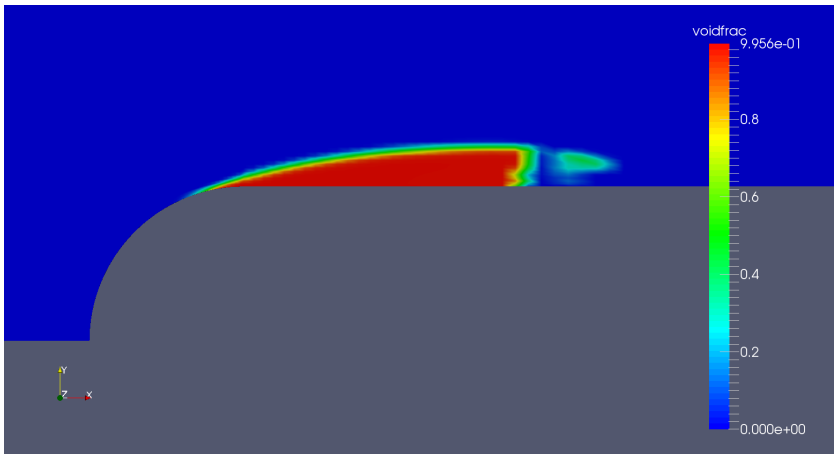

Figure 6-16: 2D cavitating head shape - water - $\sigma = 0.3$, plot of void fraction field

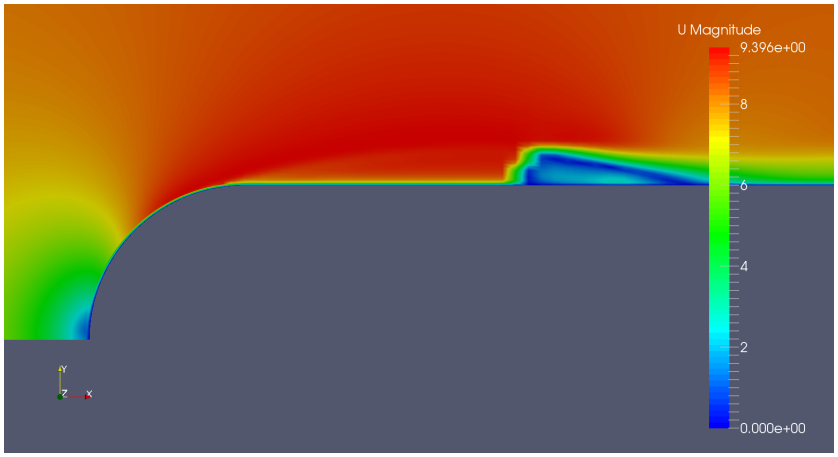

Figure 6-17: 2D cavitating head shape - water - $\sigma = 0.3$, plot of velocity field

Figure 6-18: 2D cavitating head shape - water - $\sigma = 0.3$, plot of pressure field

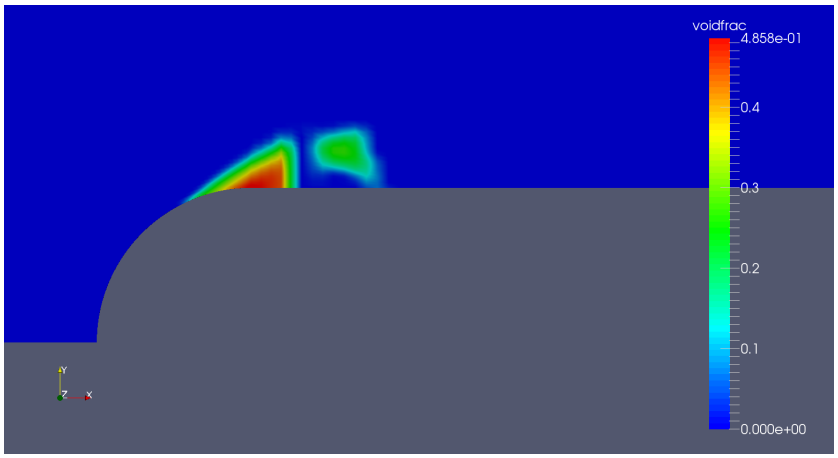

Figure 6-19: 2D cavitating head shape - butane - $\sigma = 0.3$, plot of void fraction field

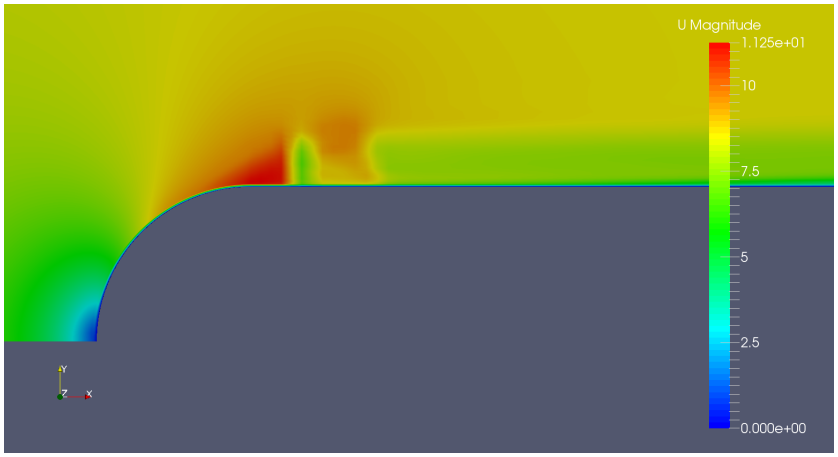

Figure 6-20: 2D cavitating head shape - butane - $\sigma = 0.3$, plot of velocity field

Figure 6-21: 2D cavitating head shape - butane - $\sigma = 0.3$, plot of pressure field

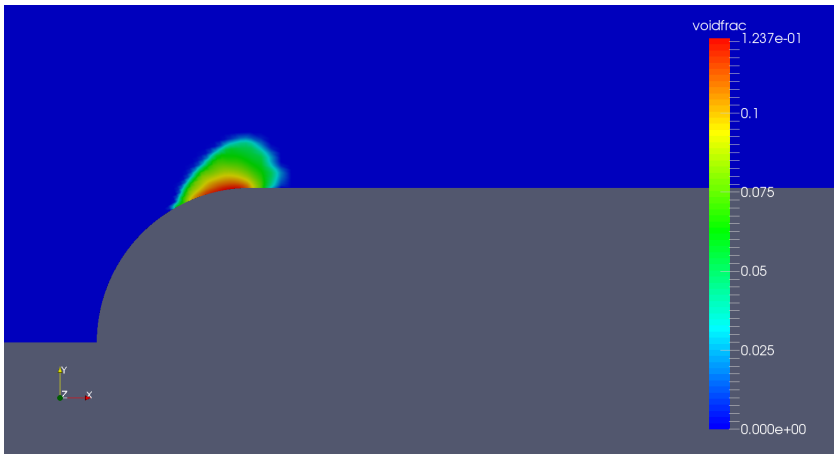

Figure 6-22: 2D cavitating head shape - propane - $\sigma = 0.3$, plot of void fraction field

Figure 6-23: 2D cavitating head shape - propane - $\sigma = 0.3$, plot of velocity field

Figure 6-24: 2D cavitating head shape - propane - $\sigma = 0.3$, plot of pressure field

Chapter 7

Discussion and review

The purpose of this chapter is to discuss and review the results obtained with the 1D models and 2D models, pointing out key observations derived from the results. This is followed by a discussion of possible application of the model. The chapter is concluded by identifying the current limits of the model and suggesting possible recommendations for future work on the subject.

7.1 Discussion of 1D results

In general it can be concluded that the main goals as stated in the introduction (chapter 1.2) have been achieved, as was the intention in order to consider the final result a successful approach in modeling cavitation. The construction of a barotropic isenthalpic model was successful and the resulting model was validated using thermodynamic data. The cavitation development of water, butane and propane was demonstrated in the 1D implementation and all the input needed by the model consisted of fluid properties or fitting functions taken from fluid properties. The goal to have no empirical relations inside the model has been fully achieved, providing the possibility to model cavitation for any fluid as long as sufficient thermodynamic data is available. From the beginning it was known that the assumption to evaluate all fluid properties at free-stream temperature may not be valid for each fluid, since the thermal properties of each fluid are different, causing the fluid to be more susceptible to local changes in temperature. After analyzing the local thermodynamics of cavitation, the thermal susceptibility of each fluid was evaluated using Brennen's thermal parameter. The conclusion is that, although butane and propane are considered to be more susceptible to local temperature changes than water, the barotropic model is not significantly influenced by the assumption to evaluate at free-stream temperature. The actual influence of updating the temperature dependent fluid properties on the barotropic relation is low enough to consider it a second-order effect.

The numerics involved with the accurate description of cavitation are equally important compared to the physical modeling of cavitation and may be even considered more difficult

when modeling the fluids as fully compressible. The main challenge lies in the fact that two extremes need to be combined in the same solver and interact in a stable manner. On one side the vapor has a low density and is also very compressible, on the other side the liquid has a high density and is weakly compressible at best. When the fluid starts to cavitate the solver needs to facilitate a crossing from the (almost) incompressible liquid to the fully compressible vapor, while maintaining conservation for mass and momentum.

It has been repeatedly shown in this thesis that the ratio between the liquid density and the vapor density is not only a property of the fluid and thus influences the barotropic behavior, but also plays a very large role in the overall stability of the numerics. The bigger the ratio is between the liquid and the vapor density, the more aggressive the behavior of the numerics become to keep the solution stable. Larger vapor liquid density ratios are more difficult to handle in obtaining a stable solution and many of the numerical issues found in the current method are more present at these higher ratios. Interestingly enough, water is almost always the fluid of interest in cavitation research and hardly considered to be 'exotic' from the perspective of process liquids. But the fact that the density drops by a factor of 57655, makes cold water one of the hardest fluids to describe. If a compressible solver can accurately handle the cavitation development of water with the full jump in density, it should have no difficulties with butane or propane that have liquid to vapor density ratios several orders of magnitude lower than water.

7.2 Discussion of 2D results

The transition from 1D to 2D proved to be much more difficult than expected. For reasons not yet fully understood, the model becomes much more sensitive and unstable for calculations in 2-dimensional domains. One of the main issues with the current method is the amount of parameters that can be changed to influence the numerics. Venkatakrishnan's limiters has a parameter K that determines the threshold that needs to be crossed before the limiter will act. The compressible solver also needs a very small time step in order to keep the solution stable. OpenFOAM has a library containing many different discretization schemes to calculate local derivatives and laplacians, this is another uncertainty that can be manipulated and will influence the overall numerical behavior of the solver. Taking all these variables into account, it is likely that the ideal stable setting for the solver is an optimization of the previously mentioned parameters. But due to long calculation times, it is practically unworkable to go through these combinations of parameters in a process of trial and error.

Also the influence of the turbulence models, although not discussed in great detail in the current work, are important for capturing the correct shape of the cavitation zone. The viscosity that is added locally by the RANS-type turbulence models is needed to force the cavitation region into a stable shape. When generally accepted values are chosen for the turbulent viscosity ratio, β, which should be in the order of 1 to 5 for external flow or 10 at most for very turbulent external flows, resulted in unstable cavitation that fluttered away from the wall in a unphysical way. By increasing the turbulent viscosity ratio β to 100, which is closer to values found in extremely turbulent pipe flow, the cavitation region became stable and fixed, with a clear starting point and a clear closure point as is to be expected for attached or sheet cavitation.

Granted that the model does not yet perform as expected, needing measures like the extreme turbulence to close the cavitation region, it did show promising results. The general shape of the cavitation region for water looked very similar to pictures taken by Rouse & McNown. Even the cavitation length and pressure profile are predicted quite well by the model, which offers possibilities for practical applications of the model. The mesh used in the calculation is relatively rough, containing only 16,800 cells to span a relatively large domain, but the accuracy shown in the calculation of the pressure profile (figure 6-5 through 6-9) is more than adequate. This confirms that the model is able to capture the cavitation development of water, even on a relatively coarse grid. The predictions for butane and propane, though hard to judge without reference material, looked plausible. The model took the different fluid properties into account and showed differences in cavitation development that are very similar to the differences observed between the fluids in the 1D implementation. The numerics are the biggest downfall of the model in its current state and need much more attention than received in this thesis.

7.3 Application possibilities of the model

The longterm goal of the model developed in this thesis is to apply it to actual engineering problems when considering pump performance and lifetime. The current version of the model is likely too inefficient to be of any practical use, meaning that the model would simply take too much time for a practical grid (1M cells) during a short simulation of $0.2s$ (10 revolutions of a pump driven at $50Hz$). Although the current version of the model is not fully ready for practical day-to-day use, an overview of possible future applications is presented to emphasize the model's strengths.

Correct prediction of the cavity length can be very interesting due to damage models used by Flowserve according to the book of Gülich [65]. According to Gülich the erosion rate for attached or sheet cavitation, ϕ_c, in $[mm/h]$ scales with the cavitation length:

$$\phi_c \quad \propto \quad \left(\frac{L_{cav}}{L_{cav,10}} \right)^N \tag{7-1}$$

In this equation $L_{cav,10}$ is the reference cavitation length of $10mm$ as used by Gülich in the experiments to calibrate the model. Coefficient N is equal to 2.83 for cavitation on the suction side of the impeller blade and equal to 2.60 for cavitation on the pressure side of the impeller blade. Also the paper by Schiavello & Visser [66] emphasizes that this relation can be very useful in predicting long term damage based on visual assessment of cavitation. If this visual assessment is obtained from actual experiment using a test loop or taken from a good quality CFD simulation should not matter. In the past good results have been obtained predicting cavitation damage based on cavitation lengths taken from CFD simulations.

Due to the barotropic modeling of the cavitation, it is mandatory for the pressure to go below saturation pressure in order to reach lower densities. In some other cavitation models, like in the cavitation model of Koop [26] the pressure is cut off at saturation pressure, meaning that the cavitation zone itself is at a constant pressure equal to the saturation pressure and cannot go below saturation pressure. In order to predict the energy that is released when a cavitation bubble implodes, an accurate description of the pressure inside the cavitation zone

is required. The barotropic model cannot only describe the shape and length of the cavity but could also be used to estimate the energy that is released by the cavitation bubble when it implodes.

The last possible application is the calculation of head drop curves in order to specify quantities like 'NPSH3' (NPSH required at the point where the pump loses 3% head). Previously this was a task performed by CFX-Tascflow and since one of the main goals of this thesis project is to develop a model that can fill the position left by Tascflow, it is only logical that at some point this model will be used to calculate head drop curves. However, a lot of additions and modifications are required before this model is ready to be used in combination with centrifugal pumps. For example, the model is only tested for stationary grids in the current work, the rotating domain of an impeller is not yet supported.

7.4 Limitations the model

Due to choices made during the development of the current cavitation model, the model has certain limits in its performance and abilities to model the development of cavitation. The aim of this section is to inform a possible user about the limitations of the model. Do note that the analysis of these limitations is not equal to a recommendation to remove these shortcomings in future work. Most of these limitations are very fundamental in nature, meaning that these cannot be resolved by improving the current methods. To solve these shortcomings the overall model needs to be re-evaluated and key components of the model need to be rewritten. Chapter 7.5 provides actual recommendations for the model, which are deemed to be realizable using the current state of the model and solver as a starting point.

The current method to advance the problem in time is the explicit 4^{th} order Runge-Kutta scheme. The explicit nature of the scheme is closely tied to the CFL number, which per definition should not become larger than 1 for explicit schemes. If the solver is made with an implicit method instead of an explicit method, this should not only benefit the maximum time step that can be taken, but can also take away the conditional stability requirements of an explicit method. The main downside of an implicit method is that these methods rarely provide an analytical solution, thus needing some kind of a root-finding algorithm (for example Newton's method) to obtain a solution. This will be much more complex to program and will take more time to solve for each time step. However, it can be argued that the additional time needed to solve each time step is compensated by larger maximum time step that can be taken.

Although this model was developed with a fully compressible solver in mind, it is a fact that most commercial CFD suites use an incompressible solver and only a limited number of these suites have included a fully compressible solver. An interesting future project could be to take the foundation for an isenthalpic expansion from this thesis but make it suitable for an incompressible solver. One could for instance develop new source terms for equations 2-32 and 2-33 that adhere to the principle of an isenthalpic expansion. Another possibility would be to stay much closer to the original principle of the CEV model as illustrated by figure 3-1, requiring the full solution of mass, momentum and energy. The solution of the energy equation can then be combined with tabulated enthalpy data of the relevant fluid to obtain a description of the density field.

One of the main disadvantages of a barotropic model is that it implies that the model is independent of temperature. In chapter 3.2.5 it is discussed how the local temperature decrease (due to cavitation) influences the local fluid properties and suppresses the development of cavitation. The validation of the model for propane and butane, which are deemed thermally sensitive according to Brennen's parameter Σ (chapter 2.1.7), showed that the influence of adjusting the fluid properties to the local temperature is minimal. To fully close this gap, the barotropic model has to be abandoned in favor of a full equation of state like the Peng-Robinson-Stryjek-Vera or Redlich-Kwong equation of state. In order to include a full equation of state, replacing the current barotropic relation, the energy conservation equation (equation 4-15) needs to be brought back into the Euler equations. The cavitation model written by Koop [26] followed a very similar approach.

7.5 Future recommendations

The general outcome of this thesis is deemed satisfactory since a number of important steps are taken in the development of modeling cavitation as a isenthalpic barotropic fluid. But there is still much room for improvement (also see chapter 7.4). In the opinion of the author of this thesis the following points are interesting and relevant topics for future work.

In its current state the stability of the solver leaves a lot to be desired. Looking back at both the 1D validation and the 2D validation it is clear that the current numerical methods are not always stable and can struggle with convergence to a steady state. The 1D implementation showed that the numerical schemes, as they are currently implemented, can lead to stable solutions. But the observations made in chapter 5 showed that the numerics are influenced by both the fluid properties and the numerical parameter settings: for example, parameter K of Venkatakrishnan's limiter. In the 2D implementation the numerical issues are much more present and harder to overcome than in the 1D implementation. Especially the convergence of the pressure field is very slow (or stalls) and is extremely sensitive to external influences. The method has to be tuned for different geometries and a combination of parameters is required to obtain a stable solution. In the timespan of this thesis the author was not able to find an ideal combination for those parameters, leading to a very time consuming process of trial and error for each simulation. A good topic for future study would be a full numerical study of the current work, identifying sensitivities and stability limits for the current methods.

Much effort was taken to factor in the complex numerics associated with the description of cavitation. In the end, the main downfall of this model can be found in those numerics. One of the main differences between the incompressible cavitation models using the Rayleigh term (chapter 2.2.4) and the fully compressible cavitation model, as developed in this thesis, is that the mass transfer for the fully compressible model happens instantaneously. To counter this effect, one has no choice to introduce complex numerics to limit and stabilize the solution. A possible improvement could be to no longer assume instantaneous thermodynamic equilibrium, but allow for a certain 'relaxation time' to transfer from non-equilibrium to equilibrium. This will limit the mass transfer between phases and should reduce the need for advanced numerics to stabilize the solution. Both of these recommendations will lead to improved performance and more stable numerics when applying the current model and solver to future test cases involving different fluids.

Appendix A

Appendix A: 1D Matlab code

A.1 EulerSolver_1D_CEV.m (main application)

```
clear all
close all
clc

%data_WATER_10ms        % run on: 08-08
%data_WATER_9ms         % run on: 08-08
%data_WATER_8ms         % run on: 08-08
%data_BUTANE_10ms       % run on: 08-08
%data_BUTANE_9ms        % run on: 08-08
%data_BUTANE_8ms        % run on: 08-08
data_PROPANE_10ms      % run on: 09-08
%data_PROPANE_9ms       % run on: 09-08
%data_PROPANE_8ms       % run on: 09-08

%% fluidprop calls

Init_FluidProp

ErrorMsg = invoke(FP,'SetFluid_M',Model,nCmp,Cmp,Cnc)
FP.SetUnits('SI','','','')

psat = invoke(FP,'Pressure','Tq',Tinf,0);
pc = invoke(FP,'Pcrit');
rhol = invoke(FP,'Density','Tq',Tinf,0);
rhov = invoke(FP,'Density','Tq',Tinf,1);

% cl = invoke(FP,'SoundSpeed','Tq',Tinf,0);
% cv = invoke(FP,'SoundSpeed','Tq',Tinf,1);

%% grid setup - 2D grids possible but calc. will only span x-cells
```

```
31
32 tnx = nx + 2*gp;
33 tny = ny + 2*gp;
34
35 xstart = -1;
36 xend = 1;
37 ystart = 0;
38 yend = 1;
39
40 Lx = xend-xstart;
41 Ly = yend-ystart;
42
43 dx = Lx/nx;
44 dy = Ly/ny;
45
46 %     Definition of grid numbering
47 %       x=0               x=1
48 % grid   |---o---|---o---|---o---  ...  --|---o---|
49 %            1   1   2   2   3           nx-1  nx
50
51 if nx == 1
52     xc = 0.5*Lx;
53     yc = ystart+(dy.*(1:(ny+2*gp)) - (dy/2+(gp*dy)));
54 elseif ny ==1
55     xc = xstart+(dx.*(1:(nx+2*gp)) - (dx/2+(gp*dx)));
56     yc = 0.5*Ly;
57 else
58     xc = xstart+(dx.*(1:(nx+2*gp)) - (dx/2+(gp*dx)));
59     yc = ystart+(dy.*(1:(ny+2*gp)) - (dy/2+(gp*dy)));
60 end
61
62 xw = linspace(xstart,xend,nx+1);
63 yw = linspace(ystart,yend,ny+1);
64
65 if viewgrid == 1
66    gridplot(nx,ny,Lx,Ly,xw,yw,xc,yc);
67 end
68
69 %% setup matrices
70
71 [X,Y] = meshgrid(xc,yc);
72 X = X';
73 Y = Y';
74
75 F = zeros(tnx-1,2);
76 Ustar  = zeros(tnx,2);
77 U = zeros(tnx,2);
78 UL = zeros(tnx-1,2);
79 UR = zeros(tnx-1,2);
80
81 %% initialize matrices - according to init. cond. from Sod Shock tube
82
83 rho_init = ((((p_init-psat)/K0)+1)^(1/N))*rhol;
```

```
84
85 for i = 1:tnx
86 U(i,1) = rho_init;
87 U(i,2) = rho_init*u_init;
88 end
89
90 %% setup interpolation of Pcev
91
92 p_CEVinterp = linspace(psat,0.01*psat,2e3);
93 rho_CEVinterp = CEV_interp(p_CEVinterp,psat,pc,rhol,rhov,...
94                 CEV_a,CEV_b,CEV_c,CEV_gV);
95
96 %% time loop
97 t = 0;
98 count = 0;
99 rescount = 1;
100
101 wbstring = ['calculating: end time = ',num2str(tend),...
102             ' - grid cells = ',num2str(nx*ny)];
103 h = waitbar(0,wbstring);
104
105 makeplot
106 makeplot2
107
108 while t < tend
109
110   i = 2:tnx-1;
111   im1 = 1:tnx-2;
112
113   % initialize/update vector
114   Ustar = U;
115   [rho,u,p,c] = CEV_calc(Ustar,psat,pc,rhol,rhov,K0,N,...
116                 rho_CEVinterp,p_CEVinterp,CEV_a,CEV_b,CEV_c,CEV_gV);
117   dt = calc_dt(Ustar,c,CFL,dx);
118
119   % Runge Kutta - step 1
120   [UL,UR] = MUSCL(Ustar,dx);
121   [rhoL,vL,pL,cL] = CEV_calc(UL,psat,pc,rhol,rhov,K0,N,...
122                     rho_CEVinterp,p_CEVinterp,CEV_a,CEV_b,CEV_c,CEV_gV);
123   [rhoR,vR,pR,cR] = CEV_calc(UR,psat,pc,rhol,rhov,K0,N,...
124                     rho_CEVinterp,p_CEVinterp,CEV_a,CEV_b,CEV_c,CEV_gV);
125   F = AUSM_HLLC(rhoL,rhoR,vL,vR,pL,pR,cL,cR,tnx);
126   RHS = calc_RHS(Ustar,X);
127
128   Ustar(i,:)= U(i,:) - (1/4)*(dt/dx)*(F(i,:) - F(im1,:)) - (1/4)*dt*RHS(i,:);
129
130   [rho,u,p,c] = CEV_calc(Ustar,psat,pc,rhol,rhov,K0,N,...
131                     rho_CEVinterp,p_CEVinterp,CEV_a,CEV_b,CEV_c,CEV_gV);
132   Ustar = apply_BC(Ustar,rho,u,p,c,u_inlet,p_outlet,psat,rhol,K0,N,dt,dx,tnx);
133
134   % Runge Kutta - step 2
135   [UL,UR] = MUSCL(Ustar,dx);
136   [rhoL,vL,pL,cL] = CEV_calc(UL,psat,pc,rhol,rhov,K0,N,...
```

```
137                     rho_CEVinterp,p_CEVinterp,CEV_a,CEV_b,CEV_c,CEV_gV);
138   [rhoR,vR,pR,cR] = CEV_calc(UR,psat,pc,rhol,rhov,K0,N,...
139                     rho_CEVinterp,p_CEVinterp,CEV_a,CEV_b,CEV_c,CEV_gV);
140   F = AUSM_HLLC(rhoL,rhoR,vL,vR,pL,pR,cL,cR,tnx);
141   RHS = calc_RHS(Ustar,X);
142
143   Ustar(i,:)= U(i,:) - (1/3)*(dt/dx)*(F(i,:) - F(im1,:)) - (1/3)*dt*RHS(i,:);
144
145   [rho,u,p,c] = CEV_calc(Ustar,psat,pc,rhol,rhov,K0,N,...
146                   rho_CEVinterp,p_CEVinterp,CEV_a,CEV_b,CEV_c,CEV_gV);
147   Ustar = apply_BC(Ustar,rho,u,p,c,u_inlet,p_outlet,psat,rhol,K0,N,dt,dx,tnx);
148
149   % Runge Kutta - step 3
150   [UL,UR] = MUSCL(Ustar,dx);
151   [rhoL,vL,pL,cL] = CEV_calc(UL,psat,pc,rhol,rhov,K0,N,...
152                     rho_CEVinterp,p_CEVinterp,CEV_a,CEV_b,CEV_c,CEV_gV);
153   [rhoR,vR,pR,cR] = CEV_calc(UR,psat,pc,rhol,rhov,K0,N,...
154                     rho_CEVinterp,p_CEVinterp,CEV_a,CEV_b,CEV_c,CEV_gV);
155   F = AUSM_HLLC(rhoL,rhoR,vL,vR,pL,pR,cL,cR,tnx);
156   RHS = calc_RHS(Ustar,X);
157
158   Ustar(i,:)= U(i,:) - (1/2)*(dt/dx)*(F(i,:) - F(im1,:)) - (1/2)*dt*RHS(i,:);
159
160   [rho,u,p,c] = CEV_calc(Ustar,psat,pc,rhol,rhov,K0,N,...
161                     rho_CEVinterp,p_CEVinterp,CEV_a,CEV_b,CEV_c,CEV_gV);
162   Ustar = apply_BC(Ustar,rho,u,p,c,u_inlet,p_outlet,psat,...
163                     rhol,K0,N,dt,dx,tnx);
164
165   % Runge Kutta - step 4
166   [UL,UR] = MUSCL(Ustar,dx);
167   [rhoL,vL,pL,cL] = CEV_calc(UL,psat,pc,rhol,rhov,K0,N,...
168                     rho_CEVinterp,p_CEVinterp,CEV_a,CEV_b,CEV_c,CEV_gV);
169   [rhoR,vR,pR,cR] = CEV_calc(UR,psat,pc,rhol,rhov,K0,N,...
170                     rho_CEVinterp,p_CEVinterp,CEV_a,CEV_b,CEV_c,CEV_gV);
171   F = AUSM_HLLC(rhoL,rhoR,vL,vR,pL,pR,cL,cR,tnx);
172   RHS = calc_RHS(Ustar,X);
173
174   Ustar(i,:)= U(i,:) - (1/1)*(dt/dx)*(F(i,:) - F(im1,:)) - (1/1)*dt*RHS(i,:);
175
176   [rho,u,p,c] = CEV_calc(Ustar,psat,pc,rhol,rhov,K0,N,...
177                     rho_CEVinterp,p_CEVinterp,CEV_a,CEV_b,CEV_c,CEV_gV);
178   Ustar = apply_BC(Ustar,rho,u,p,c,u_inlet,p_outlet,psat,rhol,K0,N,dt,dx,tnx);
179
180   % final update vector
181   [UL,UR] = MUSCL(Ustar,dx);
182   [rhoL,vL,pL,cL] = CEV_calc(UL,psat,pc,rhol,rhov,K0,N,...
183                     rho_CEVinterp,p_CEVinterp,CEV_a,CEV_b,CEV_c,CEV_gV);
184   [rhoR,vR,pR,cR] = CEV_calc(UR,psat,pc,rhol,rhov,K0,N,...
185                     rho_CEVinterp,p_CEVinterp,CEV_a,CEV_b,CEV_c,CEV_gV);
186
187   F = AUSM_HLLC(rhoL,rhoR,vL,vR,pL,pR,cL,cR,tnx);
188   [rho,u,p,c] = CEV_calc(Ustar,psat,pc,rhol,rhov,K0,N,...
189                     rho_CEVinterp,p_CEVinterp,CEV_a,CEV_b,CEV_c,CEV_gV);
```

```
190   Ustar = apply_BC(Ustar,rho,u,p,c,u_inlet,p_outlet,psat,rhol,K0,N,dt,dx,tnx);
191
192   U = Ustar;
193
194   waitbar(t/tend,h);
195
196   % creating 'garbage', break if needed
197   if (any(isnan(U(:,2))))
198     errordlg('NaN values in m')
199     break
200   end
201
202   if mod(count,200) == 0
203     for i = 1:size(F,1)-1
204         diff(i,:) = F(i,:)-F(i+1,:);
205     end
206     tres(rescount) = t;
207     res1(rescount) = log10(abs(sum(diff(:,1))));
208     res2(rescount) = log10(abs(sum(diff(:,2))));
209     updateplot
210     updateplot2
211     rescount = rescount+1;
212   end
213
214   t = t + dt;
215   count = count + 1;
216 end
217
218 U = Ustar;
219
220 delete(h)
```

A.2 Apply_BC.m (subfunction)

```
1  function[U] = apply_BC(U,rho,u,p,c,u_inlet,p_outlet,psat,rhol,K0,N,dt,dx,tnx)
2  %% first order - 1 ghost point
3
4  c_avg = mean([c(1) c(2) c(tnx-1) c(tnx)]);
5  NDT = (c_avg*dt)/dx;
6
7  p_ghost_inlet = (p(1)+0.5*NDT*(p(2)+p(1)+rho(1)*c(1)*(u_inlet-u(2))))/(1+NDT);
8  u_ghost_inlet = (u(1)+0.5*NDT*(((p(1)-p(2))/(rho(1)*c(1)))+u_inlet+u(2)))/(1+NDT);
9
10 p_ghost_outlet = (p(tnx)+0.5*NDT*(p(tnx-1)+p_outlet...
11                  +rho(tnx)*c(tnx)*(u(tnx-1)-u(tnx))))/(1+NDT);
12 u_ghost_outlet = (u(tnx)+0.5*NDT*(((p(tnx-1)-p_outlet)...
13                  /(rho(tnx)*c(tnx)))+u(tnx)+u(tnx-1)))/(1+NDT);
14
15 rho_ghost_inlet = ((((p_ghost_inlet-psat)/K0)+1)^(1/N))*rhol;
16 rho_ghost_outlet = ((((p_ghost_outlet-psat)/K0)+1)^(1/N))*rhol;
17
18 % inlet
```

```
19
20 U(1,1) = rho_ghost_inlet;
21 U(1,2) = rho_ghost_inlet*u_ghost_inlet;
22
23 % outlet
24
25 U(tnx,1) = rho_ghost_outlet;
26 U(tnx,2) = rho_ghost_outlet*u_ghost_outlet;
27
28 % % inlet
29 %
30 % U(1,1) = U(2,1);
31 % U(1,2) = U(2,1)*u_inlet;
32 %
33 % % outlet
34 %
35 % U(tnx,1) = ((((p_outlet-psat)/K0)+1)^(1/N))*rhol;
36 % U(tnx,2) = U(tnx-1,2);
```

A.3 AUSM_HLLC.m (subfunction)

```
1  function[F] = AUSM_HLLC(rhoL_,rhoR_,uL_,uR_,pL_,pR_,cL_,cR_,tnx)
2
3  i = 1:tnx-1;
4  ip1 = 2:tnx;
5
6  rhoL = rhoR_(i);
7  rhoR = rhoL_(ip1);
8  uL = uR_(i);
9  uR = uL_(ip1);
10 pL = pR_(i);
11 pR = pL_(ip1);
12 cL = cR_(i);
13 cR = cL_(ip1);
14
15 cbar = 0.5*(cL+cR);
16 rhobar = 0.5*(rhoL+rhoR);
17 ML = uL./cbar;
18 MR = uR./cbar;
19 Mbar = 0.5*(ML.^2+MR.^2);
20
21 phalf = zeros(tnx-1,1);
22 mdot = zeros(tnx-1,1);
23
24 Ku = 3/4;
25 Minf = 0;
26 M0 = sqrt(min(1,max(Mbar(i),Minf)));
27 fa = M0.*(2-M0);
28 alpha = (3/16)*(-4+5*fa.^2);
29
30 pU = -2*Ku.*fa.*rhobar(i).*cbar(i).^2.*pPlus(ML(i),alpha)...
31       .*pMin(MR(i),alpha).*(MR(i)-ML(i));
```

```
32
33 phalf(i) = pL(i).*pPlus(ML(i),alpha) + pR(i).*pMin(MR(i),alpha) + pU;
34
35 SL = min(uL(i)-cL(i),uR(i)-cR(i));
36 SR = max(uL(i)+cL(i),uR(i)+cR(i));
37 SM = (pR(i)-pL(i)+rhoL(i).*uL(i).*(SL-uL(i))-rhoR(i).*uR(i).*(SR-uR(i)))./...
38          (rhoL(i).*(SL-uL(i))-rhoR(i).*(SR-uR(i)));
39
40 mdot(SL >= 0) = rhoL(SL >= 0).*uL(SL >= 0);
41
42
43 mdot(SL < 0 & SM >= 0) = rhoL(SL < 0 & SM >= 0).*uL(SL < 0 & SM >= 0)...
44                          +SL(SL < 0 & SM >= 0)...
45                          .*(rhoL(SL < 0 & SM >= 0).*((SL(SL < 0 & SM >= 0)...
46                          -uL(SL < 0 & SM >= 0))...
47                          ./(SL(SL < 0 & SM >= 0)-SM(SL < 0 & SM >= 0)))...
48                          -rhoL(SL < 0 & SM >= 0));
49 mdot(SM < 0 & SR >= 0) = rhoR(SM < 0 & SR >= 0).*uR(SM < 0 & SR >= 0)...
50                          +SR(SM < 0 & SR >= 0)...
51                          .*(rhoR(SM < 0 & SR >= 0).*((SR(SM < 0 & SR >= 0)...
52                          -uR(SM < 0 & SR >= 0))...
53                          ./(SR(SM < 0 & SR >= 0)-SM(SM < 0 & SR >= 0)))...
54                          -rhoR(SM < 0 & SR >= 0));
55 mdot(SR < 0) = rhoR(SR < 0).*uR(SR < 0);
56
57 F(:,1)  = mdot;
58 F(:,2)  = 0.5*mdot.*(uL + uR) - 0.5.*abs(mdot).*(uR-uL) + phalf;
59
60 clear i
```

A.4 calc_dt.m (subfunction)

```
1 function [dt] = calc_dt(U,c,CFL,dx)
2
3 v_max = max(abs(U(:,2)./U(:,1)));
4 c_max = max(c);
5 dt = (CFL*dx)/(v_max+c_max);
6
7 end
```

A.5 calc_RHS.m (subfunction)

```
1 function [out] = calc_RHS(U,X)
2
3 dA = zeros(size(X));
4 A = zeros(size(X));
5
6 A(X<-0.5) = 2;
7 A(X>=-0.5 & X<=0.5) = 1+sin(pi*X(X>=-0.5 & X<=0.5)).^2;
8 A(X>0.5) = 2;
9
```

```
dA(X<-0.5) = 0;
dA(X>=-0.5 & X<=0.5) = pi*sin(2*pi*X(X>=-0.5 & X<=0.5));
dA(X>0.5) = 0;

out(:,1) = ((U(:,2))./A).*dA;
out(:,2) = ((U(:,2).*(U(:,2)./U(:,1)))./A).*dA;

end
```

A.6 CEV_calc.m (subfunction)

```
function [rho,v,p,c] = CEV_calc(U,psat,pc,rhol,rhov,K0,N...
                        ,rho_CEVinterp,p_CEVinterp,CEV_a,CEV_b,CEV_c,CEV_gV)

% IMPORTANT!
% different nomenclature possibe --> LEFT = PLUS / RIGHT = MINUS
rho = U(:,1);
v = U(:,2)./U(:,1);

p = zeros(size(rho));
c = zeros(size(rho));

%% split density over two EoS

rho_Tait = rho(rho >= rhol);
rho_CEV = rho(rho < rhol);

%% Tait EoS

p_Tait = K0*((rho_Tait./rhol).^N -1) + psat;

c_Tait = sqrt((N*K0*(rho_Tait./rhol).^(N-1))./rhol);

c(rho >= rhol) = c_Tait;
p(rho >= rhol) = p_Tait;

%% CEV model

p_CEV = interp1(rho_CEVinterp,p_CEVinterp,rho_CEV);

alpha = (rho_CEV - rhol)/(rhov - rhol);
gL = exp(CEV_a.*log(p_CEV./pc).^2+CEV_b.*log(p_CEV./pc)+CEV_c);
c_CEV = sqrt(1./(rho_CEV.*((alpha./p_CEV).*CEV_gV ...
        + ((1-alpha)./p_CEV).*gL)));

p(rho < rhol) = p_CEV;
c(rho < rhol) = c_CEV;
```

A.7 CEV_interp.m (subfunction)

```
function [rho] = CEV_interp(P,Psat,Pc,rhoL,rhoV,CEV_a,CEV_b,CEV_c,gV)

 gL = exp(CEV_a.*log(P./Pc).^2+CEV_b.*log(P./Pc)+CEV_c);

 A = 2.*gL + 2.*gV;
 B = (gL*rhoV)./2 + (gV*rhoL)./2;
 C = rhoL - rhoV;

 X1 = atanh((rhoL.*A)./(2.*B));
 X2 = log(P./Psat).*(B./C);
 X3 = -(2*B./A).*(tanh(X2-X1) -1);

 rho = abs(X3);

end
```

A.8 fluxlim.m (subfunction)

```
function phi = fluxlim(nom,denom,limtype)

% % very small nominator = 0/1 = 0
nom(abs(nom)<1e-14) = 0;
denom(abs(nom)<1e-14) = 1;

% very small denominator = inf/1 = inf
nom((nom>1e-14)&(abs(denom)<1e-14)) = 1e14;
denom((nom>1e-14)&(abs(denom)<1e-14)) = 1;

% very small negative denominator = -inf/1 = -inf
nom((nom<-1e-14)&(abs(denom)<1e-14)) = -1e14;
denom((nom<-1e-14)&(abs(denom)<1e-14)) = 1;

r = nom./denom;

phi = zeros(size(nom));

    if limtype == 0                 % No limiting, no MUSCL
    phi = 0;
    phi = max(0,phi);

    elseif limtype == 1             % No limiting
    phi = 1;
    phi = max(0,phi);

    elseif limtype == 2             % Minmod
    phi = max(0, min(r,1));
    phi = max(0,phi);

    elseif limtype == 3             % Barth Jespersen
    phi = min(1,min(4./(r+1),(4.*r)./(r+1)));
    phi = max(0,phi);

```

```
35      else
36      error('unknown lim type')
37
38      end
39
40    end
```

A.9 MUSCL.m (subfunction)

```
1  function[ULlim,URlim] = MUSCL(U,dx)
2
3  Lx = size(U,1);
4  phiL = zeros(Lx,2);
5  phiR = zeros(Lx,2);
6
7  i = 2:Lx-1;
8  ip1 = 3:Lx;
9  im1 = 1:Lx-2;
10
11 gradU = [0 0;
12         U(ip1,:)-U(im1,:);
13         0 0 ];
14
15 UL = U - 0.25.*gradU;
16 UR = U + 0.25.*gradU;
17
18 Umax(i,:) = max(U(i,:),max(U(ip1,:),U(im1,:)));
19 Umin(i,:) = min(U(i,:),min(U(ip1,:),U(im1,:)));
20 % different maximum for the edges, only 1 neighbour
21 Umax(1,:) = max(U(1,:),U(2,:));
22 Umin(1,:) = min(U(1,:),U(2,:));
23 Umax(Lx,:) = max(U(Lx,:),U(Lx-1,:));
24 Umin(Lx,:) = min(U(Lx,:),U(Lx-1,:));
25
26 rmaxL = (Umax-U)./(UL-U);
27 rminL = (Umin-U)./(UL-U);
28 rmaxR = (Umax-U)./(UR-U);
29 rminR = (Umin-U)./(UR-U);
30
31 K = 0.3;
32 epsq = (K*dx)^3;
33
34 VmaxL = (rmaxL.^2+2.*rmaxL+epsq)./(rmaxL.^2+rmaxL+2+epsq);
35 VminL = (rminL.^2+2.*rminL+epsq)./(rminL.^2+rminL+2+epsq);
36 VmaxR = (rmaxR.^2+2.*rmaxR+epsq)./(rmaxR.^2+rmaxR+2+epsq);
37 VminR = (rminR.^2+2.*rminR+epsq)./(rminR.^2+rminR+2+epsq);
38
39 phiL(UL>U) = VmaxL(UL>U);
40 phiL(UL<U) = VminL(UL<U);
41 phiL(UL==U) = 1;
42
43 phiR(UR>U) = VmaxR(UR>U);
```

```
44 phiR(UR<U) = VminR(UR<U);
45 phiR(UR==U) = 1;
46
47 phi = min(phiL,phiR);
48
49 ULlim = U - 0.25*phi.*gradU;
50 URlim = U + 0.25*phi.*gradU;
```

A.10 pMin.m (subfunction)

```
1  function [pMin] = pMin(M,alpha)
2
3  MaM1 = 0.5*(M-abs(M));
4  MaP2 = 0.25*(M+1).^2;
5  MaM2 = -0.25*(M-1).^2;
6
7  pMin = zeros(size(M));
8
9  pMin(abs(M) >= 1) = (1./M(abs(M) >= 1)).*MaM1(abs(M) >= 1);
10 pMin(abs(M) < 1) = MaM2(abs(M) < 1).*((-2-M(abs(M) < 1)) ...
11                    +16.*alpha(abs(M) < 1).*M(abs(M) < 1).*MaP2(abs(M) < 1));
12
13 end
```

A.11 pPlus.m (subfunction)

```
1  function [pPlus] = pPlus(M,alpha)
2
3  MaP1 = 0.5*(M+abs(M));
4  MaP2 = 0.25*(M+1).^2;
5  MaM2 = -0.25*(M-1).^2;
6
7  pPlus = zeros(size(M));
8
9  pPlus(abs(M) >= 1) = (1./M(abs(M) >= 1)).*MaP1(abs(M) >= 1);
10 pPlus(abs(M) < 1) = MaP2(abs(M) < 1).*((2-M(abs(M) < 1)) ...
11                     -16.*alpha(abs(M) < 1).*M(abs(M) < 1).*MaM2(abs(M) < 1));
12
13 end
```

A.12 data_WATER_10ms.m (example input file)

```
1 %% fluid parameters
2
3 nCmp  = 1;
4 Cnc   = [1,0];
5 Model = 'IF97';
6 Cmp   = 'water';
7
8 Tinf = 293.15;
```

```
9
10 K0 = 3.6904e8;
11 N = 5.9496;
12
13 CEV_a = 0.01262;
14 CEV_b = -0.6014;
15 CEV_c = 0.8241;
16 CEV_gV = 0.8870;
17
18 %% BC/IC
19 CFL = 0.9;
20 tend = 30;
21
22 p_outlet = 1.0000e5;
23 u_inlet = 10;
24 p_init = 1.0000e5;
25 u_init = 10;
26
27 nx = 250;
28 ny = 1;
29 gp = 1;
30
31 %% numerical parameters
32 % No MUSCL          = 0  (works)
33 % MUSCL, no limiter = 1  (heavy oscillations)
34 % MinMod            = 2  (works)
35 % Barth Jespersen   = 3  (works)
36 limtype = 3;
37
38 viewgrid = 0;
```

Appendix B

Appendix B: 2D OpenFOAM application

B.1 Mydbns_water.c (main application)

```
/*---------------------------------------------------------------------------*\
  =========                 |
  \\      /  F ield         | foam-extend: Open Source CFD
   \\    /   O peration     |
    \\  /    A nd           | For copyright notice see file Copyright
     \\/     M anipulation  |
-------------------------------------------------------------------------------
License
    This file is part of foam-extend.

    foam-extend is free software: you can redistribute it and/or modify it
    under the terms of the GNU General Public License as published by the
    Free Software Foundation, either version 3 of the License, or (at your
    option) any later version.

    foam-extend is distributed in the hope that it will be useful, but
    WITHOUT ANY WARRANTY; without even the implied warranty of
    MERCHANTABILITY or FITNESS FOR A PARTICULAR PURPOSE.  See the GNU
    General Public License for more details.

    You should have received a copy of the GNU General Public License
    along with foam-extend.  If not, see <http://www.gnu.org/licenses/>.

Application
    dbnsTurbFoamHEqn

Description
    Density-based compressible explicit time-marching flow solver
```

```
29      using enthalpy-based thermo packages
30
31  Author
32      Hrvoje Jasak
33
34  \*---------------------------------------------------------------------------*/
35
36  #include "fvCFD.H"
37  #include "basicPsiThermo.H"
38  #include "basicRhoThermo.H"
39  #include "MyturbulenceModel.H"
40  #include "bound.H"
41  #include "AUSMHLLCFlux.H"
42  #include "MDLimiter.H"
43  #include "BarthJespersenLimiter.H"
44  #include "VenkatakrishnanLimiter.H"
45  #include "numericFlux.H"
46  #include "IFstream.H"
47  #include "graph.H"
48  #include "interpolateXY.H"
49  #include "localTimeStep.H"
50
51  // * * * * * * * * * * * * * * * * * * * * * * * * * * * * * * * * * * * * * * * * * * * * //
52
53  int main(int argc, char *argv[])
54  {
55  #   include "setRootCase.H"
56  #   include "createTime.H"
57  #   include "createMesh.H"
58  #   include "createFields.H"
59
60  // * * * * * * * * * * * * * * * * * * * * * * * * * * * * * * * * * * * * * * * * * * * * //
61
62      Info<< "\nStarting time loop\n" << endl;
63
64      // Runge-Kutta coefficient
65      scalarList beta(4);
66      beta[0] = 0.1100;
67      beta[1] = 0.2766;
68      beta[2] = 0.5000;
69      beta[3] = 1.0000;
70
71      while (runTime.run())
72      {
73  #       include "readTimeControls.H"
74  #       include "readFieldBounds.H"
75  //# include "compressibleCourantNo.H"
76  //# include "setDeltaT.H"
77
78          runTime++;
79
80          Info<< "\n Time = " << runTime.value() << endl;
81
```

```
82          // Switch off solver messages for diagonal solver RK
83          lduMatrix::debug = 0;
84
85      localTimeStep.update(maxCo, adjustTimeStep);
86
87          // Low storage Runge-Kutta time integration
88          forAll (beta, i)
89          {
90              // Solve the approximate Riemann problem for this time step
91              dbnsFlux.computeFlux();
92
93          physDeltaT[0] = beta[i];
94
95              // Time integration
96              solve
97              (
98                  1.0/beta[i]*fvm::ddt(rho)
99                + fvc::div(dbnsFlux.rhoFlux())
100             );
101
102             solve
103             (
104                 1.0/beta[i]*fvm::ddt(rhoU)
105               + fvc::div(dbnsFlux.rhoUFlux())
106               + fvc::div(turbulence->devRhoReff())
107             );
108
109 #           include "updateVelocity.H"
110 #       include "updatePressure.H"
111 #       include "updateThermo.H"
112         }
113
114         // Switch on solver messages for turbulence
115         lduMatrix::debug = 1;
116
117         turbulence->correct();
118
119 # include "Eulerresiduals.H"
120
121     Info  << "rho residual: "
122       << max(L2NormRho,SMALL) << endl
123       << "rhoUX residual: "
124       << max(L2NormRhoUX,SMALL) << endl
125       << "rhoUY residual: "
126       << max(L2NormRhoUY,SMALL) << endl
127       << "rhoUZ residual: "
128       << max(L2NormRhoUZ,SMALL) << endl << endl;
129
130         runTime.write();
131
132         Info<< "    ExecutionTime = "
133             << runTime.elapsedCpuTime()
134             << " s\n" << endl;
```

```
135     }
136
137     Info<< "\n end \n";
138
139     return(0);
140 }
141
142
143 // ************************************************************************* //
```

Bibliography

[1] John Anspach Consulting, "Solving a cavitation problem." https://jacpump.wordpress.com/2011/04/17/solving-a-cavitation-problem/, April 2011.

[2] F. C. Visser, J. J. Backx, J. Geerts, M. Cugal, and D. Medina Torres, "Pump impeller lifetime improvement through visual study of leading-edge cavitation," in *Proceedings of the 15th International Pump Users Symposium*, (Turbomachinery Laboratory, Texas A&M University, College Station, TX), pp. 109–118, 1998.

[3] F. Visser, "Some user experience demonstrating the use of computational fluid dynamics for cavitation analysis and head prediction of centrifugal pumps," in *Proceedings of the Fourth ASME International Symposium on Pumping Machinery, New Orleans, Louisiana. Paper No. FEDSM2001-18087*, 2001.

[4] C. E. Brennen, *Cavitation and bubble dynamics*. Cambridge University Press, 2013.

[5] P. Colonna and T. Van der Stelt, "Fluidprop main homepage." http://www.asimptote.nl/software/fluidprop, January 2010. version 2.4.0.55.

[6] J. Dymond and R. Malhotra, "The tait equation: 100 years on," *International journal of thermophysics*, vol. 9, no. 6, pp. 941–951, 1988.

[7] E. F. Toro, M. Spruce, and W. Speares, "Restoration of the contact surface in the hll-riemann solver," *Shock waves*, vol. 4, no. 1, pp. 25–34, 1994.

[8] M.-S. Liou, "A sequel to ausm: Ausm+," *Journal of computational Physics*, vol. 129, no. 2, pp. 364–382, 1996.

[9] H. Rouse and J. S. McNown, "Cavitation and pressure distribution: head forms at zero angle of yaw," 1948.

[10] E. Johnsen and T. Colonius, "Compressible multicomponent flow calculations and shock–bubble interaction," in *Proc. of Sixth International Symposium on Cavitation*, 2006.

[11] H. Higuchi, R. Arndt, and M. Rogers, "Characteristics of tip vortex cavitation noise," *Journal of fluids engineering*, vol. 111, no. 4, pp. 495–501, 1989.

[12] L. Zhang and B. C. Khoo, "Dynamics of unsteady cavitating flow in compressible two-phase fluid," *Ocean Engineering*, vol. 87, pp. 174–184, 2014.

[13] The university of Tokyo, "Photographs and movies of cavitation." http://www.1.k.u-tokyo.ac.jp/yama/fluidlab/Research/CavPictures/index_e.html, April 2000.

[14] M. Berthelot, *Sur quelques phénomènes de dilatation forcée des liquides*. impr. Bachelier, 1850.

[15] H. H. Dixon, "The note on the tensile strength of water; vitality and the transmission of water through the stems," in *The Scientific Proceedings of the Royal Dublin Society,*, 1909.

[16] Y. A. Bouziad, *Physical modelling of leading edge cavitation: computational methodologies and application to hydraulic machinery*. PhD thesis, Citeseer, 2006.

[17] T. Leighton, *The acoustic bubble*. Academic press, 2012.

[18] T. v. Terwisga, "Cavitation on ship propellors." http://ocw.tudelft.nl/courses/marine-technology/cavitation-on-ship-propellers/course-home/, July 2010. lecture slides OpenCourseWare (OCW).

[19] The Suslick research group University of Illinois, "Collapse of a cavitation bubble." http://www.scs.illinois.edu/suslick/sonochembrittanica.html, August 2015.

[20] W. Xie, T. Liu, and B. Khoo, "Application of a one-fluid model for large scale homogeneous unsteady cavitation: The modified schmidt model," *Computers & Fluids*, vol. 35, no. 10, pp. 1177–1192, 2006.

[21] T. Liu, B. Khoo, and W. Xie, "Isentropic one-fluid modelling of unsteady cavitating flow," *Journal of Computational Physics*, vol. 201, no. 1, pp. 80–108, 2004.

[22] E. Rapposelli and L. d'Agostino, "A barotropic cavitation model with thermodynamic effects," in *Fifth International. Symposium on Cavitation, CAV2003*, (Osaka, Japan), November 2003.

[23] Y. Chen and S. D. Heister, "A numerical treatment for attached cavitation," *Journal of fluids engineering*, vol. 116, no. 3, pp. 613–618, 1994.

[24] E. Shams, J. Finn, and S. Apte, "A numerical scheme for euler–lagrange simulation of bubbly flows in complex systems," *International Journal for Numerical Methods in Fluids*, vol. 67, no. 12, pp. 1865–1898, 2001.

[25] Y. Delannoy, "Two phase flow approach in unsteady cavitation modelling," in *ASME Cavitation and Multiphase flow forum*, pp. 153–158, 1990.

[26] A. H. Koop, *Numerical simulation of unsteady three-dimensional sheet cavitation*. University of Twente, 2008.

[27] D. P. Schmidt, *Cavitation in diesel fuel injector nozzles*. PhD thesis, University of Wisconsin-Madison, 1997.

[28] G. B. Wallis, *One-dimensional two-phase flow*. McGraw-Hill New York, 1969.

[29] H. Karplus, "Propagation of pressure waves in a mixture of water and stream," tech. rep., DTIC Document, 1961.

[30] G. Brown and S. Gouse, "A survey of the velocity of sound in two-phase mixtures(isentropic sound velocity for single and two-phase mixtures noting effect of compressibility)," in *ASME WINTER annual winter meeting*, 1964.

[31] R. Courant, K. Friedrichs, and H. Lewy, "Über die partiellen differenzengleichungen der mathematischen physik," *Mathematische Annalen*, vol. 100, no. 1, pp. 32–74, 1928.

[32] P. J. Zwart, A. G. Gerber, and T. Belamri, "A two-phase flow model for predicting cavitation dynamics," in *Proceedings of the fifth international conference on multiphase flow, Yokohama, Japan*, 2004.

[33] A. K. Singhal, M. M. Athavale, H. Li, and Y. Jiang, "Mathematical basis and validation of the full cavitation model," *Journal of fluids engineering*, vol. 124, no. 3, pp. 617–624, 2002.

[34] R. F. Kunz, D. A. Boger, D. R. Stinebring, T. S. Chyczewski, J. W. Lindau, H. J. Gibeling, S. Venkateswaran, and T. Govindan, "A preconditioned navier–stokes method for two-phase flows with application to cavitation prediction," *Computers & Fluids*, vol. 29, no. 8, pp. 849–875, 2000.

[35] ANSYS Inc., "ANSYS CFX." http://www.ansys.com/, January 2015. version 15.0.

[36] M. Morgut and E. Nobile, "Numerical predictions of cavitating flow around model scale propellers by cfd and advanced model calibration," *International Journal of Rotating Machinery*, vol. 2012, p. 11, June 2012.

[37] S. Gopalan and J. Katz, "Flow structure and modeling issues in the closure region of attached cavitation," *Physics of Fluids*, vol. 12, no. 4, pp. 895–911, 2000.

[38] AEA Engineering, "CFX Tascflow." CD-ROM, May 2000. Tascflow version 2.10 - theory manual.

[39] C. E. Brennen, *Fundamentals of multiphase flow*. Cambridge University Press, 2005.

[40] P. G. Tait, *Report on some of the physical properties of fresh water and of sea water*. Johnson Reprint Corporation, 1965.

[41] G. Tammann, "The dependence of the volume of solutions on pressure," *Z. Phys. Chem. Stoechiom. Verwandtschafts*, vol. 17, pp. 620–636, 1895.

[42] B. Van Leer, "Towards the ultimate conservative difference scheme. V. A second-order sequel to Godunov's method," *Journal of computational Physics*, vol. 32, no. 1, pp. 101–136, 1979.

[43] T. J. Barth and D. C. Jespersen, "The design and application of upwind schemes on unstructured meshes," *AIAA Paper No 89-0366*, 1989.

[44] V. Venkatakrishnan, "Convergence to steady state solutions of the euler equations on unstructured grids with limiters," *Journal of computational physics*, vol. 118, no. 1, pp. 120–130, 1995.

[45] R. J. LeVeque, *Finite volume methods for hyperbolic problems*. Cambridge university press, 2002.

[46] J. Blazek, *Computational Fluid Dynamics: Principles and Applications*. Elsevier, 2005.

[47] M.-S. Liou, "A sequel to ausm, part ii: Ausm+-up for all speeds," *Journal of Computational Physics*, vol. 214, no. 1, pp. 137–170, 2006.

[48] S. J. Schmidt, I. H. Sezal, and G. H. Schnerr, "Compressible simulation of high-speed hydrodynamics with phase change," in *ECCOMAS CFD 2006: Proceedings of the European Conference on Computational Fluid Dynamics*, 2006.

[49] Flow Science Inc., "Laval nozzles." http://www.flow3d.com/home/industries/aerospace/laval-nozzles, January 2015.

[50] T. J. Poinsot and S. Lelef, "Boundary conditions for direct simulations of compressible viscous flows," *Journal of computational physics*, vol. 101, no. 1, pp. 104–129, 1992.

[51] MathWorks, "MATLAB." http://uk.mathworks.com/, January 2015. version R2014B.

[52] C. C. Tseng and W. Shyy, "Turbulence modeling for isothermal and cryogenic cavitation," *AIAA Paper No. 2009-1150. In*, 2009.

[53] F. R. Menter, "Two-equation eddy-viscosity turbulence models for engineering applications," *AIAA journal*, vol. 32, no. 8, pp. 1598–1605, 1994.

[54] B. Launder and B. Sharma, "Application of the energy-dissipation model of turbulence to the calculation of flow near a spinning disc," *Letters in heat and mass transfer*, vol. 1, no. 2, pp. 131–137, 1974.

[55] D. C. Wilcox *et al.*, *Turbulence modeling for CFD*. DCW industries La Canada, CA, 1998.

[56] S. B. Pope, *Turbulent flows*. Cambridge university press, 2000.

[57] H. Jasak, "dbnsturbfoam." http://sourceforge.net/p/openfoam-extend/foam-extend-3.1/ci/3c5ba8da44948851ffdcddc1a944a9ae5cf407a2/tree/applications/solvers/compressible/dbnsTurbFoam/, August 2015. source code.

[58] H. Jasak, "Coupled density-based solver for high-speed compressible flows." http://download2.polytechnic.edu.na/pub4/sourceforge/o/op/openfoam-extend/OpenFOAM_Workshops/OFW9_2014_Zagreb/Presentations/Karlo_Sunjo_OFW09_P_0123.pdf, June 2015. powerpoint slides.

[59] The OpenFOAM Extend Project , "OpenFOAM Extend (Open Source Field Operations And Manipulations)." http://www.extend-project.de, January 2015. Extended edition version 3.1.

[60] National Institute for Standards and Technology (NIST), "Refprop." http://www.nist.gov/srd/nist23.cfm, August 2015. release 23, version 9.0.

[61] T. I. A. for the Properties of Water and Steam, "Revised release on the iapws industrial formulation 1997 for the thermodynamic properties of water and steam." http://www.iapws.org/relguide/IF97-Rev.pdf, August 2007.

[62] L. Rayleigh, "Viii. on the pressure developed in a liquid during the collapse of a spherical cavity," *The London, Edinburgh, and Dublin Philosophical Magazine and Journal of Science*, vol. 34, no. 200, pp. 94–98, 1917.

[63] H. Lamb, *Hydrodynamics*. Cambridge university press, 1932.

[64] I. Senocak and W. Shyy, "A pressure-based method for turbulent cavitating flow computations," *Journal of Computational Physics*, vol. 176, no. 2, pp. 363–383, 2002.

[65] J. F. Gülich, *Centrifugal pumps*. Springer, 2008.

[66] B. Schiavello and F. C. Visser, "Pump cavitation & various npshr criteria, npsha margins, and impeller life expectancy," in *Proceedings of the 25th International Pump Users Symposium*, (Turbomachinery Laboratory, Texas A&M University, College Station, TX), pp. 113–144, 2009.

[67] H. J. Aguerre, S. M. Damián, J. M. Gimenez, and N. M. Nigro, "Modeling of compressible fluid problems with openfoam using dynamic mesh technology," *Mecénica Computacional*, vol. 33, pp. 995–1011, November 2013.

[68] M. Berger, M. J. Aftosmis, and S. M. Murman, "Analysis of slope limiters on irregular grids," Tech. Rep. 2005-0490, American Institute of Aeronautics and Astronautics, May 2005.

[69] B. Bicer, A. Tanaka, T. Fukuda, and A. Sou, "Numerical simulation of cavitation phenomena in diesel injector nozzles," in *16 th Annual Conf. ILASS-ASIA*, (Nagasaki, Japan), pp. 58–65, 2013.

[70] M. Bilanceri, F. Beux, and M. Salvetti, "Investigation on numerical schemes in the simulation of barotropic cavitating flows," in *Proceedings of the 7th International Symposium on Cavitation, CAV2009*, 2009.

[71] C. E. Brennen, *Hydrodynamics of pumps*. Cambridge University Press, 2011.

[72] D. Crighton, A. P. Dowling, J. F. Williams, M. Heckl, and F. Leppington, *Modern methods in analytical acoustics: lecture notes*. Springer Science & Business Media, 2012.

[73] M. P. Davis, *Experimental investigation of the cavitation of aviation fuel in a converging-diverging nozzle*. ProQuest, 2008.

[74] H. Ding, F. Visser, Y. Jiang, and M. Furmanczyk, "Demonstration and validation of a 3d cfd simulation tool predicting pump performance and cavitation for industrial applications," *Journal of Fluids Engineering*, vol. 133, no. 1, p. 011101, 2011.

[75] P. F. Dunn, F. O. Thomas, M. P. Davis, and I. E. Dorofeeva, "Experimental characterization of aviation-fuel cavitation," *Physics of Fluids (1994-present)*, vol. 22, no. 11, p. 117102, 2010.

[76] P. Eisenberg and R. Bergman, *Cavitation*. Encyclopaedia Britannica Educational Corporation, 1985.

[77] R. W. Erney, *Verification and validation of single phase and cavitating flows using an open source CFD tool*. PhD thesis, The Pennsylvania State University, 2008.

[78] C. Eskilsson and R. Bensow, "A compressible model for cavitating flow: comparison between euler, rans and les simulations," in *29th Symposium on Naval Hydrodynamics, Gothenburg, Sweden*, August 2012.

[79] E. Goncalvès and B. Charriere, "Modelling for isothermal cavitation with a four-equation model," *International Journal of Multiphase Flow*, vol. 59, pp. 54–72, 2014.

[80] H. Hoang, G. Galliero, F. Montel, and J. Bickert, "Tait equation in the extended corresponding states framework: Application to liquids and liquid mixtures," *Fluid Phase Equilibria*, vol. 387, pp. 5–11, 2015.

[81] F. P. Kärrholm, *Numerical modelling of diesel spray injection, turbulence interaction and combustion*. Chalmers University of Technology, 2008.

[82] H. Kanfoudi, H. Lamloumi, and R. Zgolli, *Numerical Investigation for Steady and Unsteady Cavitating Flows*. INTECH Open Access Publisher, 2012.

[83] F. P. Karrholm, H. Weller, and N. Nordin, "Modelling injector flow including cavitation effects for diesel applications," in *ASME/JSME 2007 5th joint fluids engineering conference*, pp. 465–474, American Society of Mechanical Engineers, 2007.

[84] R. Keppens, "Transsonic nozzle flow," February 2013.

[85] Z. Li, *Assessment of cavitation erosion with a multiphase Reynolds-Averaged Navier-Stokes method*. TU Delft, Delft University of Technology, 2012.

[86] D. Liuzzi, *Two phase cavitation modelling*. University of Rome, 2012.

[87] S. Martynov, D. Mason, M. R. Heikal, S. S. Sazhin, and M. Gorokhovski, "Modelling of cavitation flow in a nozzle and its effect on spray development," in *International Heat Transfer Conference 13*, Begel House Inc., 2006.

[88] K. D. Neroorkar, *Modeling of flash boiling flows in injectors with gasoline-ethanol fuel blends*. PhD thesis, University of Massachusetts - Amherst, 2011.

[89] G. Palau-Salvador, P. G. Altozano, and J. Arviza-Valverde, "Numerical modeling of cavitating flows for simple geometries using fluent v6. 1," *Spanish Journal of Agricultural Research*, vol. 5, no. 4, pp. 460–469, 2007.

[90] C. Pascarella, V. Salvatore, and A. Ciucci, "Effects of speed of sound variation on unsteady cavitating flows by using a barotropic model," in *5th International Symposium on Cavitation CAV2003, Osaka, Japon*, 2003.

[91] M. G. Rodio, *Numerical and Experimental Investigation of Water and Cryogenic Cavitating Flows*. PhD thesis, Università degli studi di Lecce, 2011.

[92] V. Salvatore, C. Pascarella, and L. d'Agostino, "Numerical evaluation of cavitating flows using different two-phase models," in *Fourth International Conference on Multiphase Flow, ICMF2001*, no. 713, May 2001.

[93] S. I. Sandler *et al.*, *Chemical, biochemical, and engineering thermodynamics*, vol. 4. John Wiley & Sons Hoboken, NJ, 2006.

[94] J. Sauer, *Instationär kavitierende Strömungen - Ein neues Modell basierende auf Front Capturing (VoF) und Blasendynamik*. PhD thesis, Karlsruher Institut für Technologie, 2000.

[95] R. Saurel and R. Abgrall, "A simple method for compressible multifluid flows," *SIAM Journal on Scientific Computing*, vol. 21, no. 3, pp. 1115–1145, 1999.

[96] G. H. Schnerr, I. H. Sezal, and S. J. Schmidt, "Numerical investigation of three-dimensional cloud cavitation with special emphasis on collapse induced shock dynamics," *Physics of Fluids (1994-present)*, vol. 20, no. 4, p. 040703, 2008.

[97] E. Usta and L. N. Sankar, "Application of high order schemes to aerodynamics of hovering rotors," in *AHS Aerodynamics, Acoustics, and Test and Evaluation Technical Specialists Meeting*, 2002.

[98] T. Van der Stelt, N. Nannan, and P. Colonna, "The iprsv equation of state," *Fluid Phase Equilibria*, vol. 330, pp. 24–35, 2012.

[99] S. Venkateswaran, J. W. Lindau, R. F. Kunz, and C. L. Merkle, "Computation of multiphase mixture flows with compressibility effects," *Journal of Computational Physics*, vol. 180, no. 1, pp. 54–77, 2002.

[100] Y. Ventikos and G. Tzabiras, "A numerical method for the simulation of steady and unsteady cavitating flows," *Computers & Fluids*, vol. 29, no. 1, pp. 63–88, 2000.

[101] W. Wagner and A. Pruss, "International equations for the saturation properties of ordinary water substance. revised according to the international temperature scale of 1990. addendum to j. phys. chem. ref. data 16, 893 (1987)," *Journal of Physical and Chemical Reference Data*, vol. 22, no. 3, pp. 783–787, 1993.

[102] W. Wei, X. Luo, B. Ji, B. Zhuang, and H. Xu, "Cavitating flow investigation inside centrifugal impellers for a condensate pump," in *IOP Conference Series: Earth and Environmental Science*, vol. 15, p. 032061, IOP Publishing, 2012.

[103] R. Yin and W. Chow, "Comparison of four algorithms for solving pressure-velocity linked equations in simulating atrium fire," *Int J Archit Sci*, vol. 4, no. 1, pp. 24–35, 2003.

[104] W. Yuan, J. Sauer, and G. H. Schnerr, "Modeling and computation of unsteady cavitation flows in injection nozzles," *Mécanique & industries*, vol. 2, no. 5, pp. 383–394, 2001.